

POLITECNICO DI TORINO

Collegio di Ingegneria Meccanica

**Corso di Laurea Magistrale
in Ingegneria Meccanica**

Tesi di Laurea Magistrale

Characterization of single crystals and single grain boundaries in commercially pure titanium



Relatore

Prof. Aurelio Somà

Candidato

Ivan D'Auria

Table of Contents

Abstract.....	6
Acknowledgements.....	7
Chapter 1 Introduction.....	8
1.1 Background.....	8
1.2 Aim and scope.....	8
1.3 Organization of the thesis.....	9
Chapter 2 Literature review.....	10
2.1 Titanium basic properties and applications.....	10
2.2 Crystal structure.....	11
2.3 Crystallographic defects	13
2.4 Slip systems.....	15
2.5 Grain boundary strength.....	20
Chapter 3 Material, heat treatment and microstructure investigation.....	24
3.1 Material.....	24
3.2 Material fabrication.....	24
3.3 Annealing.....	25
3.4 Metallographic preparation.....	29
Chapter 4 From EBSD to the gauge configuration.....	34
4.1 EBSD.....	34
4.1.1 From the EBSD map analysis to the final sample shape.....	41
4.2 Femtosecond laser micromachining.....	43

4.2.1 Machining steps.....	46
4.2.2 Gauge dimensions.....	50
Chapter 5 Data acquisition.....	51
5.1 Tensile testing.....	51
5.2 Strain measurement with DIC.....	55
Chapter 6 Experiments.....	58
6.1 Single grain in tensile gauge.....	58
6.1.1 Sample “A2”.....	58
6.2 Gauge containing a single grain boundary separating two single crystals.....	65
6.2.1 Sample “A3”.....	65
6.2.2 Sample “A6”.....	74
6.2.3 Sample “A7”.....	82
6.2.4 Sample “A8”.....	90
Chapter 7 Results analysis.....	98
7.1 Single grain boundaries behaviour.....	98
7.2 Single crystal behaviour.....	100
7.2.1 Determination of the experimental CRSS and comparison with the literature.....	102
7.3 Fractography.....	105
Chapter 8 Discussions and conclusions.....	111
8.1 Discussions.....	111
8.2 Conclusions.....	114

Abstract

A new experimental procedure has been developed in the present study in order to investigate the behaviour of CP titanium single crystals with hexagonal closed packed (HCP) crystal structure. The work is mainly focus on the investigation of mechanical properties such as plasticity and anisotropy, with an emphasis on grain boundary effects. Dog bone shaped samples were cut out of a CP titanium foil using wire EDM. These samples were then polished with an automatic polishing machine, using the chemical-mechanical technique. EBSD mapping was performed to know the orientations of the crystals and the grain boundaries misorientation angles. Two micron-sized gauge configurations were introduced: in the first, the gauge only contains one crystal; in the second, two single crystals divided by a perpendicular grain boundary to the tensile axis constitute the gauge. The latter configurations and the “speckle pattern” that is useful for digital image correlation (DIC) were realized with femtosecond laser micromachining. The samples were finally tested in-situ using a micro tensile tester under a digital microscope, and the strain values were obtained using DIC technique. The experimental data confirmed the anisotropy of crystals and underlined different mechanical properties within the same principal slip system family. Large data were obtained on the basal family, this led to the possibility to define new Critical Resolved Shear Stress (CRSS) values for this family and compare them with previous results from the literature. It is found that the experimental basal CRSS values obtained in this study ($CRSS = 126,1 \pm 14$ MPa in average) are effectively in agreement with the literature. It emerges from the present study that the grain boundary misorientation angle seems to influence the dislocation motion and the locus of fracture.

Acknowledgements

I would like to express my gratitude towards my supervisor Professor Arnaud Weck. He gave me the possibility to perform my research on a really interesting subject and was always available for theoretical and technical clarifications. Thanks to his teachings, I was able to enhance my knowledge on science and engineering materials.

I would like to thank Professor Mohammed Yandouzi for performing EBSD maps and letting me use his polishing machine and his digital microscope.

I would like to acknowledge the help of the mechanical engineering technical officers John Perrins and Paul Burberry for cutting the coupons.

I would like to thank my colleagues Wasim Alam and Frederic Manseau with whom I shared great moments inside and outside the labs.

Finally and overall, I would like to thank my family and Nina for their support.

Chapter 1 Introduction

1.1 Research workplace

The work presented in this thesis was performed at the University of Ottawa, Ontario, Canada. As part of an enthusiastic research group, Fracture and Femtosecond Research Ottawa Group (FROG), most of the researches have been carried out in the Laboratory of Characterization of Materials at the Faculty of Engineering. FROG is mainly interested in the characterization of the mechanical properties of materials, mechanisms leading to material fracture, and ultrafast laser machining.

1.2 Aim and scope

The aim of this work is the investigation of the behaviour of commercially pure titanium single crystals with hexagonal closed packed (HCP) crystal structure and the study of the grain boundaries properties. The present research particularly focuses on crystal plasticity, reviewing what has been done whether theoretically, experimentally or analytically in previous papers. Hence, key concepts such as the Schmid factor and the critical resolved shear stress (CRSS) have been studied and implemented in order to make comparisons with the literature. The gauges of the samples include single grain boundaries that are studied to investigate mechanical properties, dislocation motion as well as fracture phenomena. The equipment that has been used for this research includes: wire EDM (Electrical discharge machining), a furnace for heat treatments, an automatic polishing machine,

optical microscopes, a digital microscope, a femtosecond laser micromachining system, a micro tensile tester, a digital image correlation (DIC) software and a scanning electron microscope (SEM).

1.3 Organization of the thesis

The following structure has been considered:

Chapter 1: Introduction

Chapter 2: Literature review

Chapter 3: Material, heat treatment and microstructure investigation

Chapter 4: From EBSD map to the gauge configuration

Chapter 5: Data acquisition

Chapter 6: Experiments

Chapter 7: Results analysis

Chapter 8: Discussions and conclusions

Chapter 2 Literature review

2.1 Basic properties and applications of Titanium

Commercially pure titanium grade 1 has been used in this research. The latter is the first of four grades and is characterized by the higher ductility and softness. It also possesses good properties in terms of formability, resistance to corrosion and resiliency [1]. Therefore, it is commonly available in form of titanium plate and tubing for many applications such as: chemical processing, chlorate manufacturing, dimensional stable anodes, desalination, architecture, medical industry, marine industry, automotive parts and airframe structure [2]. Its chemical composition and mechanical properties are listed in Table 2.1 [3].

Table 2.1 – Chemical composition and mechanical properties CP titanium grade 1.

CHEMICAL COMPOSITION							
Weight %	C	Fe	N ₂	O ₂	H ₂ (sheet)	H(bar)	Ti
Min.							
Max.	0.1	0.2	0.03	0.18	0.015	0.0125	Balance

MECHANICAL PROPERTIES		
	Minimum	Typical
UTS, MPa	241	345
0.2% PS, MPa	172	221
Elongation on 2 in., %	25	37
Reduction of area, %	35	-
Elastic modulus, GPa	-	103
Hardness, HBN	-	120

Obviously the table describes the macroscopic mechanical properties of CP titanium grade 1. In the present work, its behaviour at a microscopic scale will be investigated.

2.2 Crystal structure

Pure titanium presents two types of structures: a hexagonal closed packed (HCP) crystal structure, also known as α phase, for lower temperatures and a body centered cubic (BCC) crystal structure or β phase. The transition temperature between the two phases is equal to 882°C , but it may vary depending on the purity of the metal [4].

Fig. 2.1 shows the two types of unit cell of titanium. In the present activity, the HCP structure is the one that is studied. This cell presents two parameters: a (0.295 nm) and c (0.468 nm). Figure 2.1 exhibits, with reference to the HCP cell, the three most densely packed types of lattice planes, the (0002) plane, also called basal plane, one of the three $\{10\bar{1}0\}$ planes, also called prismatic planes, and one of the six $\{10\bar{1}\bar{1}\}$ planes, also called pyramidal planes [4].

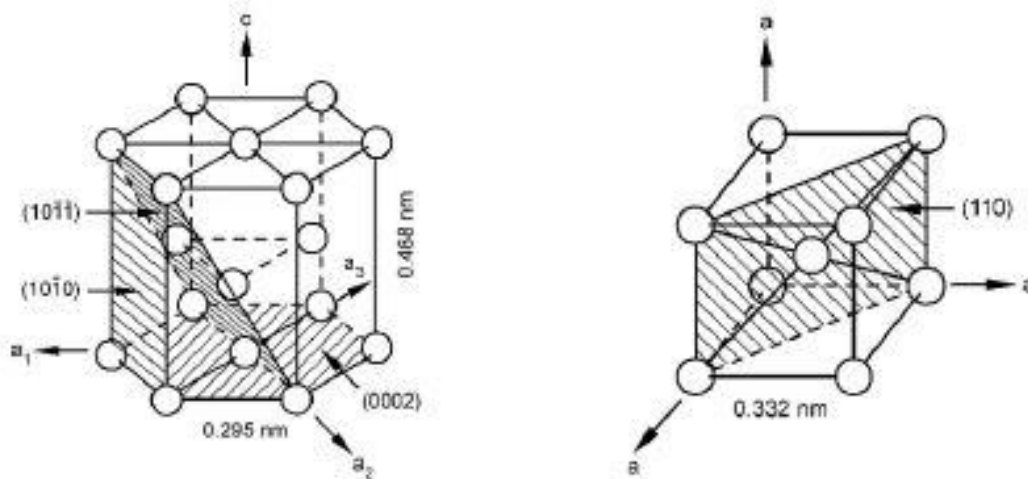


Fig. 2.1 – Two different lattices of titanium: HCP crystal structure on the left, BCC crystal structure on the right.

HCP crystal has an anisotropic behaviour; this means that the elastic properties vary depending on its orientation. In fig 2.2, the Young's modulus vs the declination angle is represented [4].

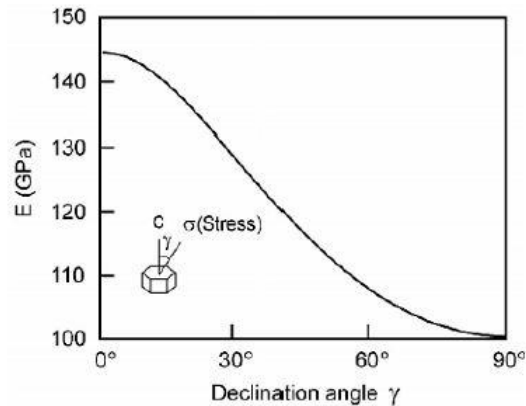


Fig. 2.2 – Young's modulus vs declination angle for a HCP crystal [5].

In fig. 2.3, it is possible to identify three different stages of deformation:

- The first part is known as “easy glide” and it is characterized by low strain hardening, large dislocation velocity and a single slip.
- The second region is known as “double glide” and it is represented by strong strain hardening, immobilization of dislocations, an increase in dislocation density and a decrease of dislocation velocity.
- The last region is characterized by a reduction of dislocation density and the possibility for new dislocations to be created [54].

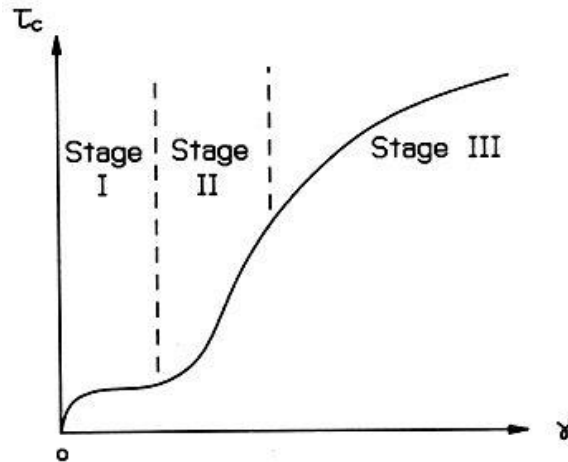


Fig. 2.3 – Shear stress – shear strain for a single crystal

2.3 Crystallographic defects

All the atoms would occupy the correct reticular positions in the lattice if the crystals were ideal. It is well known that crystals are not perfect as they present defects that can influence the mechanical properties. The various defects that are found in crystalline solids are usually classified by their dimension:

- The 0-dimensional defects are also called point defects because they affect single lattice points. The defects belonging to this category are further classified into intrinsic and extrinsic. Vacancies and interstitials (Fig. 2.4) are intrinsic defects: a vacancy is created when there is lack of one atom in a particular position of the crystal; an interstitial is caused when an atom occupies a position where no atom would ordinarily appear.

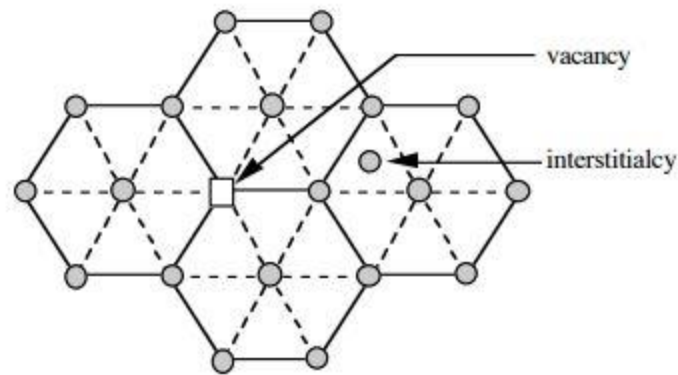


Fig. 2.4 – Illustration of an interstitial site and a vacancy. [17]

Extrinsic defects are composed by foreign atoms that are called solutes if they are added to the material on purpose, or impurities if they are not.

- The 1-dimensional defects are the dislocations that are the lines along which the crystal pattern is broken. The dislocations can be: edge, screw or mixed. Fig. 2.5 shows an illustration of these types of dislocations.

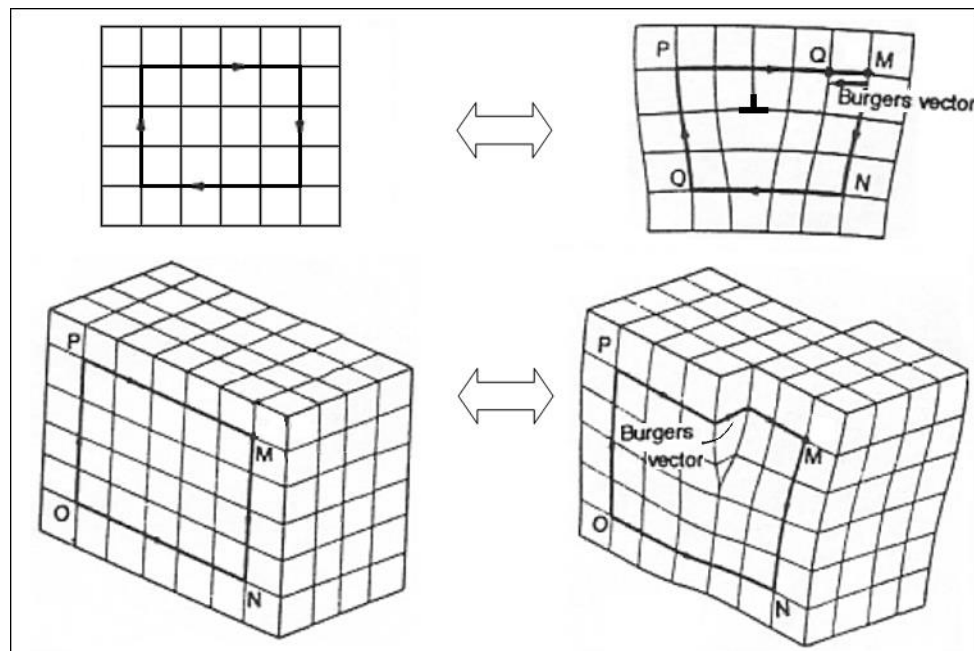


Fig. 2.5 – Illustration of screw dislocation (bottom) and edge dislocation (top). [18]

In this concept, the Burgers vector assumes an important role. In fact, it defines the magnitude and direction of the lattice distortion resulting from a dislocation in a crystal lattice [19]. In fig. 2.5, it can be seen that the Burgers vector is perpendicular to the dislocation line in edge dislocations. In screw dislocations, Burgers vector and dislocation line are parallel [20].

- The 2-dimensional defects, also known as planar defects, are related to grain boundaries. Grain boundaries are nothing else than interfaces that separate grains. Its structure depends on the misorientation of the crystals that it separates. If the misorientation is small, the grain boundary structure can be assumed as a simple planar array of dislocations. If the misorientation is larger, then its structure is more complicated [18].
- The 3-dimensional defects are referred to voids, cracks and inclusions.

2.4 Slip systems

Fig. 2.6 exhibits the different slip systems and slip direction for the HCP unit cell ($\langle a \rangle$ and $\langle c+a \rangle$ are the Burgers vectors). The first slip system to be activated depends on the orientation of the crystal [6,7] and on the tensile direction. By loading a polycrystalline sample in one direction, the first crystals to yield will be the ones where the weakest slip systems are activated or rather, the slip systems with lowest critical resolved shear stress (CRSS) values. To better understand the mechanisms of the plastic deformation, it is more convenient to explain these concepts with easier systems like mono-

crystals. “The first slip occurs when the shear stress across the plane exceeds a certain value. This threshold value is called critical resolved shear stress” [8].

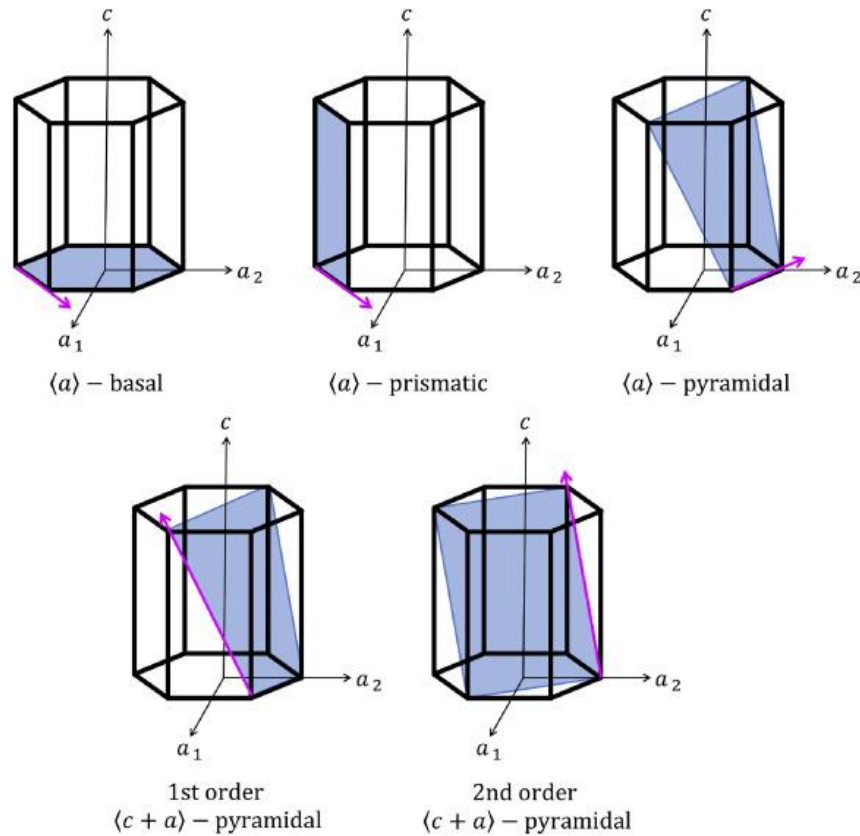


Fig 2.6 - Different slip systems and slip direction for the HCP unit cell [9].

It is well established in the literature that the weakest slip system for titanium is the prismatic because it presents lowest CRSS values. It is followed by the basal with medium CRSS values and the pyramidal with the highest CRSS values. The CRSS values depend on temperature, for any slip system it decreases with an increasing temperature, as shown in fig. 2.7 [10].

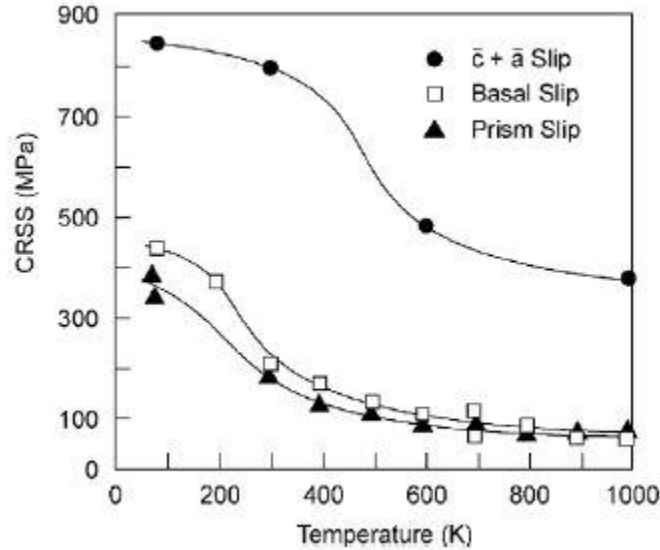


Fig. 2.7 – CRSS [MPa] vs Temperature [K] for different slip systems [10].

These CRSS values from fig 2.7 are referred to single crystals of Ti-6.6Al and therefore are not taken into account in the present research. A recent study by Wang L. et al [11], using high energy X-ray diffraction microscopy, has determined the following values:

- CRSS = 96 ± 18 MPa for prismatic slip systems.
- CRSS = 127 ± 33 MPa for basal slip systems.
- CRSS > 240 MPa for pyramidal $\langle c+a \rangle$ slip systems.

In the latter research, the average grain size was approximately 100 μm , very similar to this present study.

Gong and Wilkinson [12], through finite element simulations, discovered that the CRSS values are subjected to size effects. In fact, by testing cantilevers with increasing width (and adapting length and thickness with width), they noticed a decrease in CRSS. The paper only involves prismatic slip systems, for this reason, the y axis in fig. 2.7 is referred to the prismatic CRSS values.

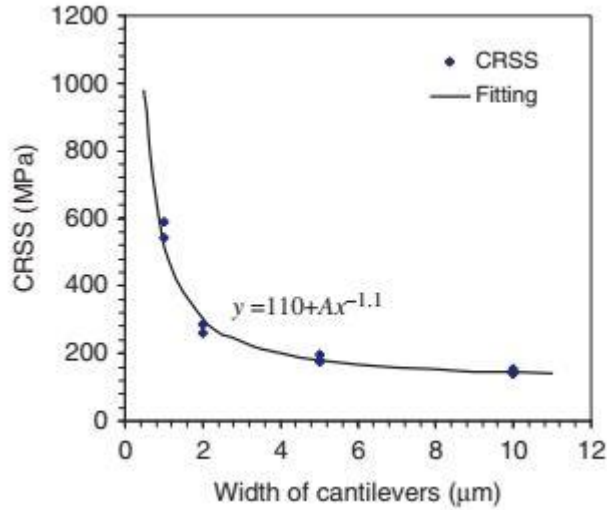


Fig. 2.8 – CRSS [MPa] vs width of cantilevers [μm] for prismatic slip systems.

Fig. 2.8 shows how those size effects saturate after a certain width, at around 10 μm . After saturation, the prismatic CRSS value is equal to 110 MPa [12].

The relation between the CRSS values and the yield strength of a single crystal stands in the Schmid's law [13]. Yield depends on the orientation of the crystal lattice relative to the tensile direction. It will begin on a

slip system when the shear stress reaches a critical value (CRSS) which is independent on the crystal lattice or the tensile direction. According to Schmid's law, the shear stress is given by the following equation:

$$\tau = \frac{F}{A} \cos \lambda \cos \varphi$$

where $F \cos \lambda$ is the stress along slip direction, $A/\cos \varphi$ is the area over which the shear force is applied. The Schmid factor is given by:

$$m = \cos \lambda \cos \varphi$$

$$0 \leq m \leq 0.5$$

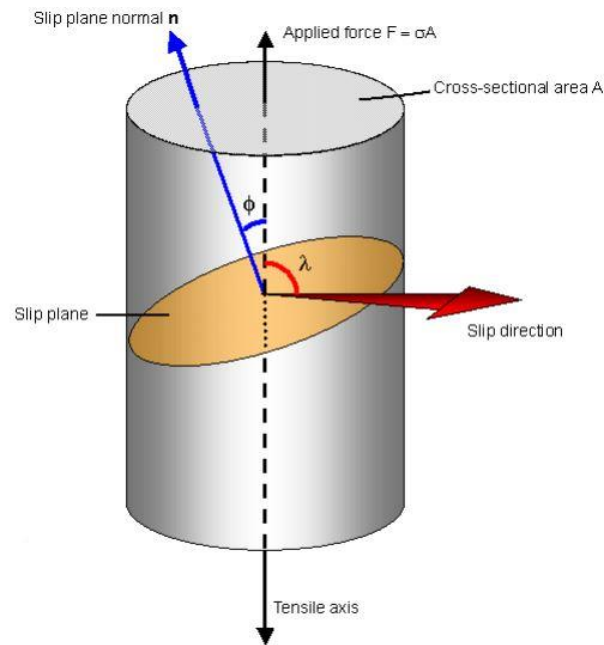


Fig. 2.9 – Slip plane and slip direction. [14]

Therefore the shear stress can be expressed as follows:

$$\tau = \sigma_{YS} m$$

The Schmid's factor is calculated for each slip system. By using the CRSS values for each family found in the literature, it is known that the first slip system to be active is the one presenting the lowest ratio CRSS/ m that defines the yield strength. In this context, a distinction between “soft orientation” and “hard orientation” can be done: the former indicates that the slip plane is at 45° to the tensile axis, the latter indicates that the slip plane is at 90° to the tensile axis. “Hard orientation” implies lower Schmid's factors and, consequently, higher yield strength.

2.5 Grain boundary strength

Degradation of grain boundary strength induced by corrosion, thermal ageing and irradiation is one of the causes of intergranular cracking. The decrease in grain boundary strength can occur because of segregation of impurities or solute elements (like hydrogen, helium and oxygen atoms), oxide formation, vacancies, and micro void formation, helium bubble formation [21]. Furthermore it is difficult to extract data related to the strength of an individual grain boundary, in fact, there is not much literature about it. In the last decade, mechanical properties measurements have been improved by a new technique called FIB (Focused Ion Beam), which allows to deal with specimens in micron or sub-micron scales [22]. Fig. 2.10 presents an illustration of the FIB technique.

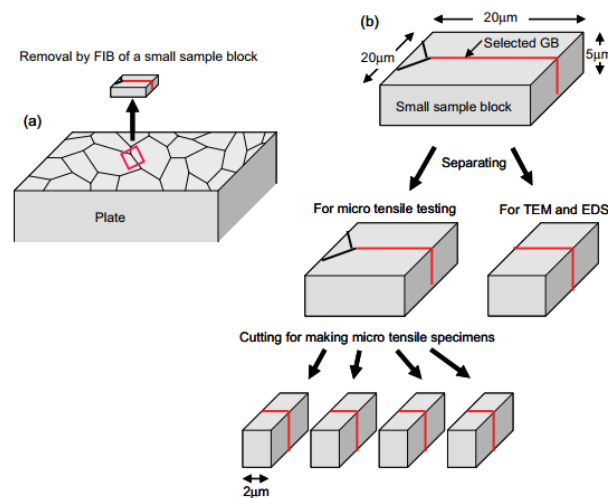


Fig. 2.10 – Illustration of FIB procedure for grain boundaries testing.

Recently Fujii and Fukuya [21] used FIB to obtain a $2 \times 2 \times 10 \mu\text{m}$ Fe-Mn-P alloy sample having one grain boundary and tensioned it by FIB system. Load

was measured from the deflection of the cantilever and the displacement was monitored in situ. In the research study, aged and unaged conditions were analyzed; in both cases, intergranular fracture occurred in a brittle manner and the fracture surface suggested a mode I. Fujii et al [28] used FIB micro-processing also for the characterization of alloy 600 oxidized grain boundary strength; in order to evaluate the exact stress in the specimen, they took into account the bending moment, given that the tensile axis inevitably shifted along the cantilever length. Fracture appeared to have occurred by mode I in a brittle manner in this research as well. Then stress normal to the grain boundary was calculated, that is likely to be a direct measure of the grain boundary strength.

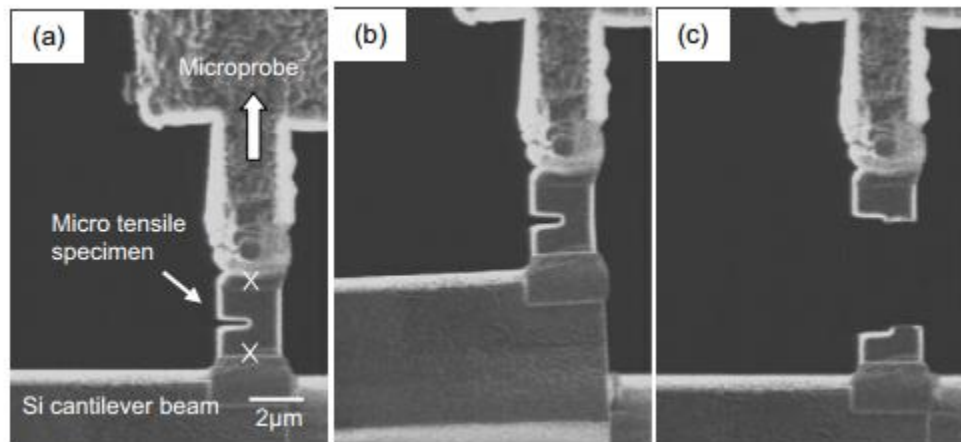


Fig. 2.11 – Summary of test for measuring the grain boundary strength.

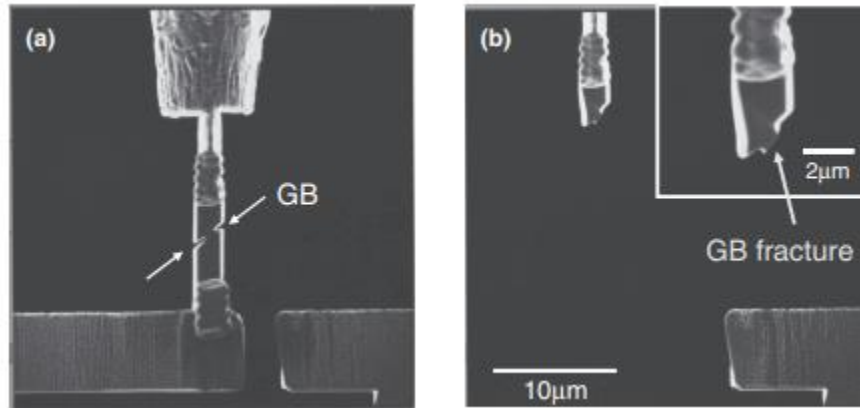


Fig 2.12 - Summary of test for measuring the grain boundary (45°) strength.

FIB has also been used to evaluate the bonding interface between cold sprayed coatings (copper) [23]. Cold spraying is a particle deposition process that permits to deposit different materials on a substrate, such as polymers, ceramics or metals [24-25]. This technique permits to obtain 1 mm thickness dense deposit, another advantage is that the material does not get affected thermally consistently [26-27]. Ichikawa et al [23] demonstrated that coating often present brittle properties; for this reason, crack propagation is supposed to occur on the interface. Usually FIB systems are reliable in revealing the stress state; on the other hand they cannot provide strain. The latter research can be considered innovative because a new setup was provided by combining FIB with image analysis applied to continuously recorded SIM (Scanning Ion Microscopy) images. As it can be seen in the fig. 2.13, the relative movement of A, B, P,Q and R positions can be measured and the elongation of the specimen can be obtained with $d_1 - d_2$, where $d_1 = d_{A,B} - d_R$ and $d_2 = d_{P,Q}$.

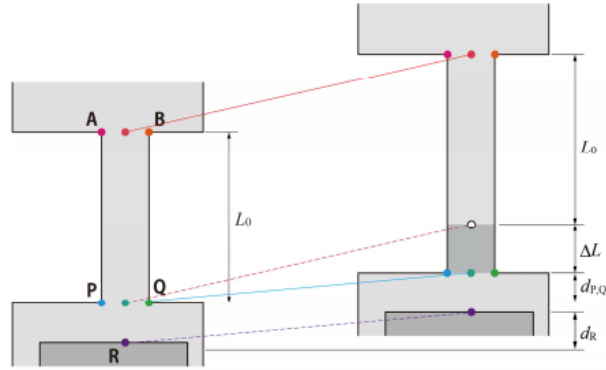


Fig. 2.13 – Method to obtain strain values

In this way, it is possible to obtain a coating stress-strain curve for the tensile test whose accuracy can be improved. The schematic diagram of their process can be seen in fig. 2.12, and the relationship between force and displacement is given by:

$$F = \frac{16 E w t^3 d}{l^3}$$

where E is the elastic modulus, l the length, w the width, and t the thickness of the sample. Based on [23], although macroscopically the material exhibited brittle behaviour, microscale test revealed the possibility of plastic deformation.

Chapter 3 Material, heat treatment and microstructure investigation

This chapter describes the material and the experimental procedure that has been used to obtain the samples and the steps performed in order to reveal the microstructure.

3.1 Material

The material used in the present study is commercially pure titanium. The latter has been bought in the form of a 0.25mm thick foil (99,5% Ti) from Alfa Aesar company.

3.2 Material fabrication

Dog-bone-shaped samples (Figure 3.1) have been obtained from these foils using wire EDM (Electrical Discharge Machining). This technique is an unconventional machining process that, by incorporating CNC controls, allows the cut of metals and other conductive materials. The electro-thermal system is composed of two electrodes: the wire and the workpiece. Since there is no contact between them (sparks are generated in the process that rapidly cut away the material), neither cutting forces nor deformations occur [28].

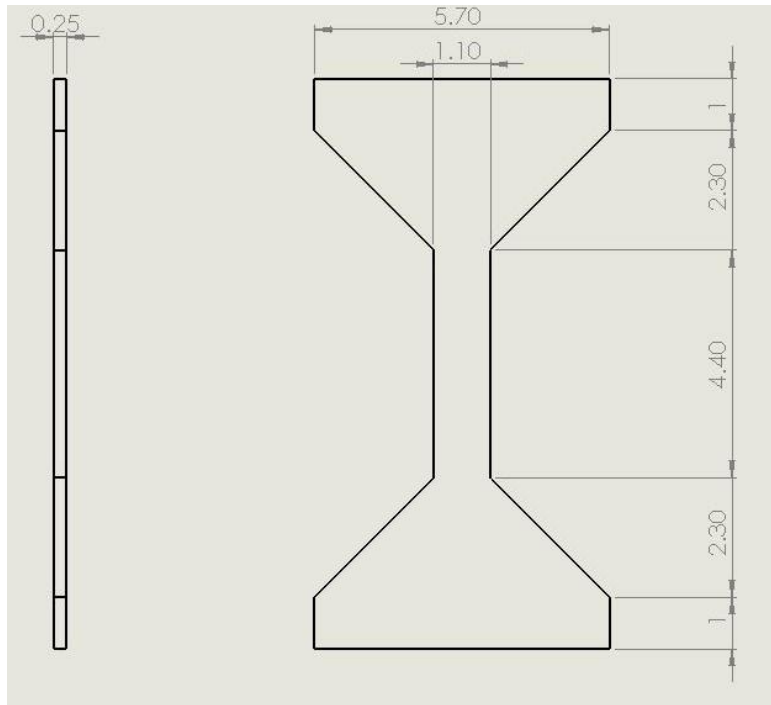


Fig 3.1 – Tensile dog-bone-shaped sample: side view on the left and front view on the right. Dimensions are in mm.

3.3 Annealing

Annealing is a heat treatment in which the material is brought to a temperature that is lower than the transition temperature α - β (883°C for CP Titanium), this means that the microstructure remains unchanged (HCP). In the process, grain growth occurs given that the total area of grain boundaries decreases; there will be fewer grains but their average size increases. In figure 3.2, it is possible to see how grain size is influenced by annealing temperature and time; in general, by increasing both of them, the grain size increases. Usually, this treatment is used to recover the deformed crystalline lattice that implies the elimination of residual deformations. Moreover, it gives the material a good ductility. [29]

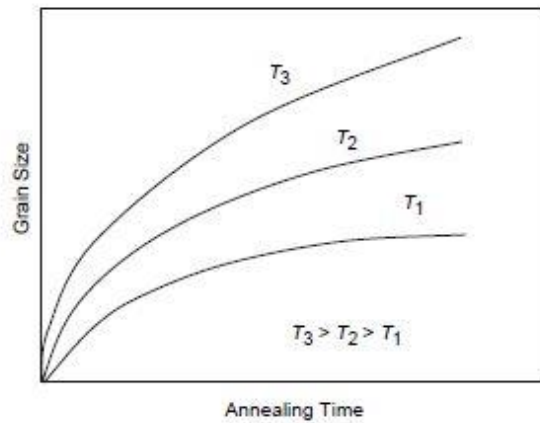


Fig 3.2 – Grain size vs Annealing time [30]

Table 3.1 – Effect of thermal treatment on the grain size in Commercially Pure Titanium [31]

TABLE 1. Effect of Thermal Treatment on the Grain Size* in Commercially Pure Titanium

Annealing temperature, °C	Annealing time, h	Grain size, μm
425	15	0,4; 0,5
425	20	0,4; 0,5; 0,6
450	10	0,6
500	3	2; 2,5; 2,5
520	0,67	2,5
550	1	3; 4
570	0,67	10
600	1	7
650	1	9; 14
700	0,5	11
800	0,33	30
800	1	17; 20; 35
800**	5	39; 43; 54; 58

* Grain size of annealed specimens in the as-forged state was ~ 0.4 μm.

** Thermal treatment was performed in vacuum.

Note: In all cases air-cooling was used.

Given that the present work is focused on the study of single grains and grain boundaries, the annealing has not been used to reach particular mechanical

properties, but rather to increase grain size and make the following cutting by laser micromachining easier.

It is well established that the average grain size in CP Titanium is around the order of magnitude of $10\ \mu\text{m}$ [32-33]. This means that in order to study the single crystal behaviour, one should be able to obtain a final gauge width equal to less than 10 microns which is quite arduous. For this reason, the annealing becomes an important step that makes the experimental procedure easier. In fact, after annealing, the average grain size is approximately $90\ \mu\text{m}$.

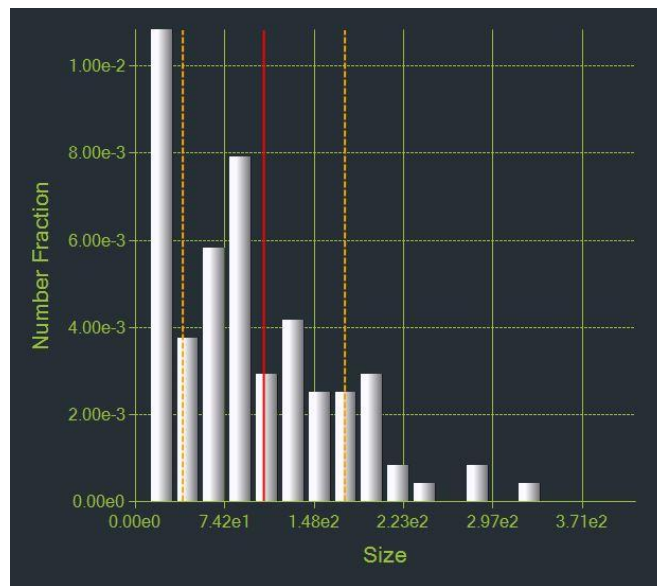


Fig 3.3 – Number Fraction vs Size [μm] in one sample analyzed: the red vertical line indicates the average grain size that is $\sim 90\ \mu\text{m}$.

The treatment has been realized with the furnace that can be seen in Fig 3.4. The annealing data presented in Table 3.2 come from Marina Pushkareva research paper [35].

Table 3.2 – Annealing data

Annealing data	
Temperature [°C]	870
Pressure (vacuum) [Torr]	10^{-6}
Time [h]	36



Fig 3.4 – Furnace used for the heat treatment: starting from right it is possible to see the chamber, the turbo pump and the pressure gauge.

After setting up the furnace, the samples are placed on a little ceramic holder. The latter is then placed inside the ceramic tube that is located in the chamber. The heating curve obtained from the process can be observed in Fig. 3.5.

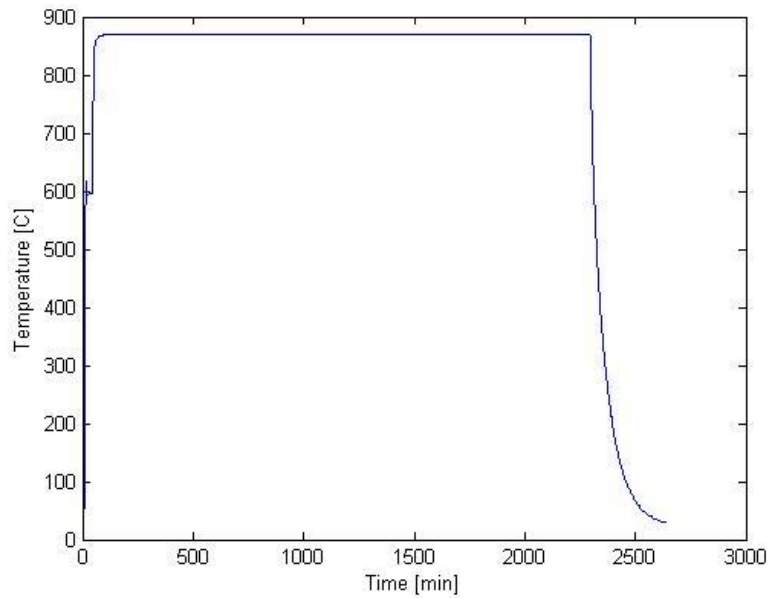


Fig 3.5 – Annealing curve

3.4 Metallographic preparation

After the annealing treatment, samples were prepared metallographically by chemical-mechanical polishing in order to observe microstructure and prepare sample surface for EBSD (Electron Back Scattered Diffraction) analysis.



Fig 3.6 – Automatic polishing machine used for metallographic preparation: Allied MetPrep 3 Grinder/Polisher with Power Head (right) and AD-5 Fluid Dispenser (left)



Fig 3.7 – Way to plug the sample holder into the Power Head [35]

In Fig 3.7 it is possible to see the sample holder: macro samples are usually kept still with screws, but given that the samples analyzed in this research are thin and fragile, they were glued (with super glue) on the top of aluminum cylinders and then let dry for hours. The latter cylinders were then kept still by the visible screws in the figure.

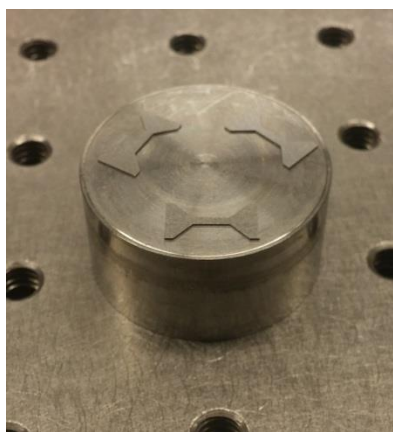


Fig 3.8 – Samples disposition on the cylinder

Table 3.3 Grinding/Polishing data

Steps	Cloths/ lubricant	Load [N]	Speed [RPM]/ direction	Time [min]
Grinding	P1200 SiC paper / water	25	240(platen) 50(holder) / complementary	15-30 sec Until plane
Polishing	9 μm Anamet ultrapolishing / diamond suspension	25	150 (platen) 50(holder) / contrary	10
Polishing	0.06 μm Mastermet / Colloidal silica:Hydrogen peroxide (5:1)	20	150(platen) 150(holder) / contrary	10

The samples were first ground using SiC paper with a continuous water flow until the sample surface was plane. Then the samples were polished using a 9 μm diamond spray on an ultrapolishing cloth. Final polishing was performed with 0.06 μm Struers OP-S suspension on Microcloth/Buehler cloth with an attack polishing agent (1:5 of hydrogen peroxide and colloidal silica). Between the steps, samples were put in an ultrasonic bath for 5 minutes in water, then rinsed in alcohol and finally a fast dry with air flow. After the last step, A Nikon OPTIPHOT-100 optical microscope was used for microstructure examination at different magnifications.

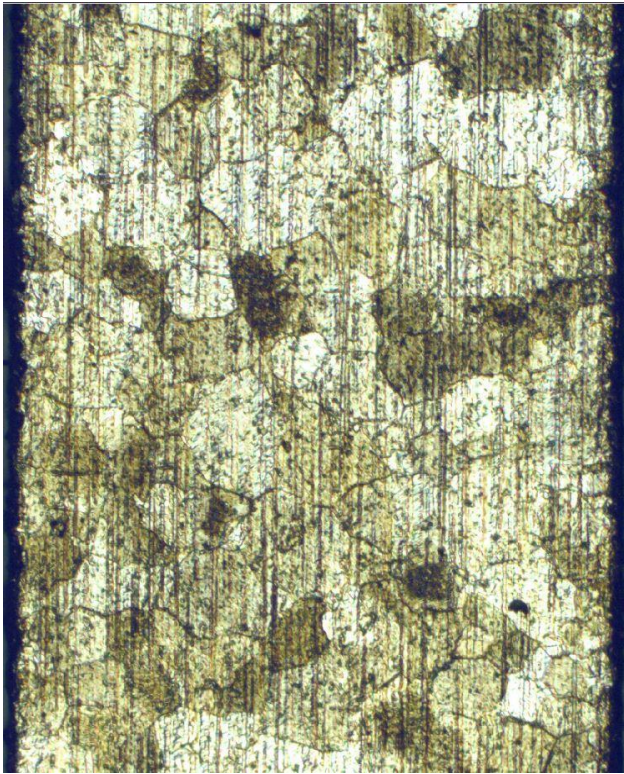


Fig 3.9 left - Specimen surface after annealing and before polishing steps.

Fig 3.10 right - Specimen after polishing steps.

After the steps, the cylinders (with the samples on top) were placed in a glass filled with acetone overnight in order to unglue the samples. This step could usually bring undesired blue spots (acetone residuals) on the surface. By dipping the samples in an ultrasonic bath for 5 minutes with acetone, then rinsing them with acetone and finally drying them with a fast air flow, their surfaces go back to the state visible in Fig 3.10.

The load during polishing is kept constant thanks to one of the black little columns that comes down from the power head of the machine that presses the cylinder (and subsequently the samples) against the SiC paper (in the first step) or against the ultrapolishing cloth (in the second or third step).

The use of automatic polishing machine also permits to control the speed of the sample holder and the speed of the cloth, the lubricant flow by setting the pulses/min and the length of a pulse.

The steps in Table 3.3 gave great polishing results and they were obtained after several trials and by consulting giants of the field such as Struers and papers on specimen preparation for EBSD [36-37].

Chapter 4 From EBSD to the gauge configuration

This chapter describes the EBSD analysis and the way the tested grains are chosen from the EBSD maps. Finally, the femtosecond laser micromachining process is explained.

4.1 EBSD (Electron Back Scattered Diffraction)

EBSD is a microstructural-crystallographic characterization technique that provides quantitative information about any crystalline or polycrystalline material such as: grain size, grain boundary character, grain orientation, texture and phase identity of the sample under the beam. Experimentally, this technique is performed in a scanning electron microscope (SEM) and other accessories that can be attached to it. The SEM is usually equipped with an EBSD detector that contains a CCD camera, a phosphor screen and a compact lens [38-39-40]. A schematic arrangement of an EBSD layout is given in Figure 4.1.

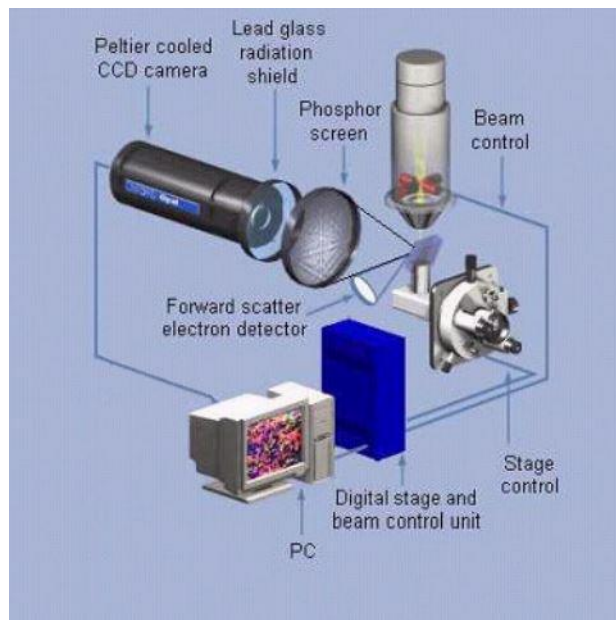


Fig 4.1 – Schematic layout of EBSD system [41]

and tensile direction and it is positive downward, the X axis corresponds to the horizontal direction and it is positive to the right. Consequently, the Z axis is positive “into the screen”.

The software also provides the Euler angles which are three angles introduced by Leonhard Euler that are useful to describe the orientation of a rigid body with respect to a fixed coordinate system [42]. More simply, these angles help in distinguishing the various grains orientations.

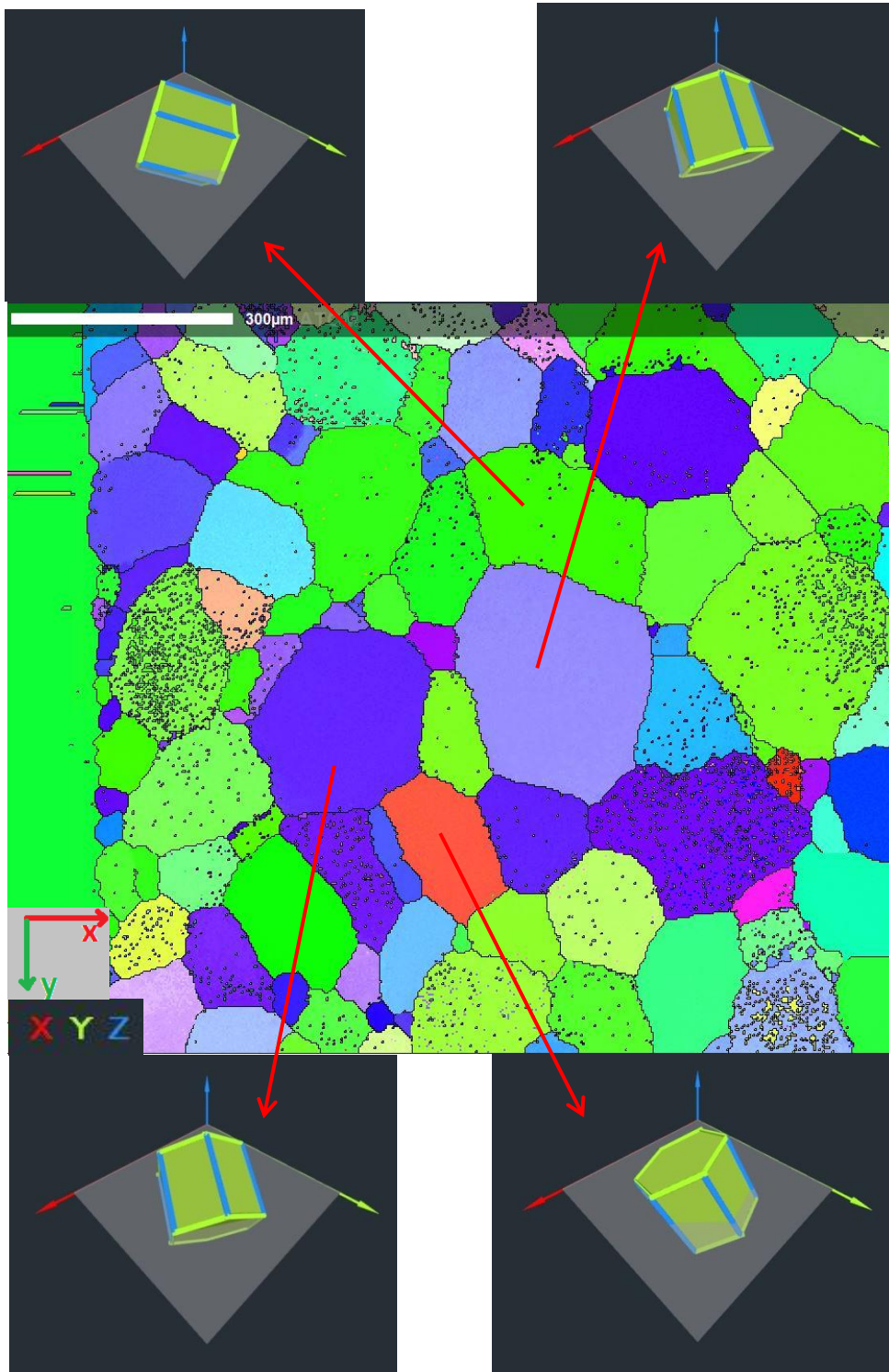


Fig 4.3 – EBSD map on top left; the red arrows show the orientations of the indicated grains.

Euler angles are typically denoted with Φ , Θ and Ψ .

It is possible for ATOM to provide the three Euler angles of any grain by making grain detection and by clicking on the grain of interest. For example, by analyzing the big grain in the center of Fig 4.3, the three Euler angles are (as can be seen in Fig 4.4):

- $\Phi = 152.43^\circ$
- $\Theta = 117.6^\circ$
- $\Psi = 49.32^\circ$

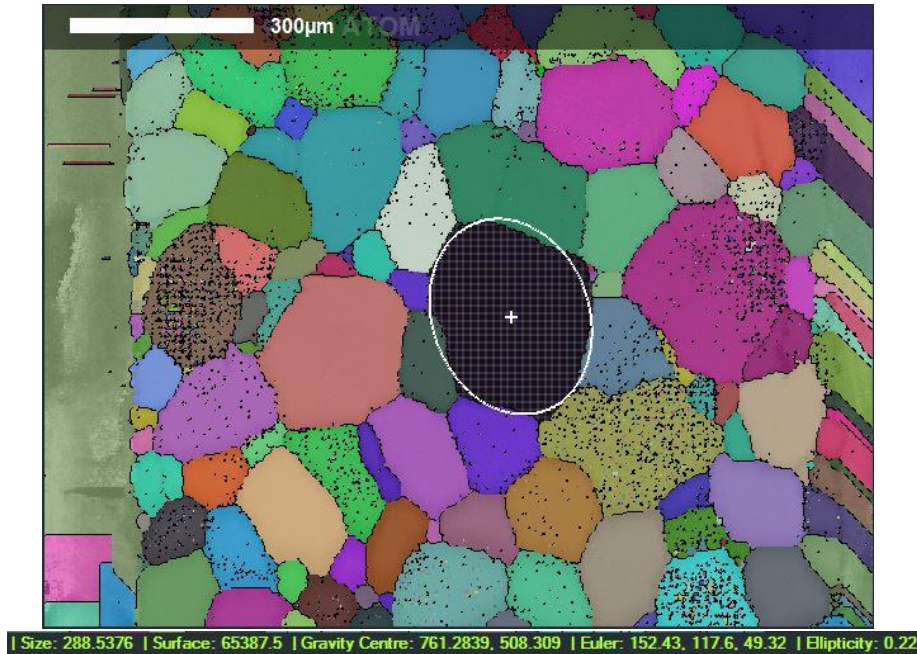


Fig 4.4 – Grain information. Size is in μm . Surface is in μm^2 .

Considering a fixed coordinate system X_0 - Y_0 - Z_0 : the first Euler angle Φ represents the rotation around Z_0 , the second Euler angle Θ describes the rotation around the new X axis (X_1) and, finally, the third Euler angle Ψ

provides the rotation around the new Z axis (Z_2). What is written above can be verified in the next figure (Fig. 4.5)

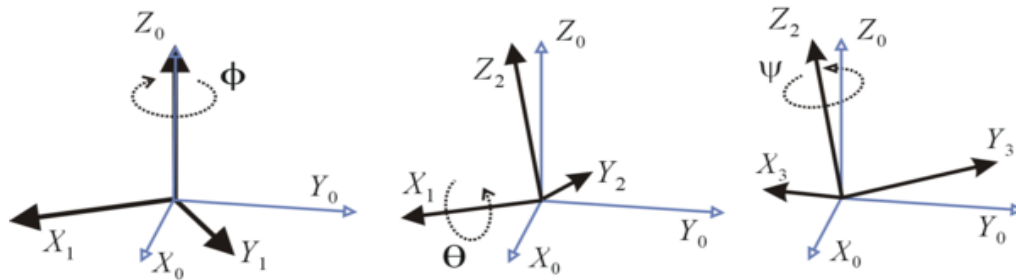


Fig 4.5 – Schematic arrangement of the Euler angles. [43]

ATOM also provides the grain boundary misorientation angle between two grains (see Fig. 4.6).

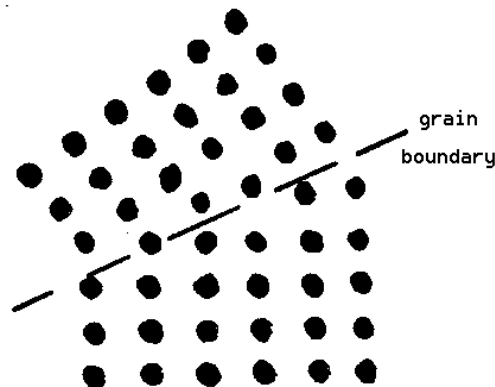


Fig 4.6 – Example of grain boundary with reference to the atomic dispositions of the two grains. []

An example of EBSD map (Fig 4.3 EBSD map) with grain boundaries misorientation angles is given in Fig 4.7.

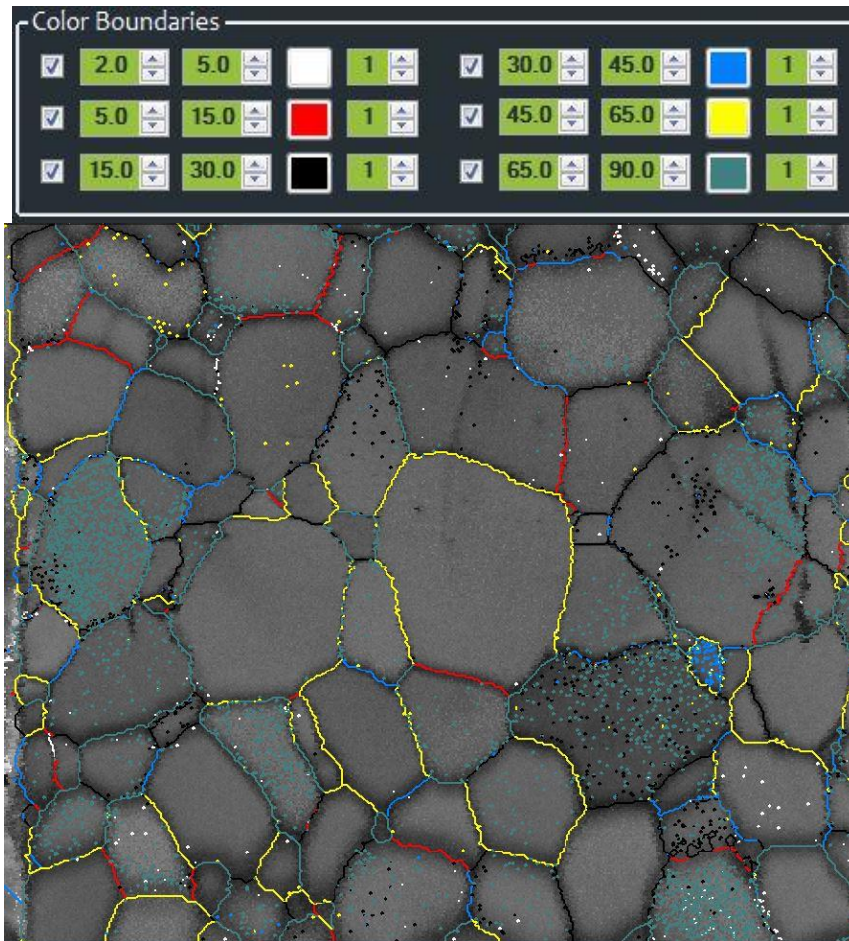


Fig 4.7 EBSD map with reference to the grain boundaries misorientation angles. On the top: colours legend.

For example, yellow grain boundaries have misorientation angle included from 45° to 65° .

4.1.1 From the EBSD map analysis to the sample final shape

The sample shape in Fig 3.1 is not the final one because it contains, in its gauge length, many grains. In order to study the single grain (Fig 4.9) or a single grain boundary that separates two single grains (Fig 4.10), another modification to the sample shape is required. This further modification is obtained through ablation of material with the femtosecond laser machining technique that is described further on. In Fig 4.8, the final outcome can be noticed (the dimensions will be provided in the appropriate paragraph).

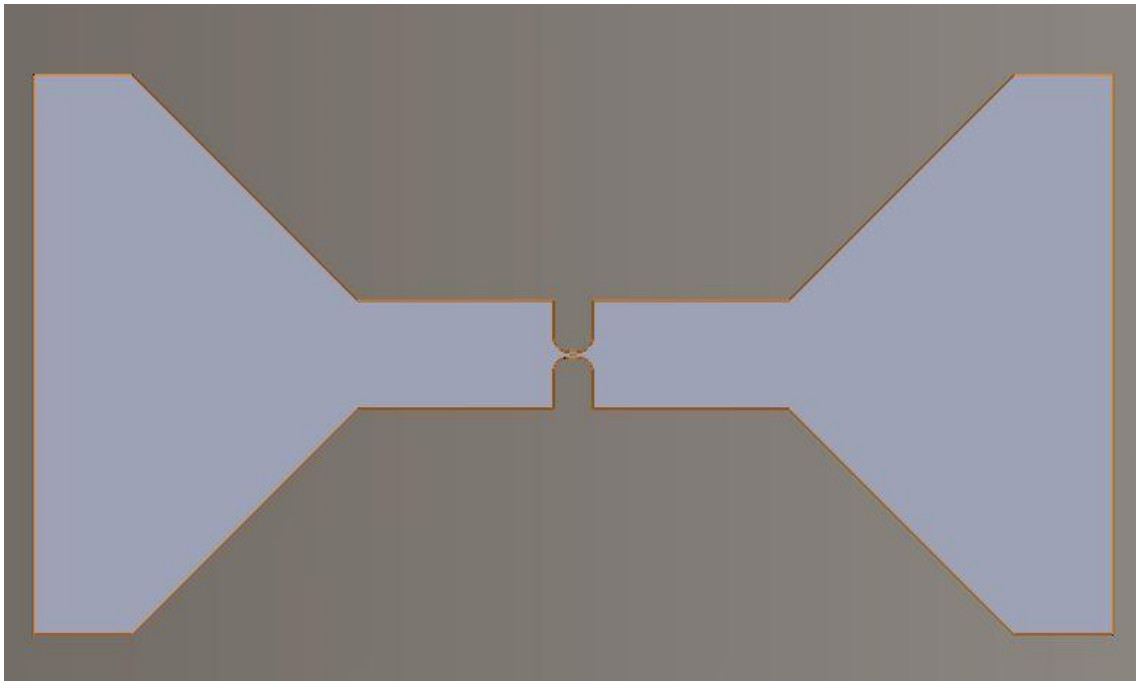


Fig 4.8 – Samples final shape.

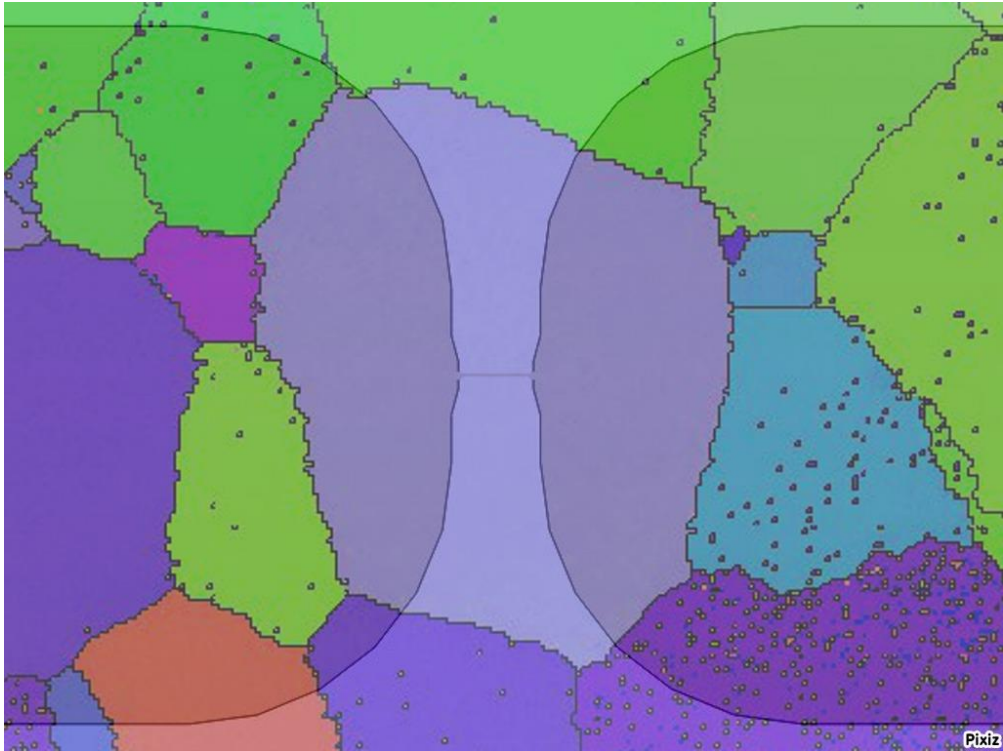


Fig 4.9 – Configuration 1.

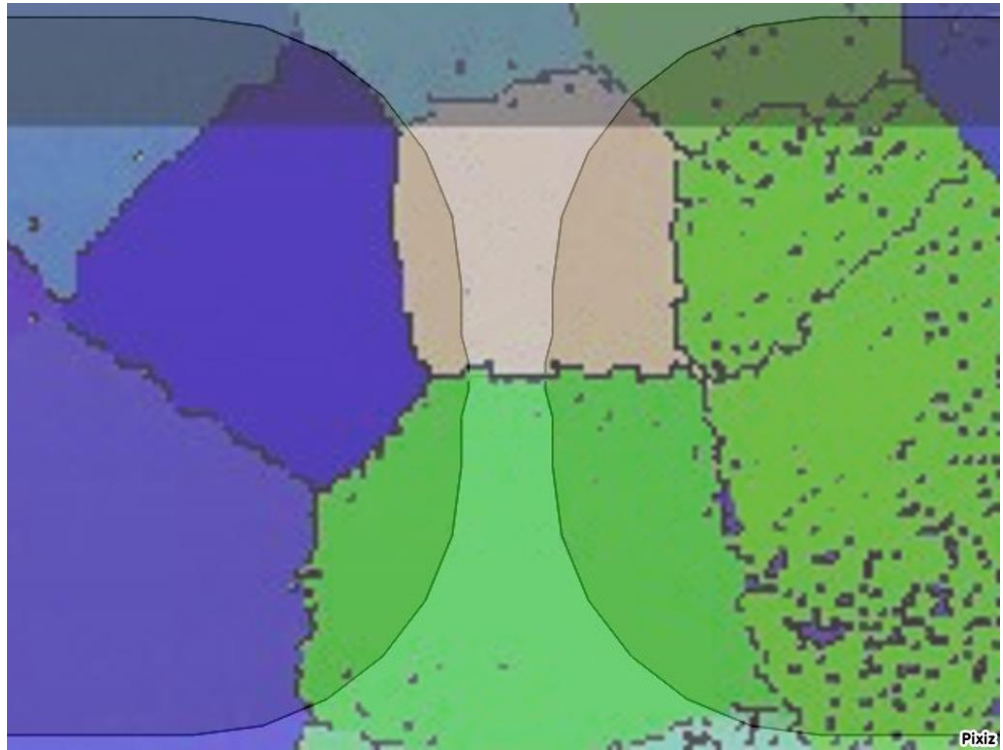


Fig 4.10 – Configuration 2.

In Fig 4.9, the gauge length only contains one grain that is chosen depending on its orientation. In Fig 4.10, the gauge length contains two grains divided by a perpendicular grain boundary to the tensile axis; the grain boundary misorientation angle plays, in this case, an important role. If the first configuration only allows the study of the mechanical properties of the chosen grain, the second configuration permits to study two grains at a time and offers the possibility to examine the deformation of the grain boundary and the typology of fracture: intergranular or transgranular. The first configuration was only used for one sample (called “A2”): the presence of a big grain perfectly located in the middle of the specimen width and the lack of a perpendicular grain boundary to the tensile axis led to this choice.

4.2 Femtosecond laser micromachining

Femtosecond laser micromachining is a high resolution machining process that has emerged in the last few decades thanks to its applicability and to its numerous advantages. Femtosecond lasers allow material removal through ablation and micro/nano structures can be realized. Ablation occurs via fast creation of vapour and plasma and almost no heat affected zone [44]. Moreover, structural changes do not occur and the sample is characterized by smooth edges (no significant recast layer). The latter advantages are not possible with lasers with longer pulse durations which produce significant melting that implies heat affected areas [45-46-47-48]. Other advantages can be found in [49]. Fig. 4.11 enounces the differences between microsecond and femtosecond lasers.

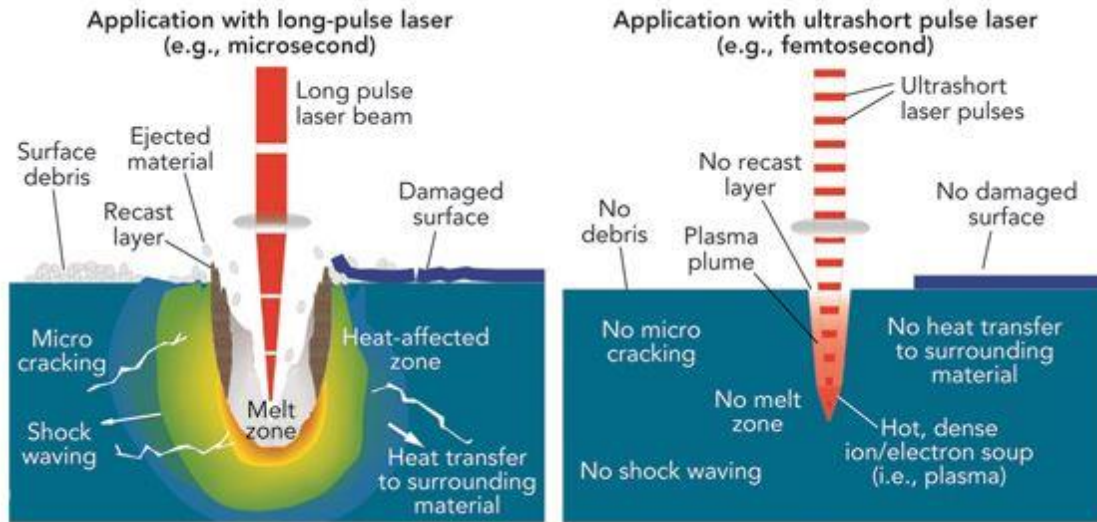


Fig 4.11 – The effects of an ultrashort pulse laser compared to a long-pulse laser.

Some important parameters that are used to describe femtosecond lasers include the pulse duration [tp], the pulse repetition rate (PRR) [Hz] and the average power P of a laser beam measured by a power meter [W]. The single pulse energy E [J] is calculated with the following relation:

$$E = \frac{P}{PRR}$$

The setup that has been used for laser machining is presented in Fig 4.12: the laser is guided to the shutter by a set of lenses. Hence, the laser follows the red lines towards the objective that focuses the beam on the sample. By developing scripts in G-CODE, it is possible to machine the sample to its final shape.

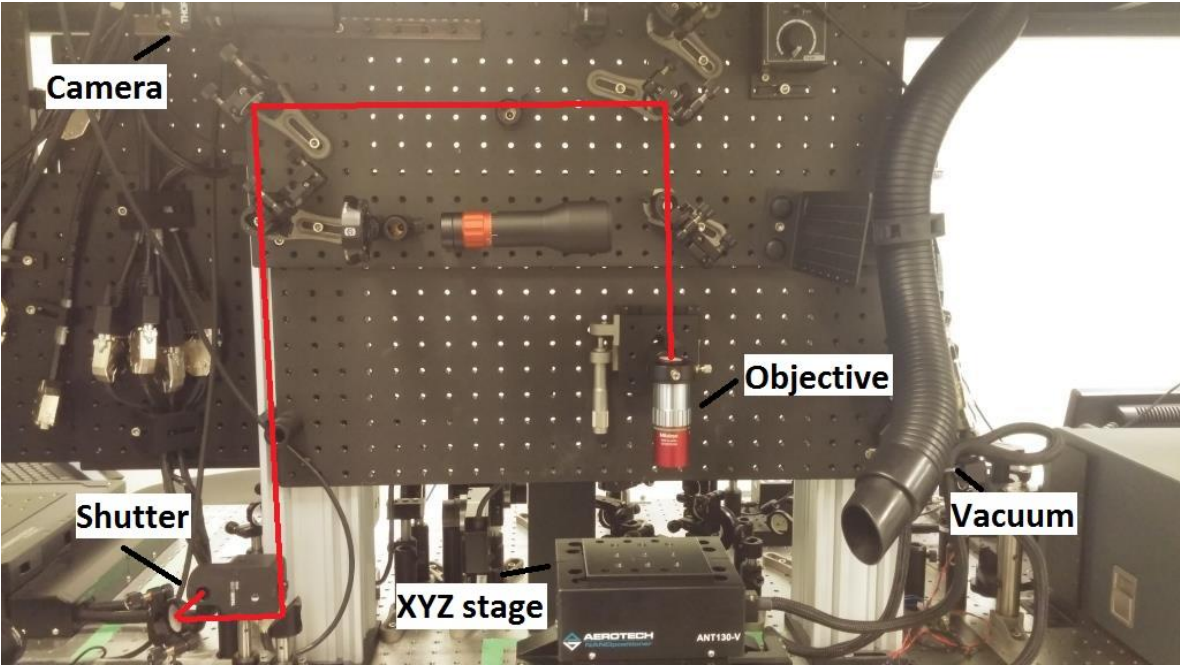


Fig 4.12 – Laser micromachining setup

4.2.1 Machining steps

Step 1

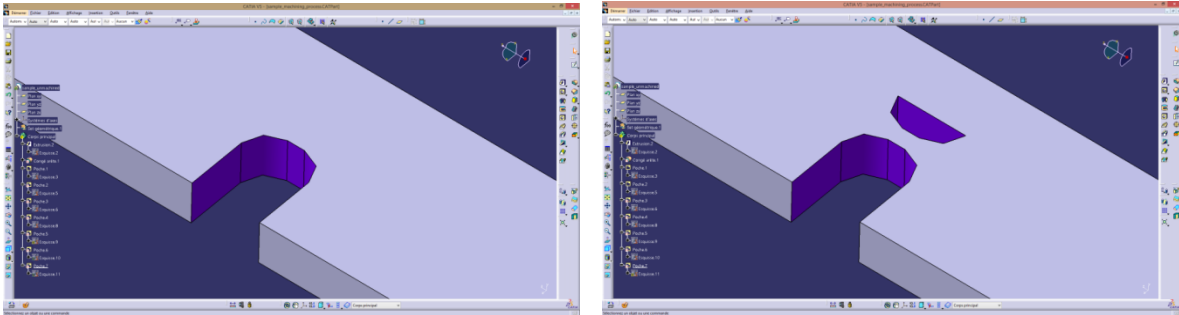


Fig 4.13 – Part 1 micromachining

In step 1, a first script has been developed to machine the sample as in Fig 4.13 (right) from the top view with a 5x objective using the following parameters:

- PRR = 10 KHz
- P = 700 mW
- Machining speed = 80 $\mu\text{m/s}$
- Width of the gauge (Fig 4.13 right) at the end of part 1 = 100 μm
- E = 0.07 mJ

The beam has to go through 100-150 μm that corresponds to the thickness of the polished sample (the initial thickness was 250 μm , but the polishing steps reduce it to 100-150 μm).

Step 2

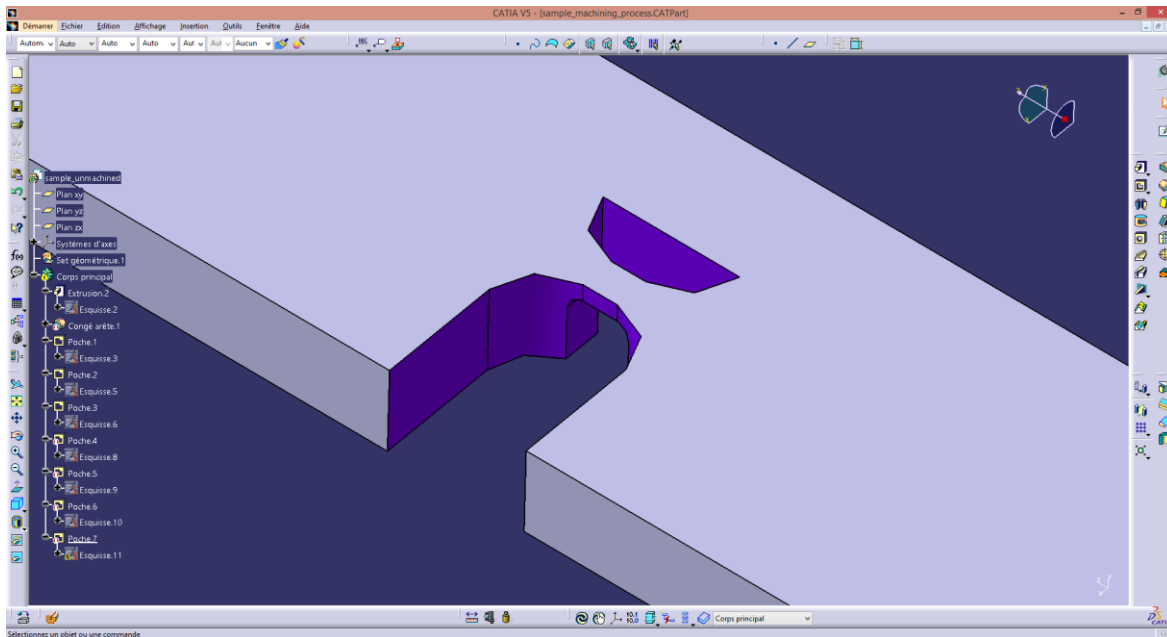


Fig 4.14 – Part 2 micromachining

In step 2, the sample is rotated by 90° to be machined on its side with a 20x objective (Fig 4.14). The parameters are as follow:

- PRR = 10 KHz
- P = 250 mW
- Machining speed = $80 \mu\text{m/s}$
- Thickness of the sample (Fig 4.14) at the end of part 2 = $50 \mu\text{m}$
- E = 0.025 mJ

Step 3

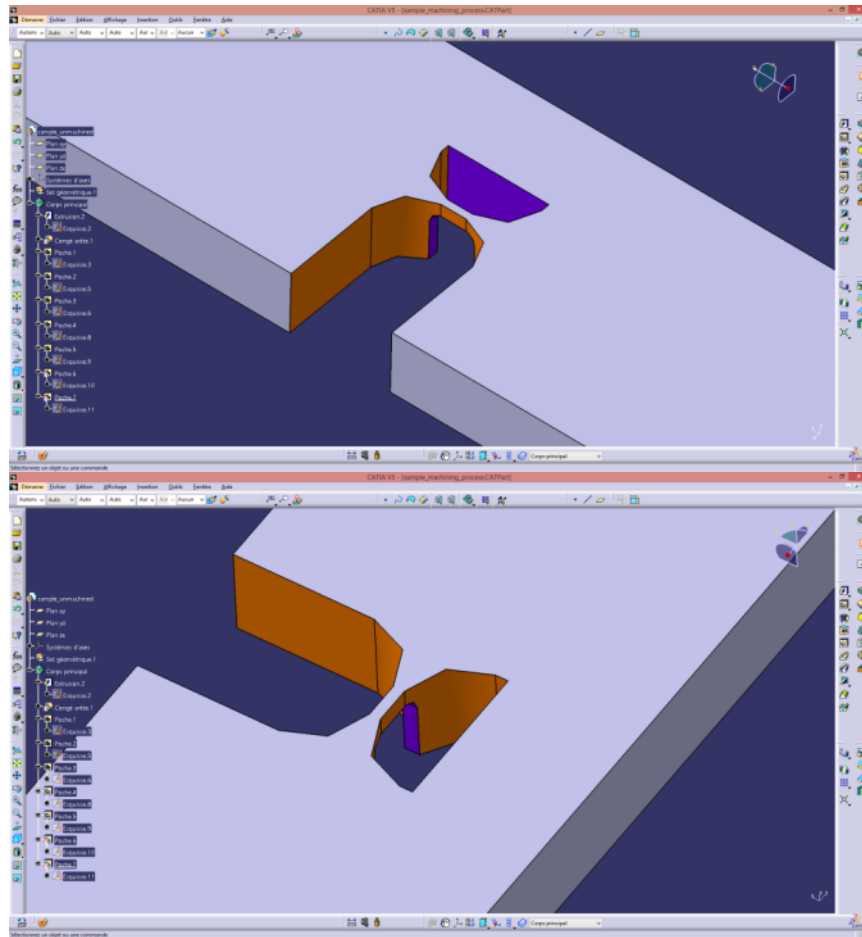


Fig 4.15 – Part 3 micromachining

In step 3, the sample is again machined from the top view, but with a 20x objective to increase accuracy (Fig. 4.15). The parameters are as follow:

- PRR = 10 KHz
- P = 100-150 mW
- Machining speed = 80 $\mu\text{m/s}$
- Width of the sample (Fig 4.15) at the end of part 3 = 30-50 μm
- E = 0.01-0.015 mJ

Step 4

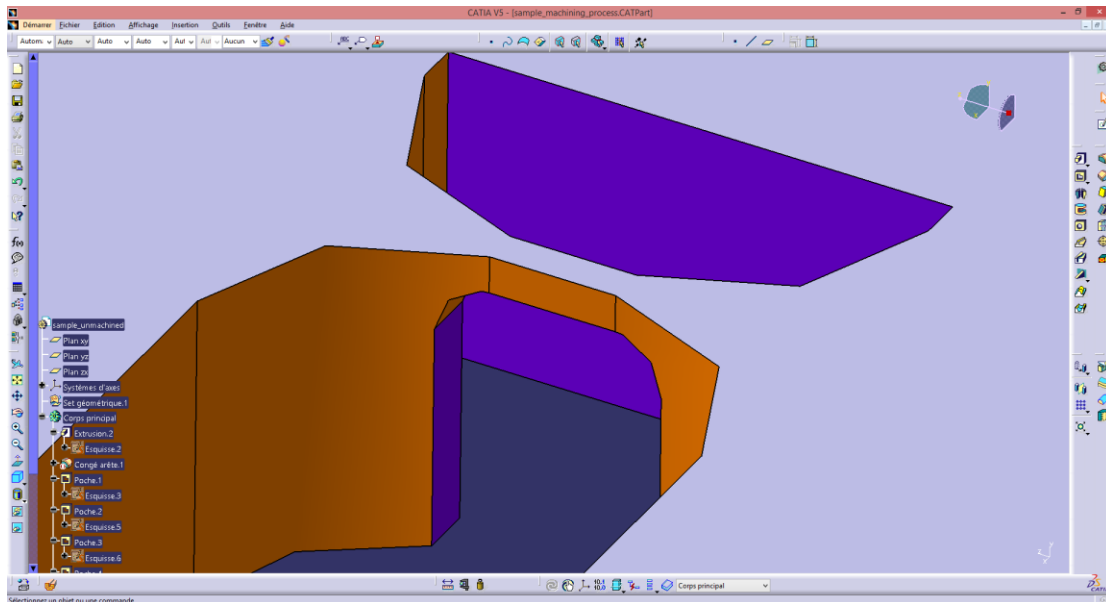


Fig 4.16 – Part 4 micromachining

In the final step, the sample is once again machined on its side with a 20x objective (Fig 4.16) using the following parameters:

- PRR = 10 KHz
- P = 100-150 mW
- Machining speed = 80 $\mu\text{m/s}$
- Thickness of the sample (Fig 4.16) at the end of part 4 = 24-30 μm
- E = 0.01-0.015 mJ

As it can be seen in the previous pictures, there is still a part that needs to be removed to complete the sample machining. In the four steps, the specimen was placed over a rotating support, so that both width and thickness of the sample can be machined. After, with a suction pen, the sample is placed on the tensile machine (the part that not has been removed yet helps to avoid deformation of the gauge length). Once the sample is on the tensile machine,

the latter is placed on the 3D stage to finally remove the part of the sample that is no longer needed.

4.2.2 Gauge dimensions

- Gauge length = 100 μm
- Gauge width = 30 - 50 μm
- Gauge thickness = 24 - 30 μm

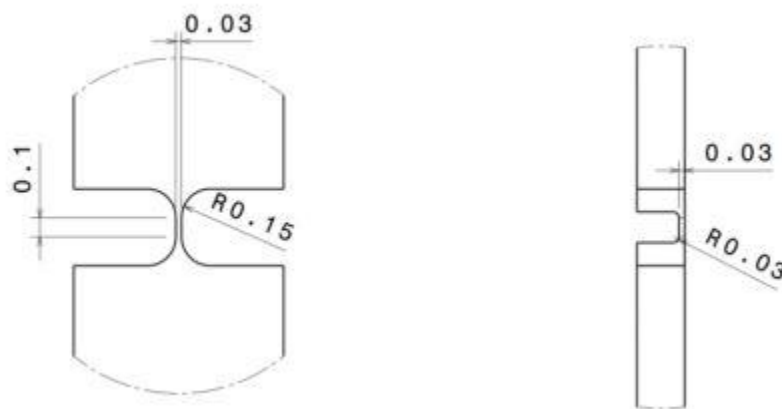


Fig. 4.17 – Gauge dimensions. Dimensions in mm.

Fig. 4.17 shows the front view (left) and the side view (right) of the gauge of the sample. The dimensions about the gauge length and the two curvatures are fixed. On the other hand, as already mentioned, the width and the thickness vary from sample to sample.

Chapter 5 Data acquisition

This chapter describes the tensile testing and data post-processing procedures, such as the use of digital image correlation (DIC) technique to measure the extension and compute the strain, in order to obtain the stress-strain curves.

5.1 Tensile testing

Tensile testing is an important technique for materials characterization in which a sample is subjected to a controlled tension loading until failure [50]. Important properties such as the yield strength, ultimate tensile strength, Young's modulus, Poisson's ratio are defined from the test. It is usually used to study isotropic materials (same properties in any direction). However the single crystals are anisotropic; and therefore it is expected to see different mechanical properties by analyzing crystals with different orientations with respect to the tensile axis.

The Engineering strain is found using the relation:

$$\varepsilon = \frac{L_F - L_G}{L_G}$$

where ε is the engineering strain, L_G is the gauge length, L_F is the final length.

The engineering stress σ_e is then calculated with the following equation:

$$\sigma_e = \frac{F}{A_i}$$

where F is the load applied on the tensile sample and A_i is the initial cross-sectional area. During the test, the gauge length tends to stretch while the thickness and width decrease (conservation of volume). This phenomenon

implies a reduction of the cross sectional area that decreases more and more until fracture of the sample in the neck.

The true stress σ_t is obtained with the following equation:

$$\sigma_t = \frac{F}{A_t}$$

where A_t is the real cross sectional area.

In some samples (such as “A3”, “A7”, “A8”), the gauge width is not constant because of a round part created by the laser in the middle. In such cases, the correction formula by Bridgman [51] has been used to revise the overestimated true stress values due to stress triaxiality.

The load data (F values) are obtained from the load cell of the micro tensile machine visible in Fig. 5.1. A load cell of 500g maximum capacity is used (Model 31 Honeywell load cell) and the actuator is a PI-Micros LPS-45 Vacuum piezo motor.

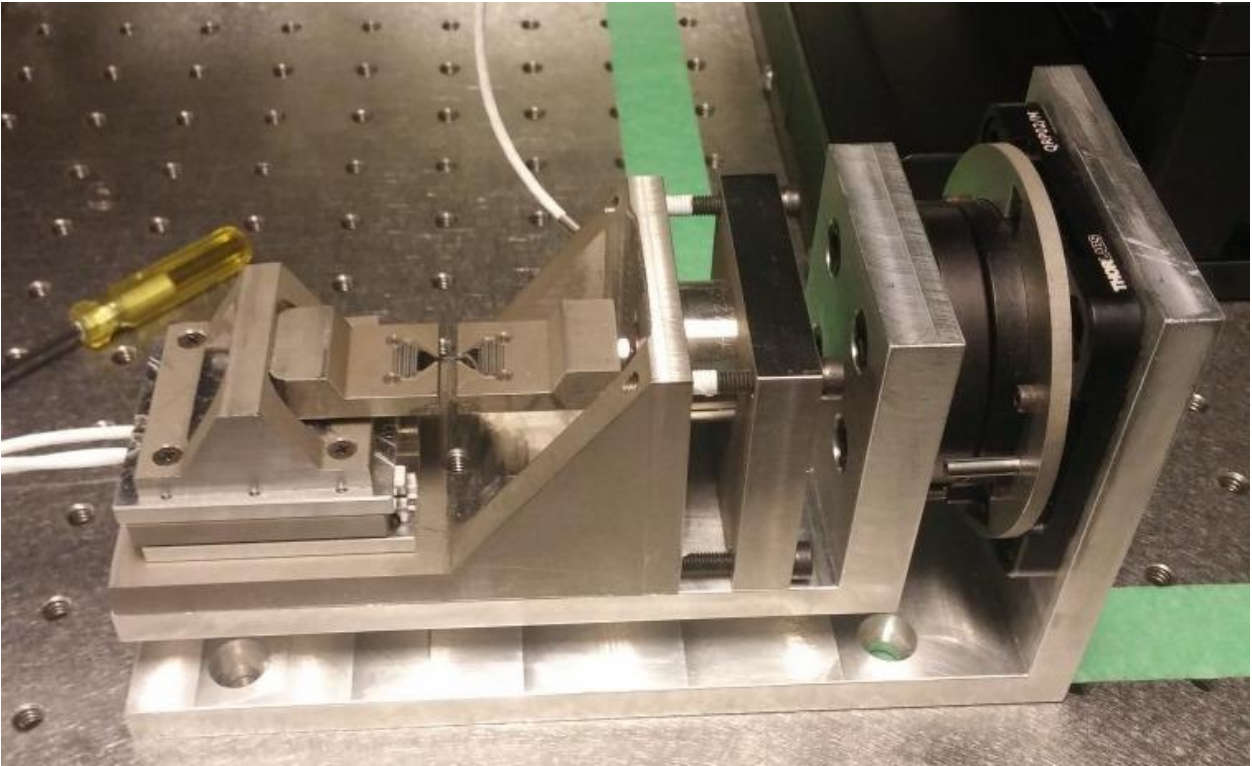


Fig. 5.1 – Micro tensile tester

The tensile test has been realized under a Keyence Digital Microscope VHX-5000 with the following precautions:

- Pulling speed = $0.1 \mu\text{m/s}$
- Acquisition of 1 picture every 10 seconds



Fig 5.2 – Tensile test setup

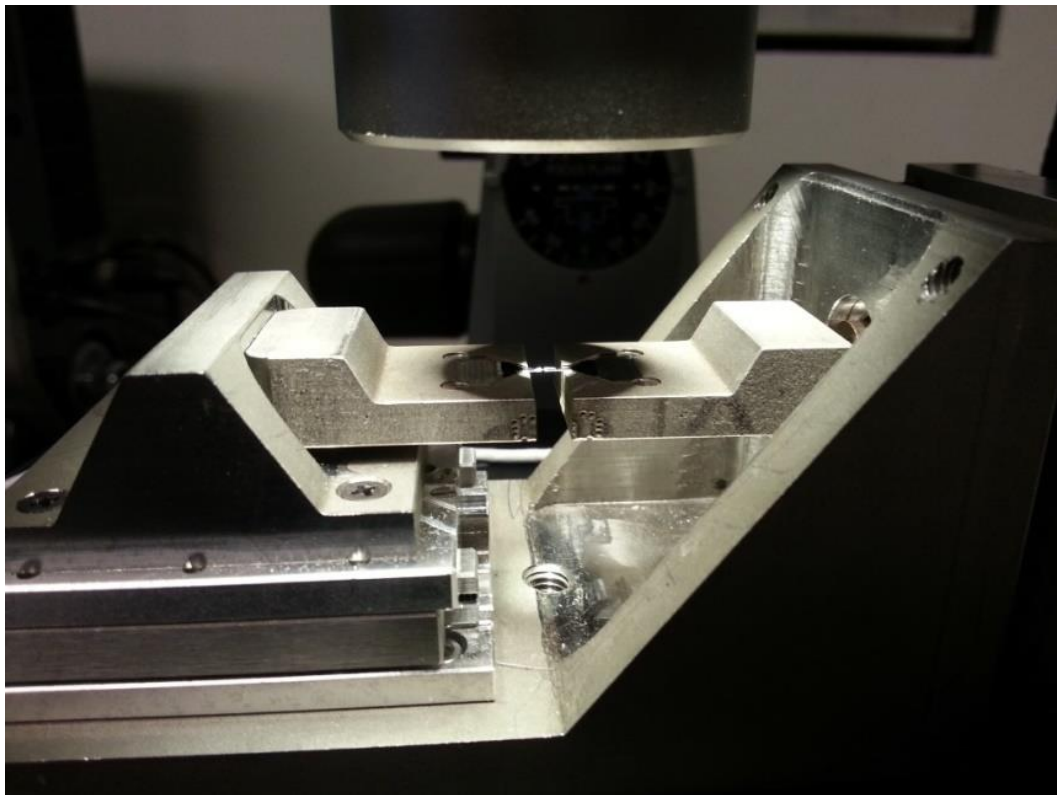


Fig 5.3 – Sample in tension under Digital Microscope

At the end of test, many pictures are available and can be related to a load value and, consequently, to an engineering stress value since the initial thickness is known from the laser micromachining last step and the digital microscope allows to obtain the initial width (initial cross sectional area is consequently known). In order to know the thickness and width values for each picture and therefore to know the true stress values, strain measurements are required.

5.2 Strain measurement with DIC

Digital Image Correlation (DIC) is an optical technique for measuring strain and displacement. By tracking blocks of pixels, a DIC system can measure displacements and build 2D or 3D strain maps. To properly track the deformation of the sample, it must be prepared with a random pattern which is called “speckle pattern”. In the present research, the first picture is taken before the beginning of the tensile test and its pattern obviously represents the un-deformed configuration. The pictures taken during the test express random patterns in deformed configurations which are then compared to the previously captured pattern in order to make DIC software calculate 2D strain maps. [52]

Two types of speckle patterns have been tried in this study:

- Random array of dots (about 1 μm diameter) filling the gauge length (Fig 5.4) obtained with laser micromachining after the Step 4 with PRR = 1 KHz and using a threshold power value.

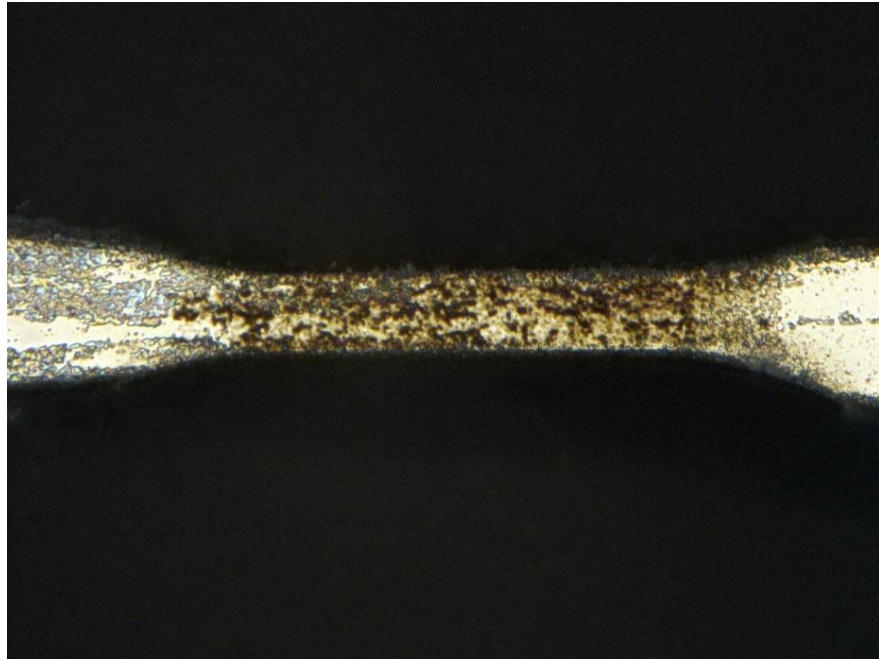


Fig 5.4 – Random array of dots

- Random pattern obtained exploiting the superficial debris caused from the laser machining (Fig 5.5).

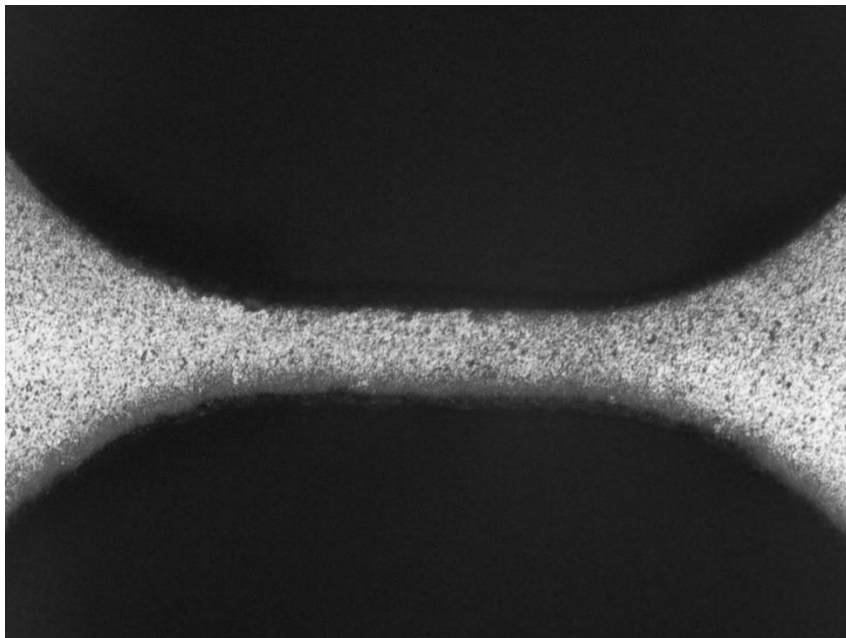


Fig 5.5 – Random pattern caused from machining debris

Both techniques worked on Davis LaVision which is the software that has been used for the analysis. For this reason, the second type of pattern was preferred because of its simplicity.

Davis LaVision permits to focus the attention on regions of interest such as: a region where a grain boundary or a single crystal is present, or a region where the fracture happens. By selecting a particular area of the gauge length, the software can average the longitudinal strain (on Davis ϵ_{xx}) and the transverse one (on Davis ϵ_{yy}); assuming the conservation of the volume, it is possible to know ϵ_{zz} using to the following relation:

$$\epsilon_{xx} + \epsilon_{yy} + \epsilon_{zz} = 0$$

By knowing ϵ_{yy} and ϵ_{zz} , it is possible to know the variation of the analyzed area step by step from the beginning of the tensile test to the end. For instance, if the picture number n is being analyzed in a particular cross sectional area, this selected area will be given by the following equation:

$$A = w(1 + \epsilon_{yy})t(1 + \epsilon_{zz})$$

Where w and t are respectively the width and the thickness of the analyzed cross sectional area A. ϵ_{yy} and ϵ_{zz} have negative values.

Chapter 6 Experiments

6.1 Single grain in tensile gauge (Configuration 1 Fig. 4.9)

6.1.1 Sample “A2”

The EBSD map corresponding to this specimen is presented in Fig 6.1.

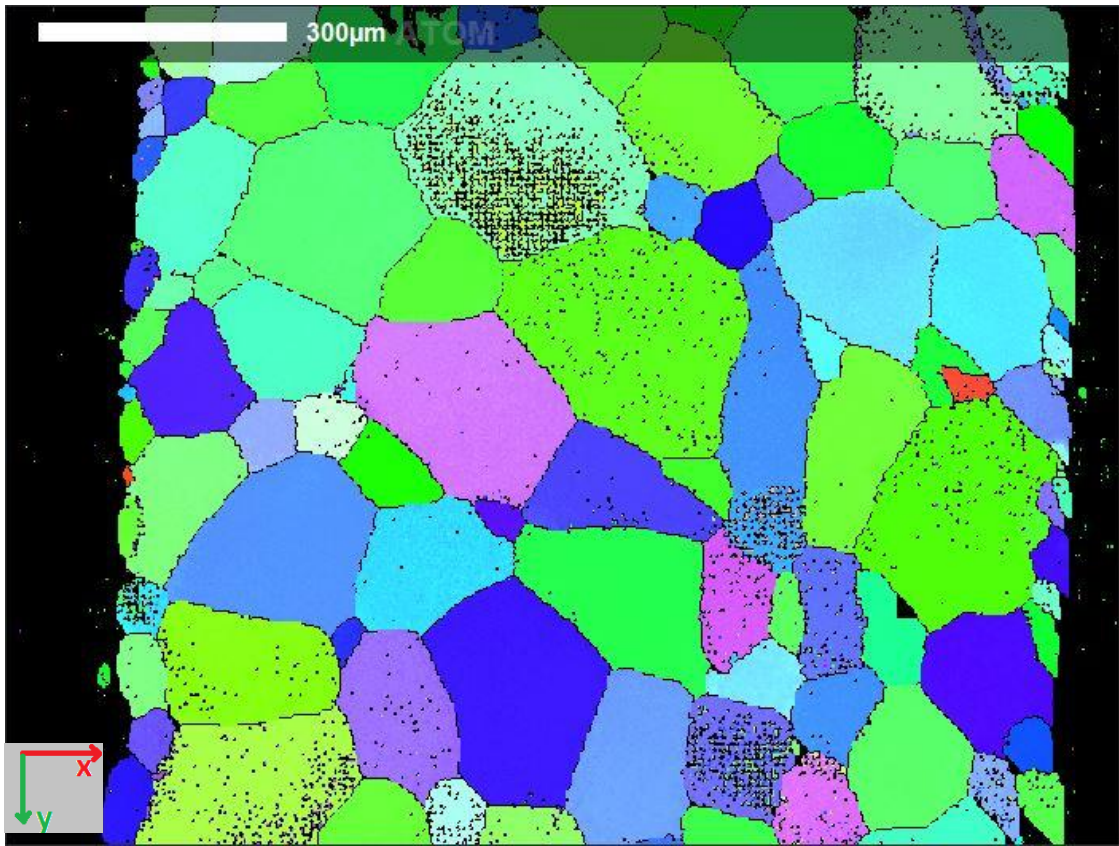


Fig 6.1 – EBSD map sample “A2”

The single crystal, that has been chosen for the analysis, can be observed in Fig 6.2.



Fig 6.2 – Crystal chosen for the test

The Euler angles of the given crystal are:

- $\Phi = 41.71^\circ$
- $\Theta = 65.17^\circ$
- $\Psi = 27.31^\circ$

As already said, these angles describe its orientation with reference to the tensile axis (vertical axis in the EBSD map, horizontal axis in the next pictures that summarize the tensile test) which is the green one.

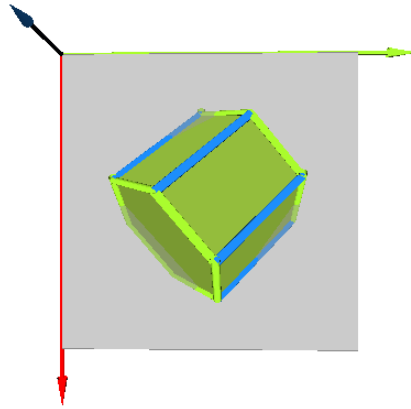
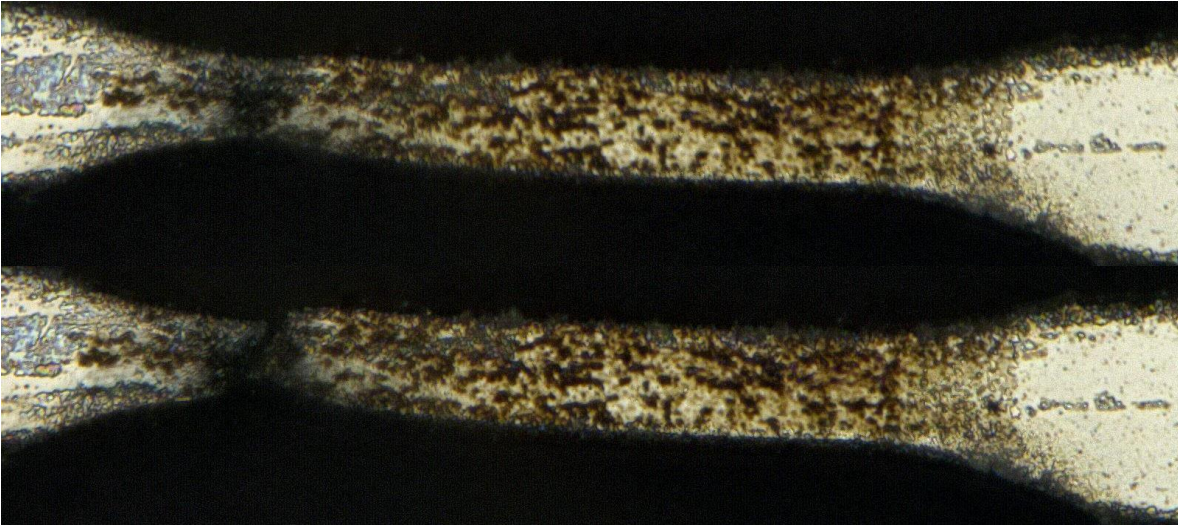


Fig 6.3 – Orientation of the chosen crystal. Green axis = Tensile axis

Sample “A2” in the un-deformed configuration is visible in Fig 5.4. After laser micromachining, its dimensions are:

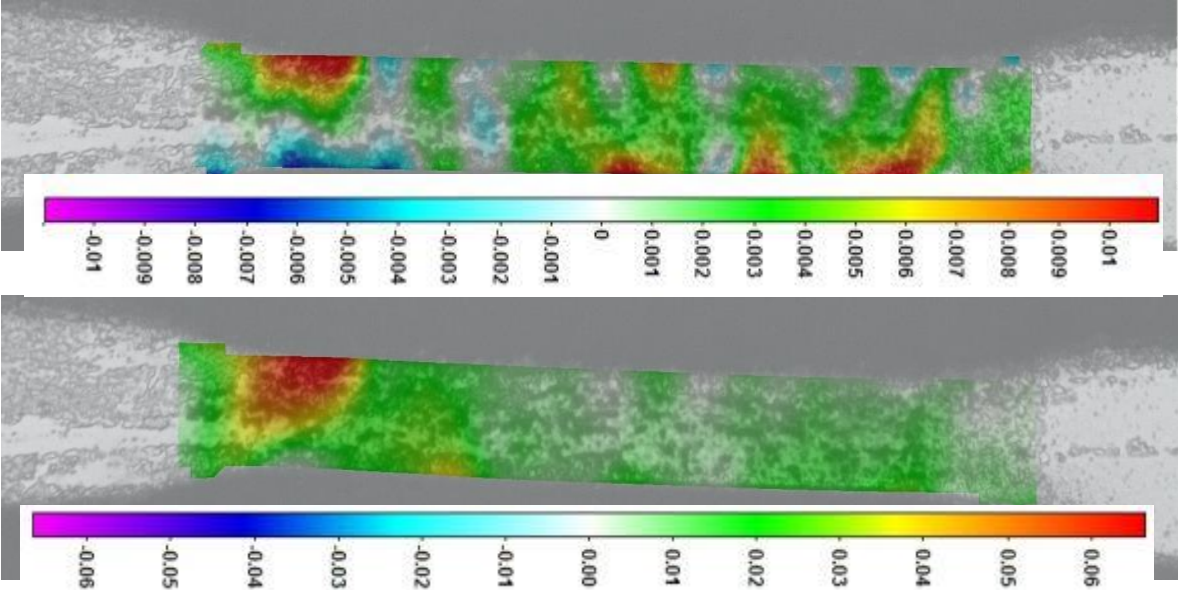
- Gauge length = 100 μm
- Gauge width = 33 μm
- Gauge thickness = 25 μm





From Fig 6.4 to Fig 6.10 – Summary of tensile test. Horizontal axis = Tensile axis. Top view of the sample

The previous pictures follow the reference of the crystal in Fig. 6.3.



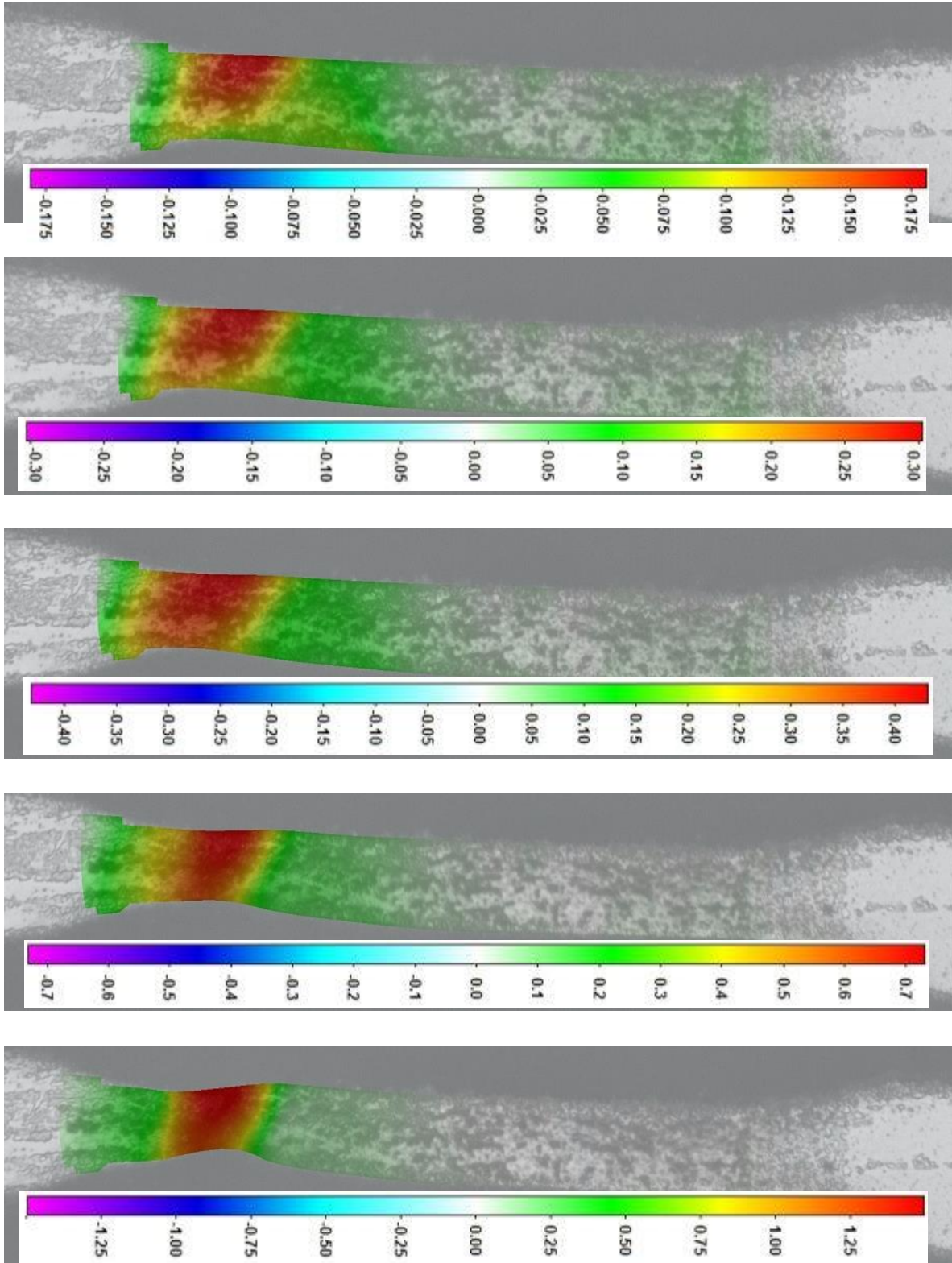


Fig 6.11 to Fig 6.17 – Longitudinal strain maps which refer to the previous seven pictures

Obviously, the fractured area has been selected in the DIC software to average the longitudinal and transverse values of strain. From the analysis, engineering stress – longitudinal strain and true stress – longitudinal strain curves are obtained. Those are compared in Fig 6.18.

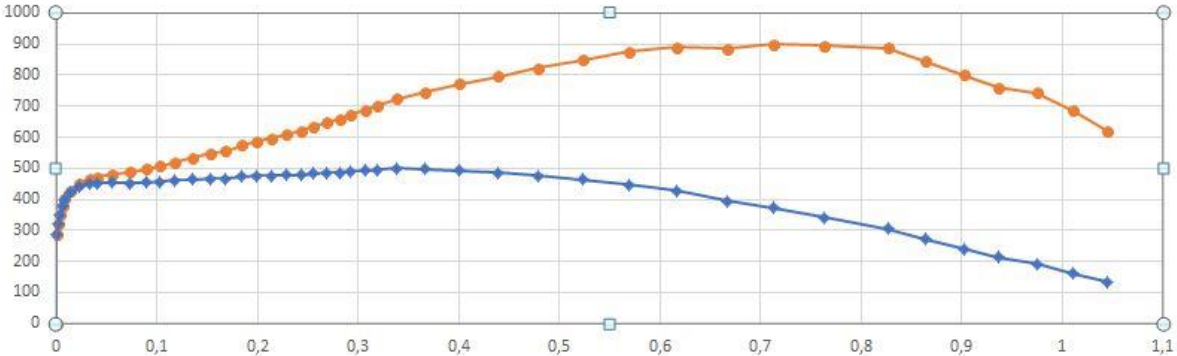


Fig 6.18 – Engineering stress – longitudinal strain in blue. True stress – longitudinal strain in orange. Stress in MPa, strain unit less.

From Fig 6.18, the yield strength and the ultimate tensile strength (referred to the orange curve) are respectively equal to ~290 MPa and ~900 MPa.

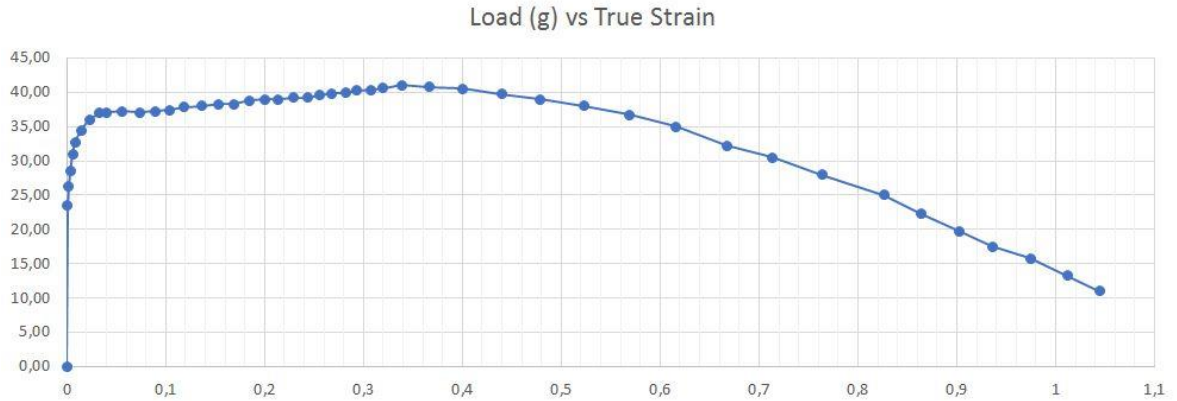


Fig 6.19 – Load [g] vs Longitudinal Strain

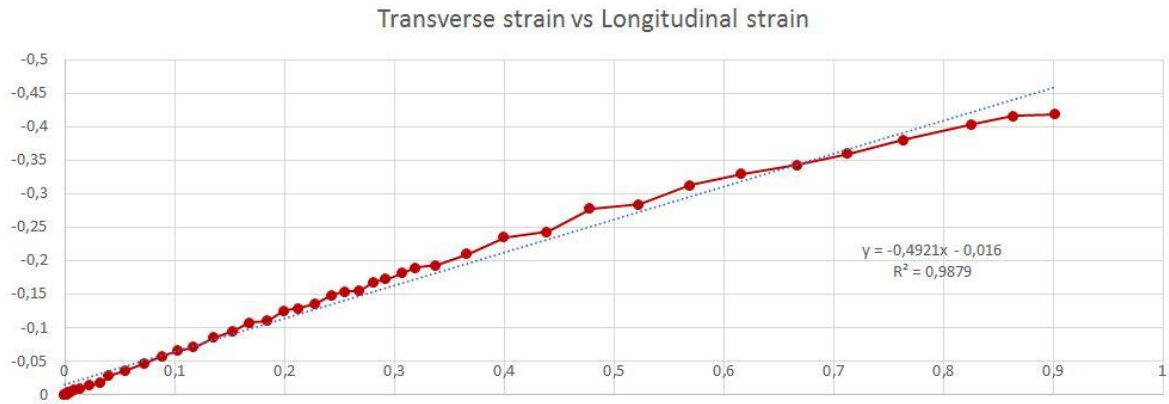


Fig 6.20 – Transverse strain vs Longitudinal strain

6.2 Gauge containing a single grain boundary separating two single crystals (Configuration 2 Fig. 4.10)

6.2.1 Sample “A3”

The EBSD map regarding this specimen can be seen in Fig. 6.19.

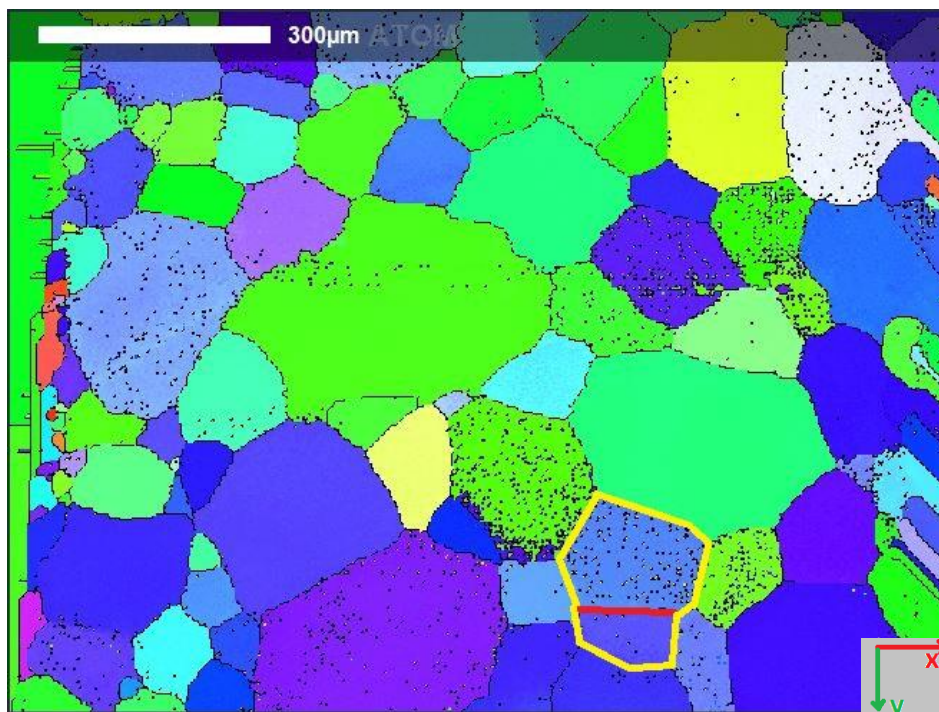


Fig 6.21 – EBSD map sample “A3”

Basically, sample “A3” contains in its gauge two single crystals (underlined in yellow in Fig 6.21) divided by a grain boundary (marked in red in Fig 6.21). The “blue” crystal (the higher up) will fill the left part of the gauge length in the next pictures, while the “violet” one will be on the right part.

“Blue” crystal Euler angles are:

- $\Phi = 137.83^\circ$
- $\Theta = 107.21^\circ$
- $\Psi = 49.57^\circ$

“Violet” crystal Euler angles are:

- $\Phi = 144.69^\circ$
- $\Theta = 108.39^\circ$
- $\Psi = 5.93^\circ$

The grain boundary misorientation is equal to 17.5° .

Sample “A3” in its un-deformed configuration is visible in Fig. 6.22.

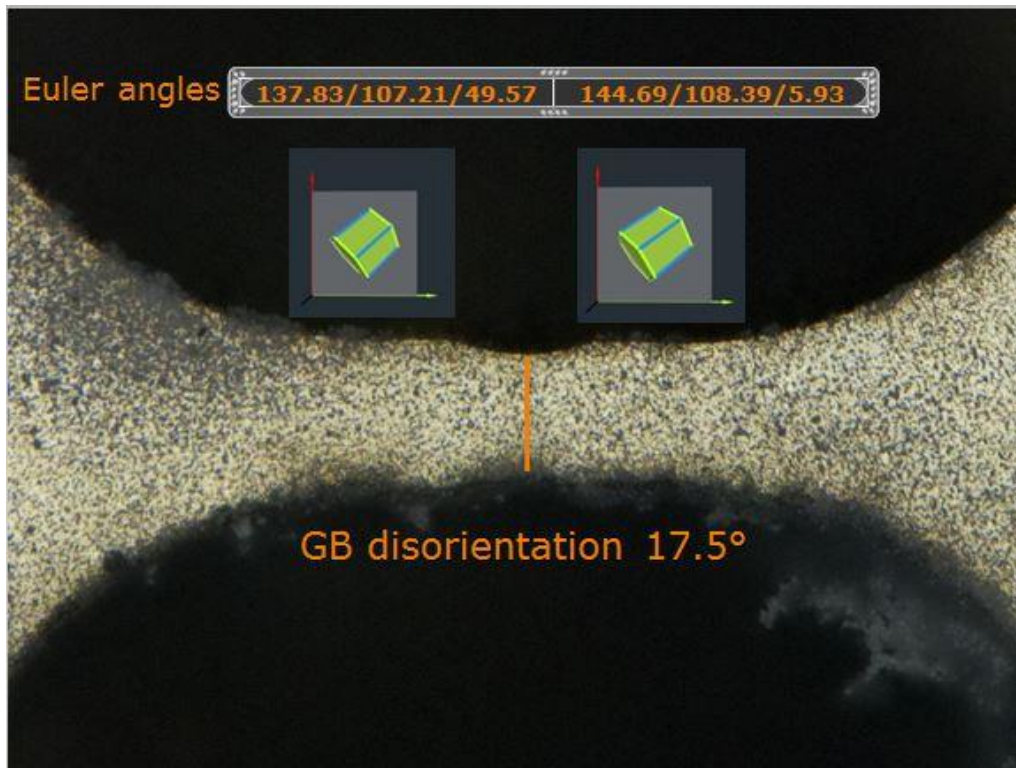
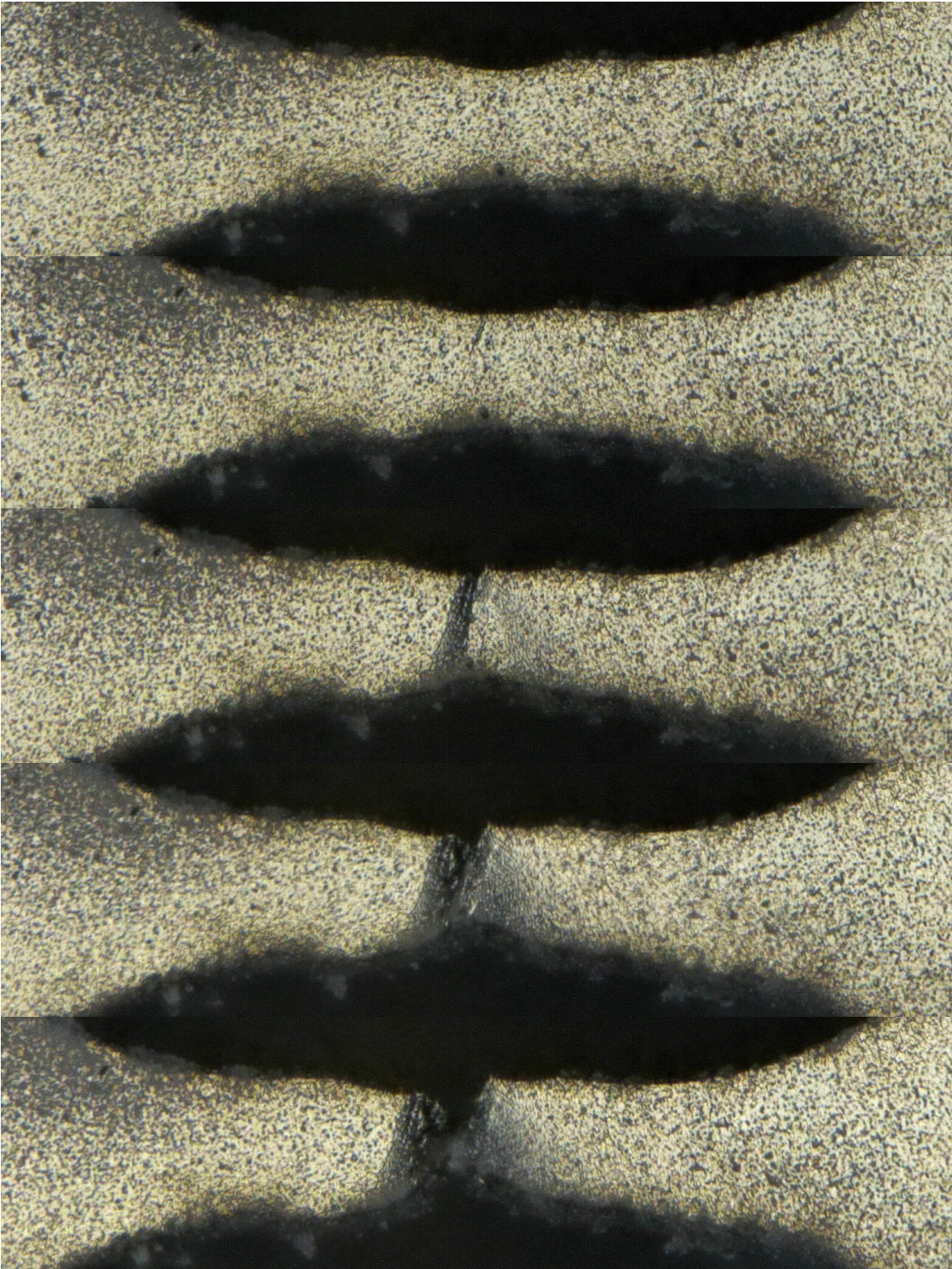


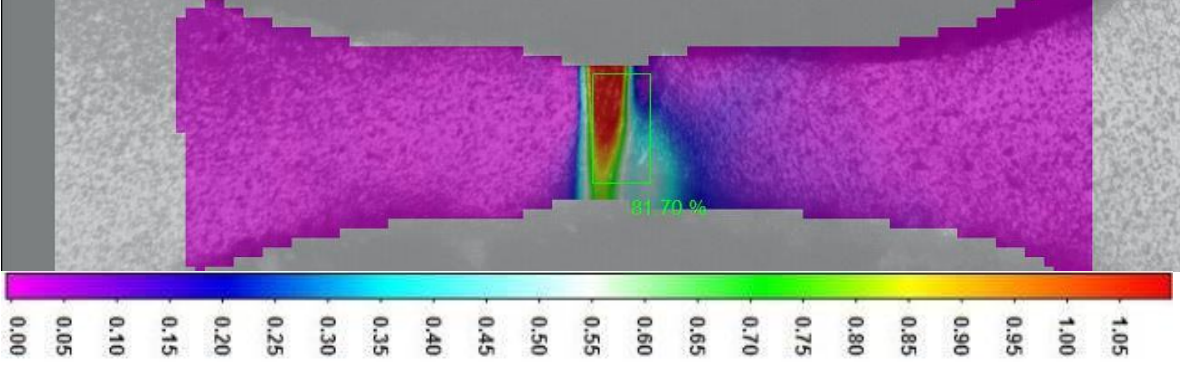
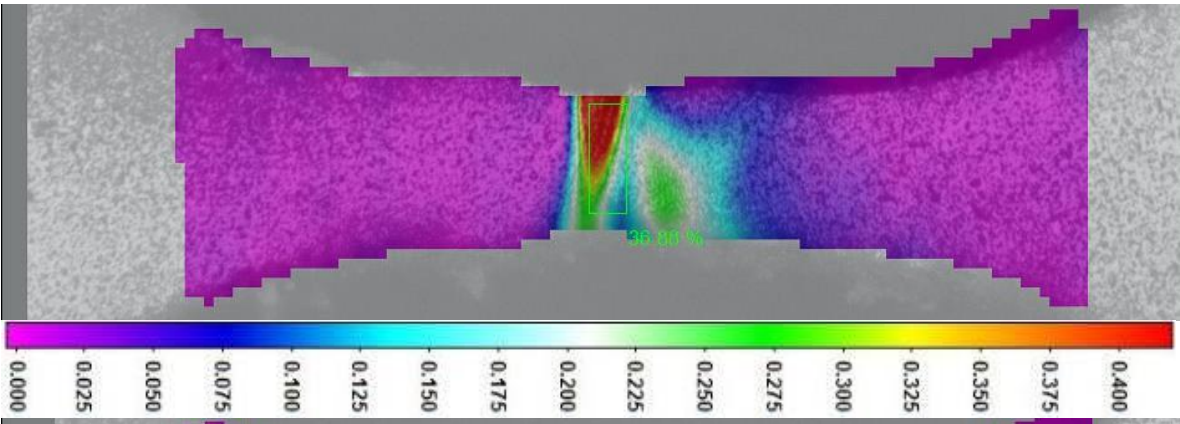
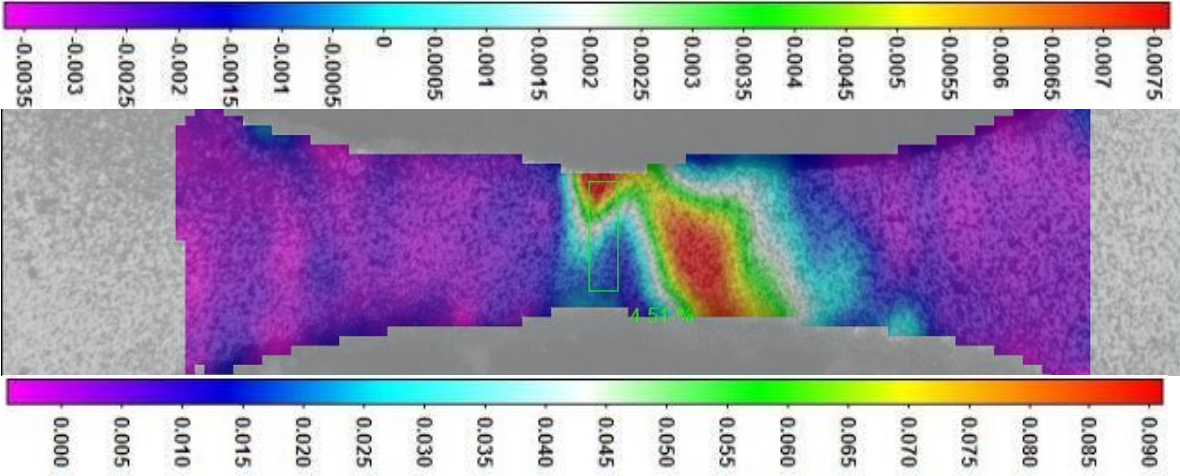
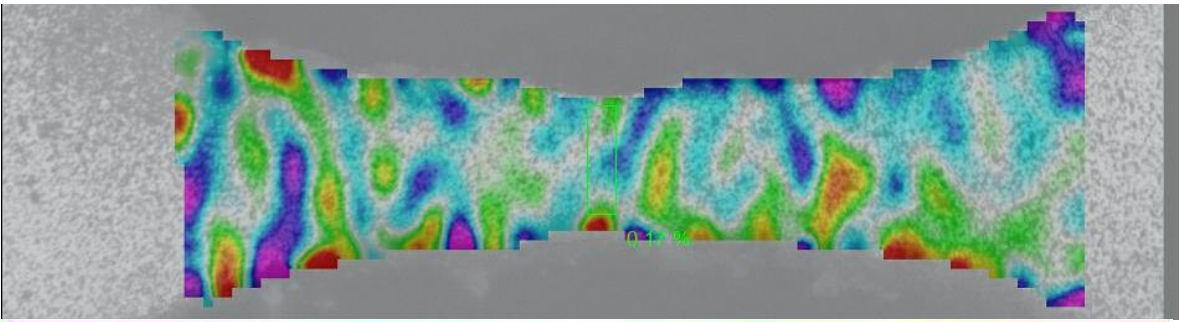
Fig 6.22 – Un-deformed configuration sample “A3”

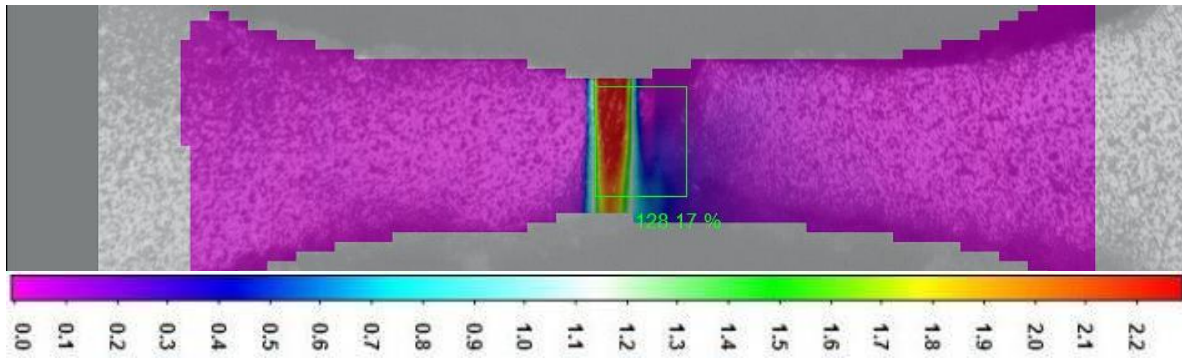
After laser micromachining, the dimensions of the gauge are:

- Gauge length = 100 μm
- Gauge width where the grain boundary stands = 42 μm
- Gauge width where the grains are analyzed = 46 μm
- Gauge thickness = 27 μm



From Fig 6.23 to Fig 6.27 – Summary of Sample “A3” tensile test. Same reference as Fig. 6.22.





From Fig 6.28 to Fig 6.32 - Longitudinal strain maps which refer to the previous five pictures

As it can be seen from the previous pictures, the longitudinal deformation is mostly on the boundary that is also the locus where the fracture occurs. Looking at Fig. 6.33 and Fig. 6.34, the left grain seems to be the strongest although it presents the lower yield strength (~ 270 MPa) ; furthermore, it only deforms until the 0.8%. This obviously leads to a “short” stress strain curve that stops at the beginning of the plastic deformation. The right grain, instead shows yield strength equal to ~ 290 MPa and deforms more than 10%.

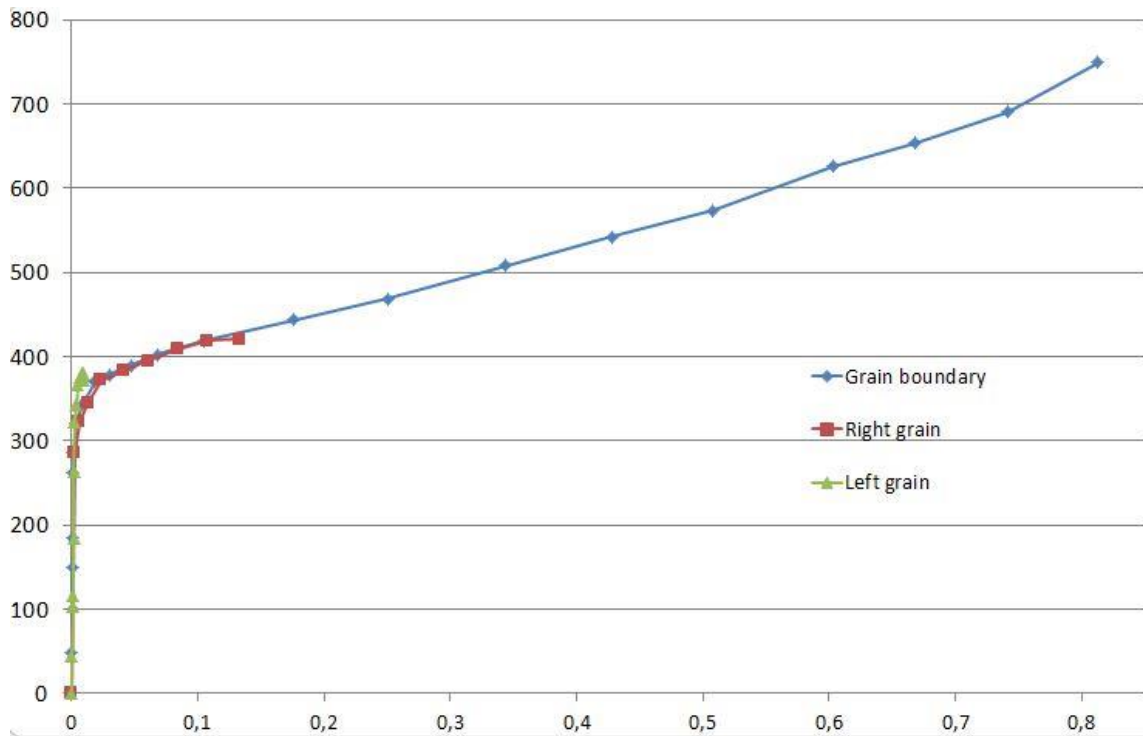


Fig 6.33 – True Stress [MPa] vs Longitudinal strain for grain boundary, left grain and right grain

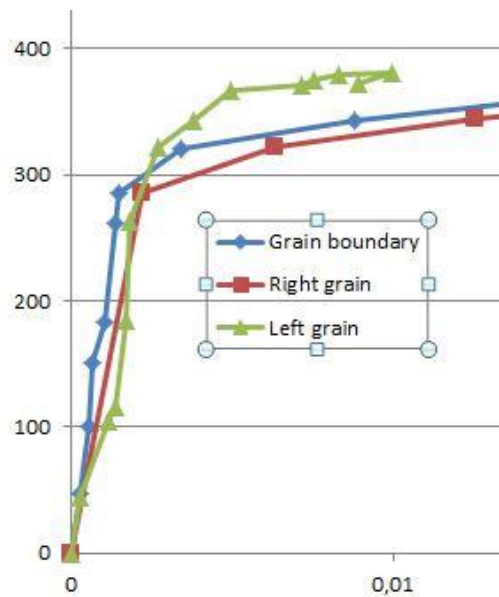


Fig 6.34 – Zoom on True Stress [MPa] vs Longitudinal strain for grain boundary, left grain and right grain

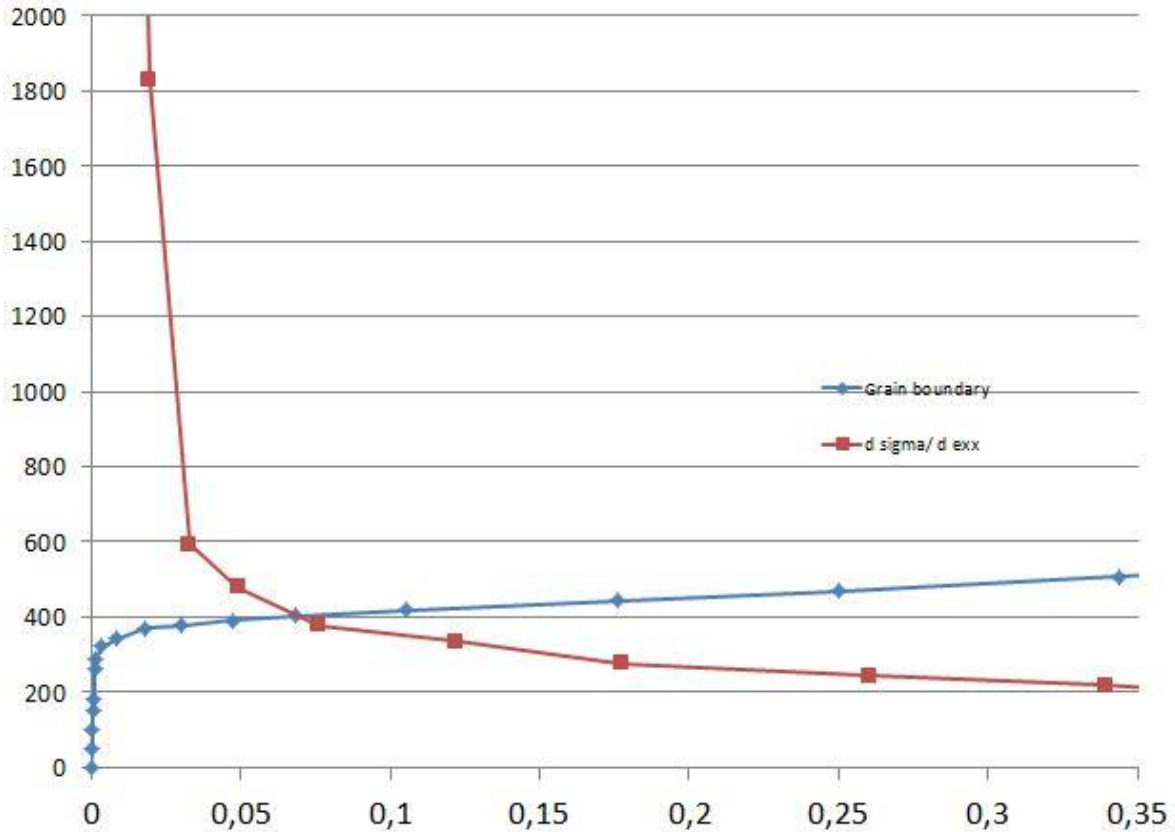


Fig 6.35 - $\frac{d\sigma}{d\epsilon_{long}}$ – longitudinal strain (red) and true stress – longitudinal strain (blue) curves regarding the grain boundary.

The intersection between the two curves in Fig 6.35 provides the onset of necking. From that value of longitudinal strain ($\sim 7\%$), the load starts decreasing while the cross sectional area keeps on decreasing. This means that the increase of the true stress – longitudinal strain curve is only due to the fact that the cross sectional area decreases faster than the load. In the engineering stress – longitudinal strain curve, the ultimate tensile strength would correspond to that value of longitudinal strain ($\sim 7\%$), as can be seen from Fig 6.36. The UTS value is equal to approximately 415 MPa.

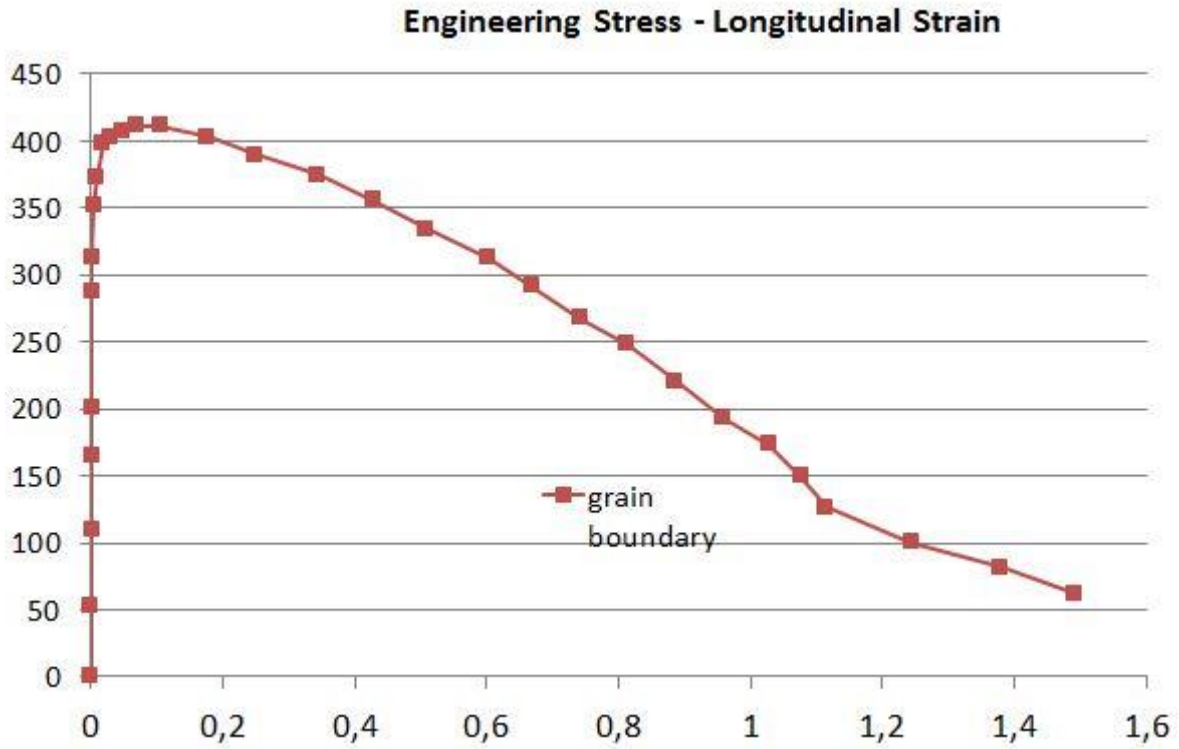


Fig 6.36 – Engineering Stress [MPa] – Longitudinal Strain for grain boundary

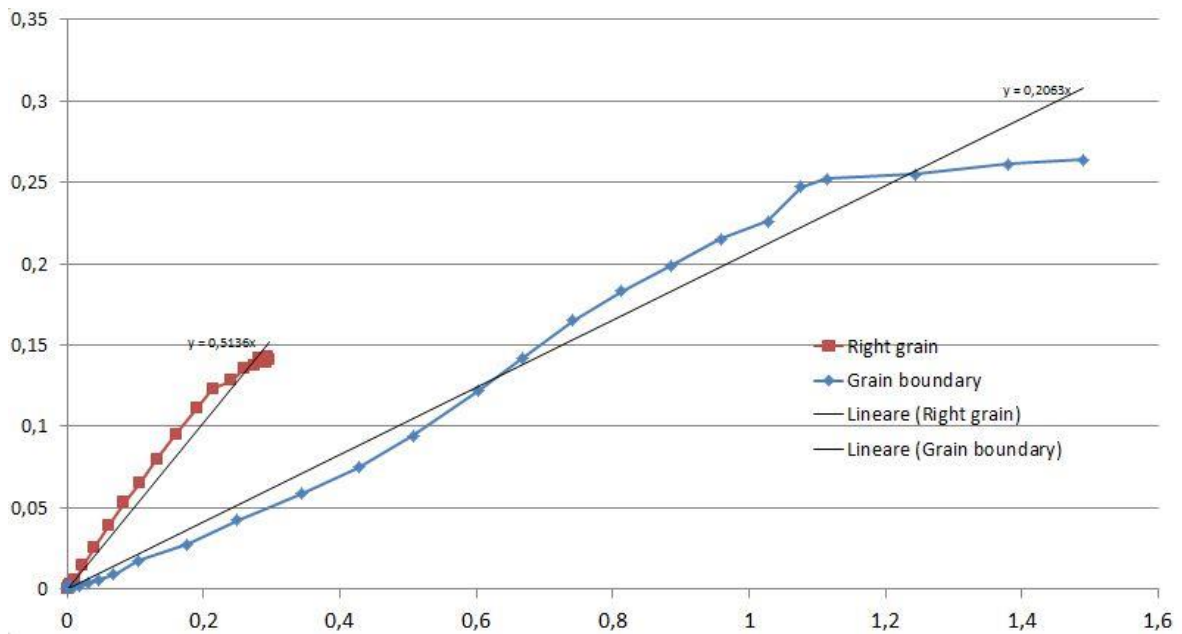


Fig 6.37 - Transverse strain (absolute value) vs Longitudinal strain

6.2.2 Sample “A6”

The EBSD map regarding sample “A6” can be seen in Fig. 6.38.

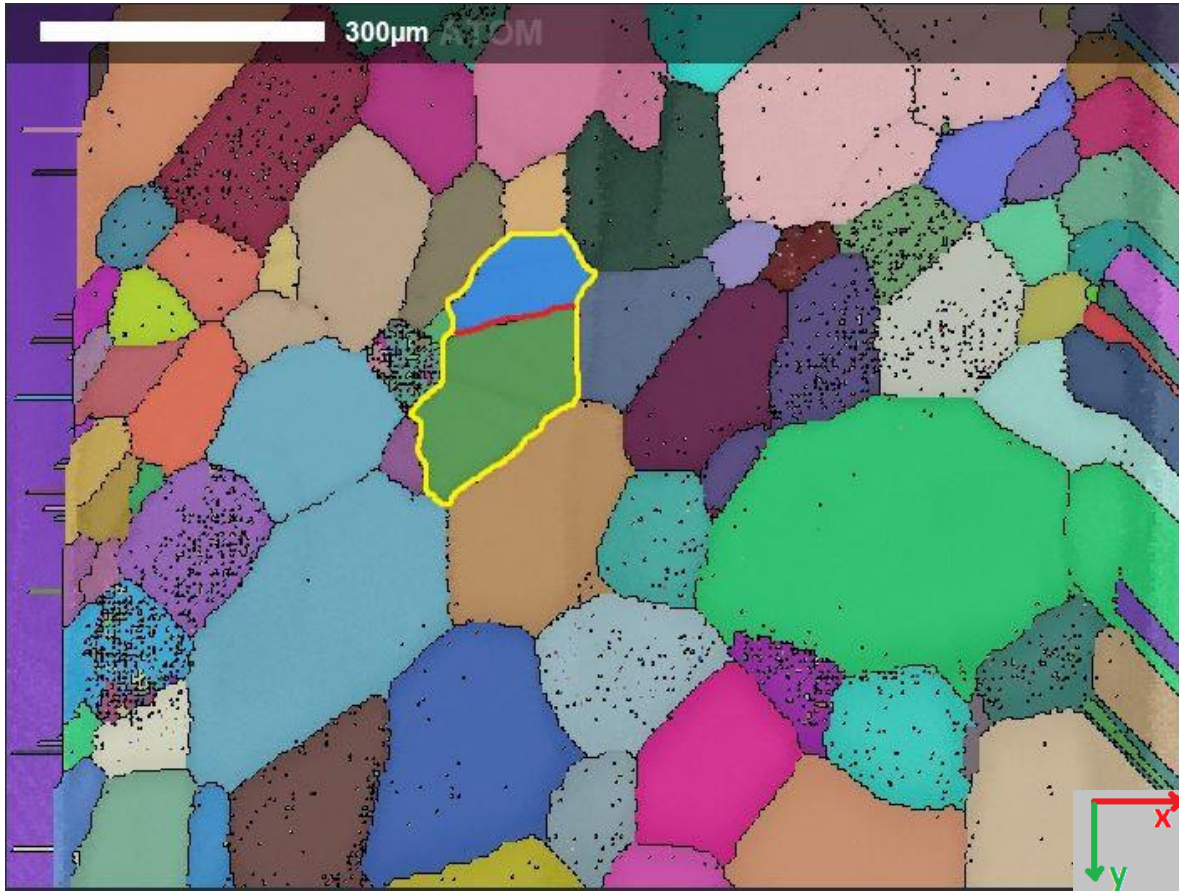


Fig 6.39 – EBSD map for sample “A6”

Even in this case the two crystals marked in yellow (Fig. 6.39) are the ones contained in the gauge of the sample. The red line (Fig. 6.39), indicates the grain boundary. The “green” crystal will be on the left side in the next pictures while the “light blue” one will be on the right.

“Green” crystal Euler angles are:

- $\Phi = 151.1^\circ$
- $\Theta = 104.96^\circ$

- $\Psi = 53.34^\circ$

“Light blue” crystal Euler angles are:

- $\Phi = 38.72^\circ$
- $\Theta = 71.54^\circ$
- $\Psi = 2.75^\circ$

The grain boundary misorientation is equal to 66° .

In Fig. 6.40, it is possible to see the gauge of sample “A6” before the beginning of the test.

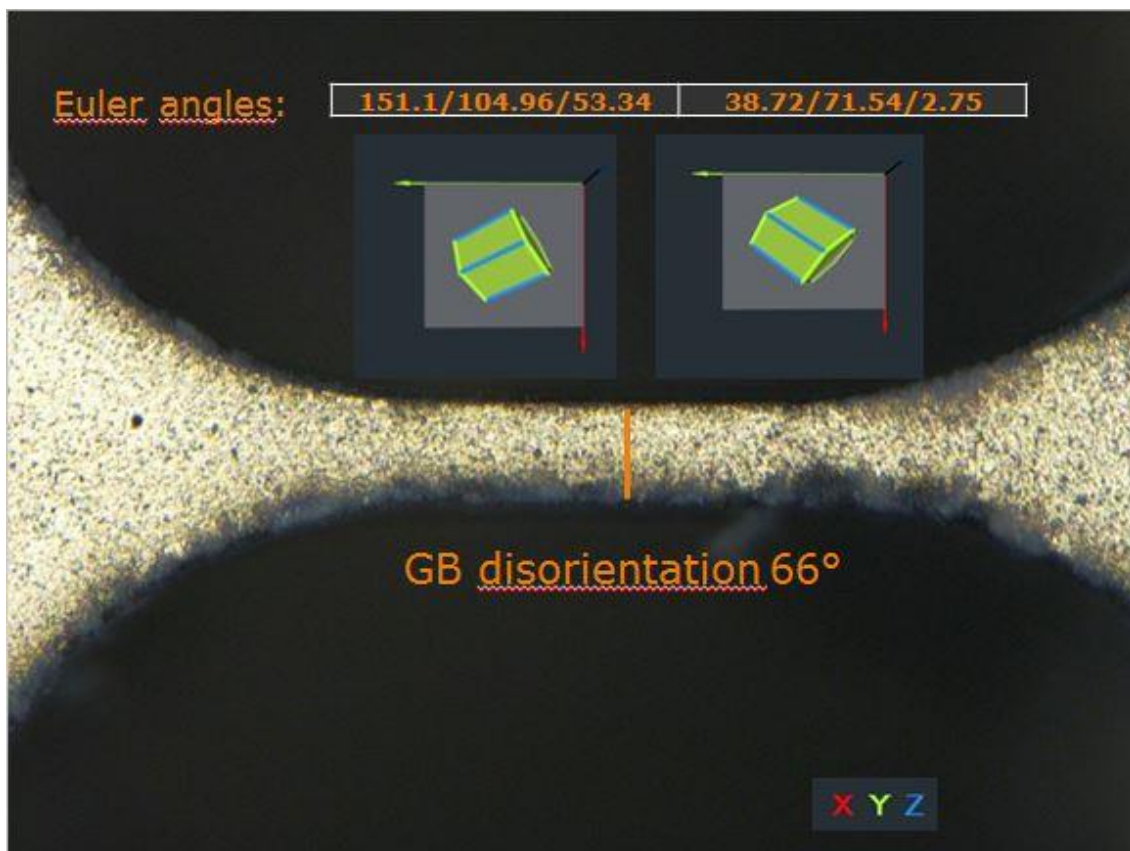
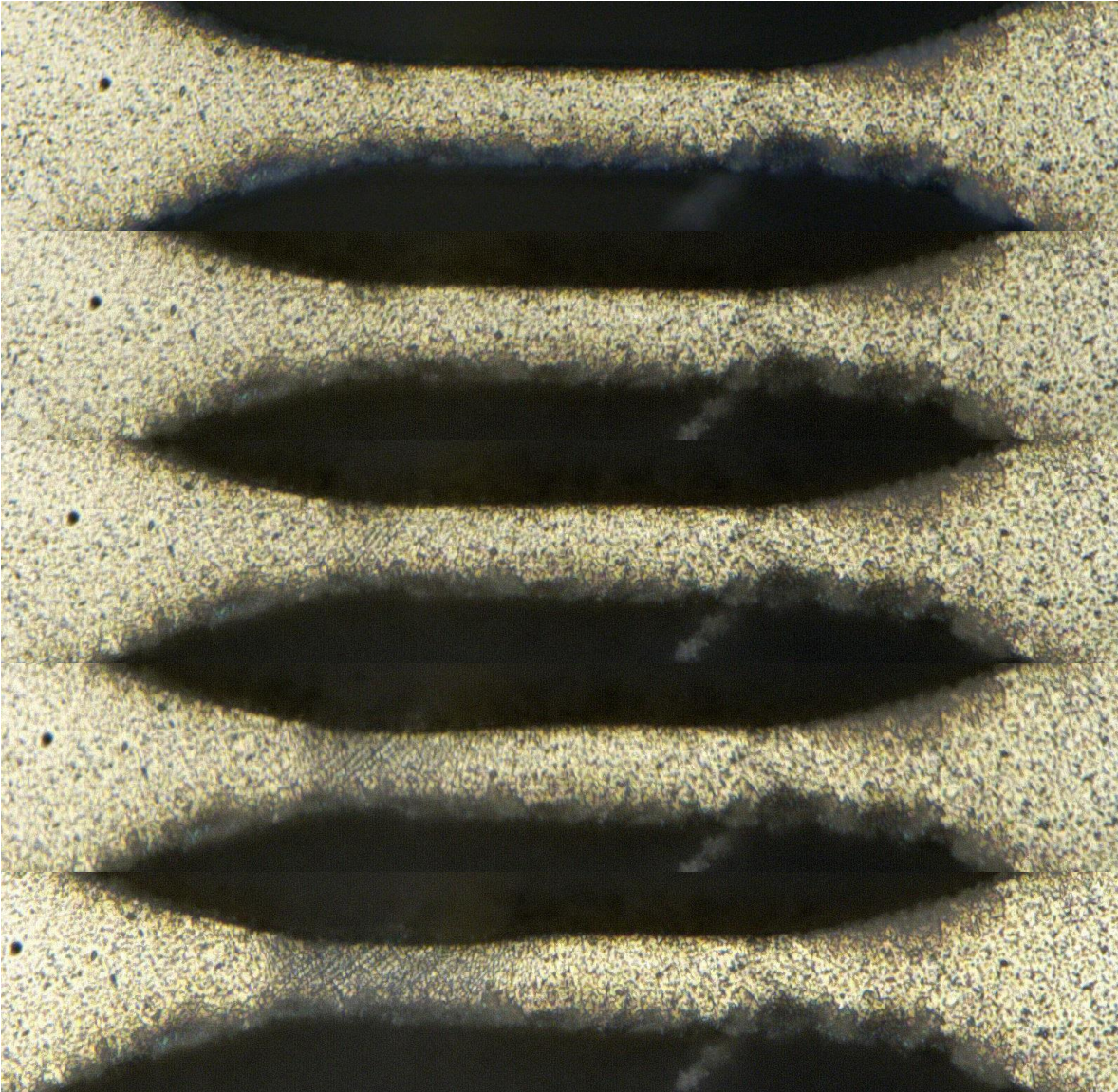
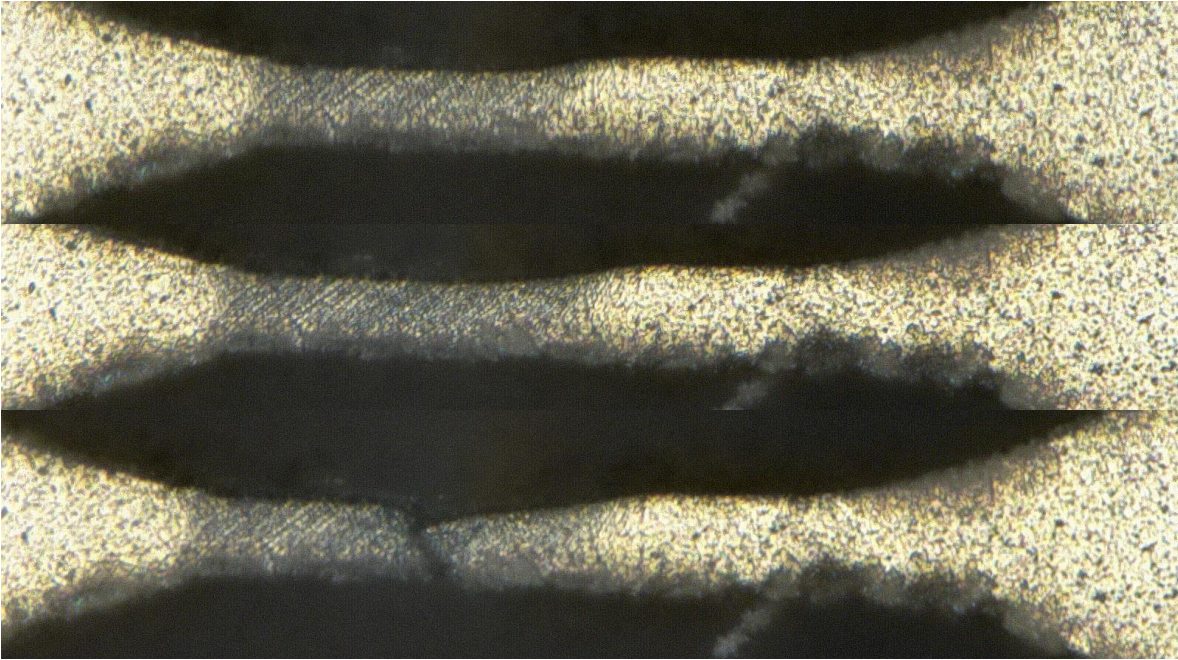


Fig 6.40 – Un-deformed configuration sample “A6”

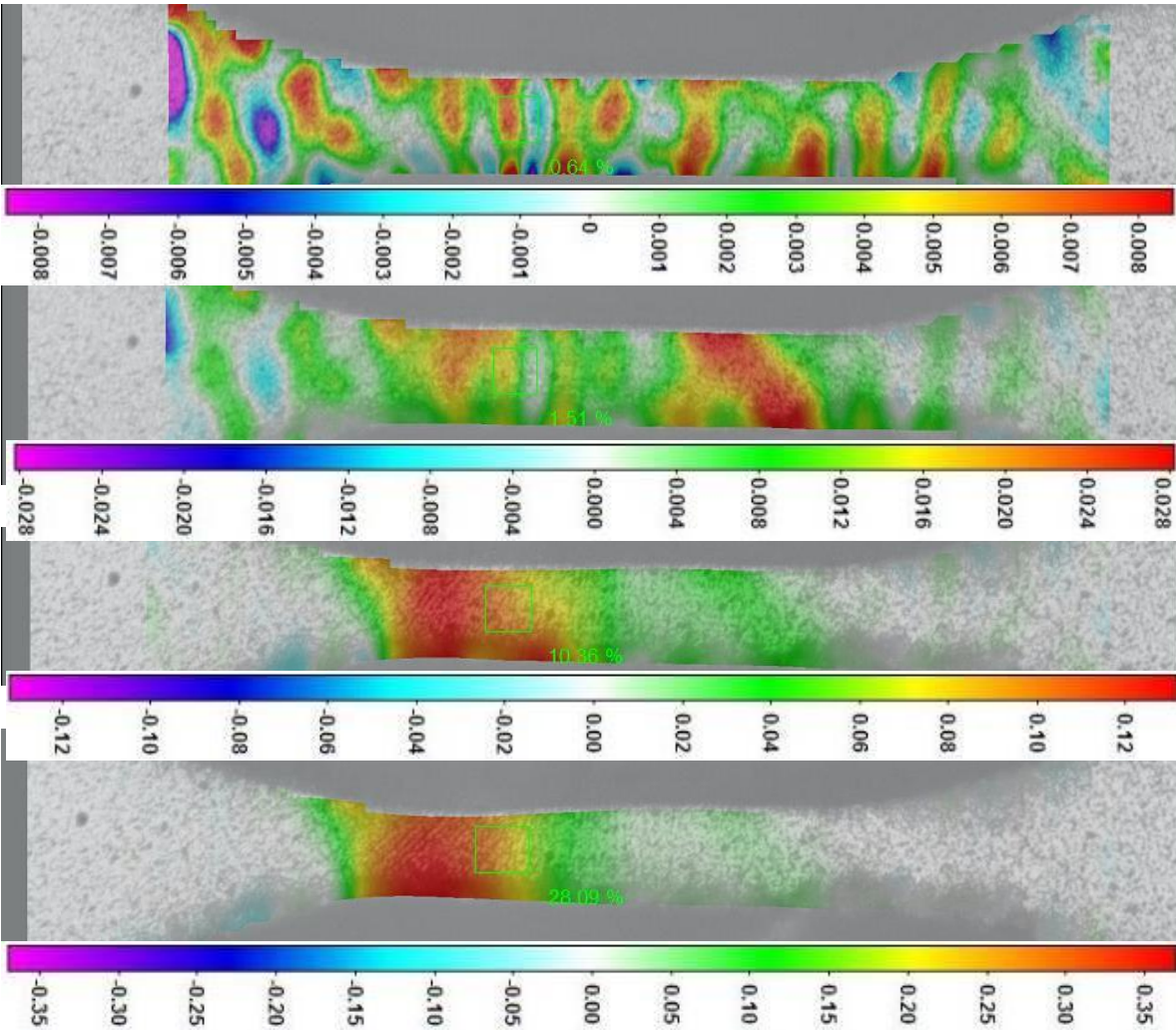
The gauge dimensions are:

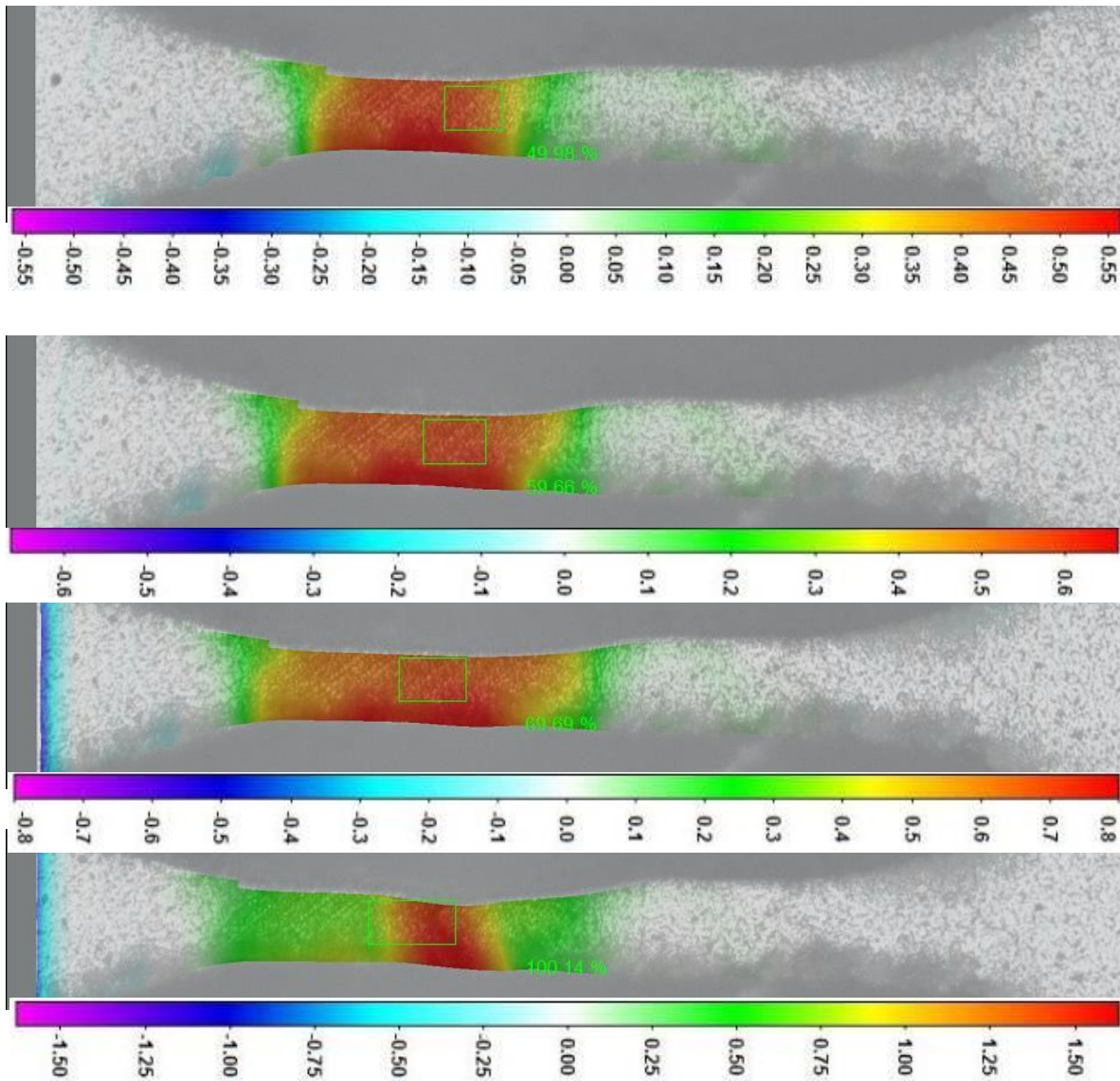
- Gauge length = 100 μm
- Gauge width = 31 μm
- Gauge thickness = 24 μm





From Fig 6.41 to Fig 6.48 – Summary of tensile test for sample “A6”. Same reference as Fig. 6.40.





From Fig 6.49 to Fig 6.56 - Longitudinal strain maps which refer to the previous eight pictures

The previous pictures show the left grain to exhibit higher yield strength (Fig 6.50) as, with equal load, it deforms less than the right grain, but also to manifest lower tensile strength as it presents long deformation until fracture. Right grain, on the other hand, only deforms until 2.5%. Taking a look at Fig 6.58, it emerges that left grain yield strength is ~ 295 MPa and right grain yield strength is ~ 270 MPa. The grain boundary behaves really similarly to

the right grain, in fact it deforms until longitudinal strain is equal to 2.5%. Moreover, Fig 6.59 shows that left grain presents a really short period of plastic deformation after the yield strength and long necking.

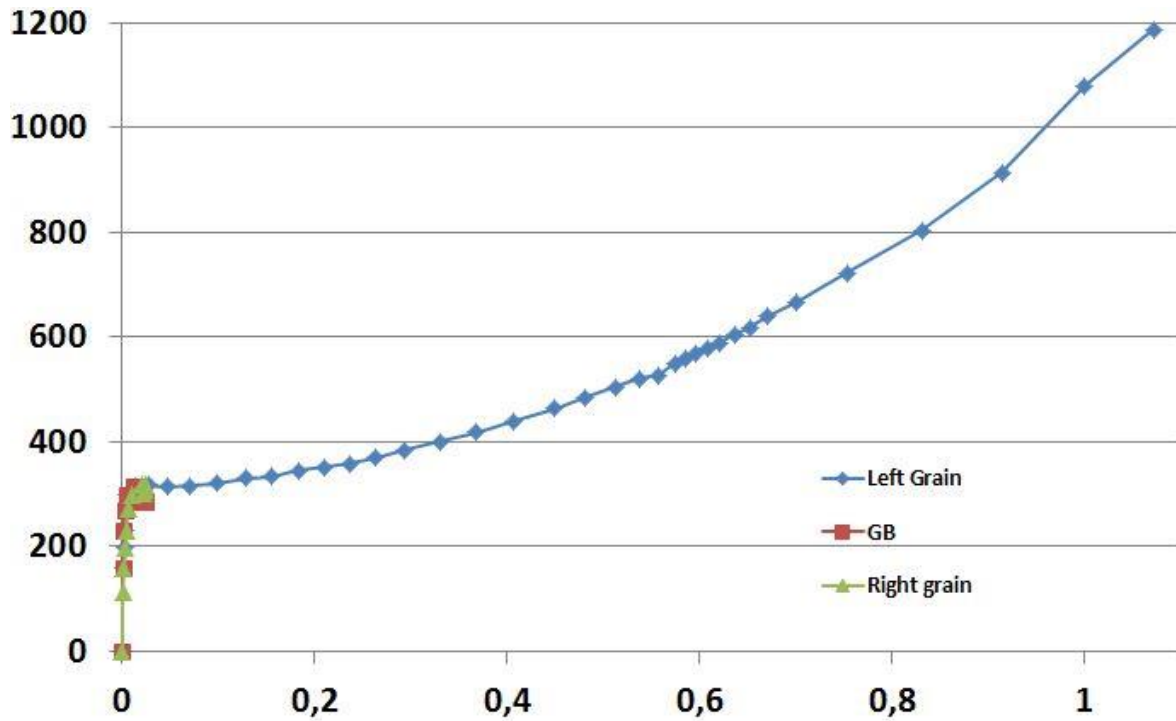


Fig 6.57 – True stress [MPa] vs Longitudinal strain for left grain, right grain and grain boundary.

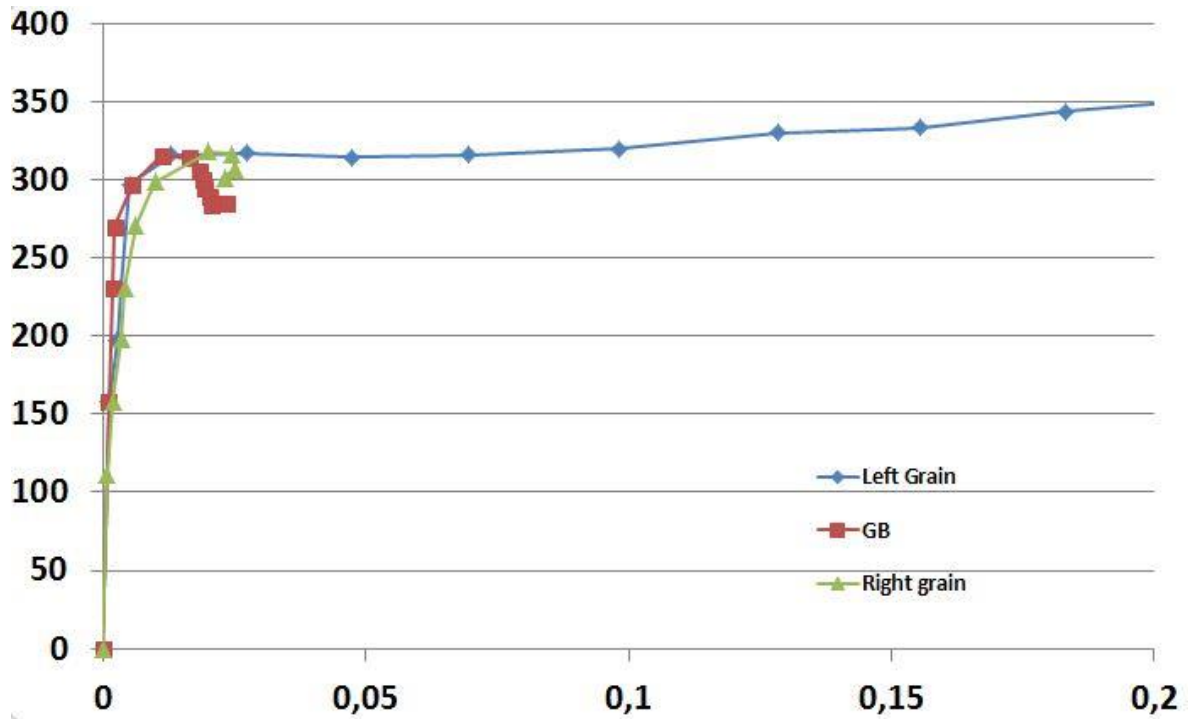


Fig 6.58 – Zoom on True stress [MPa] vs Longitudinal strain for left grain, right grain and grain boundary for yield strength analysis.

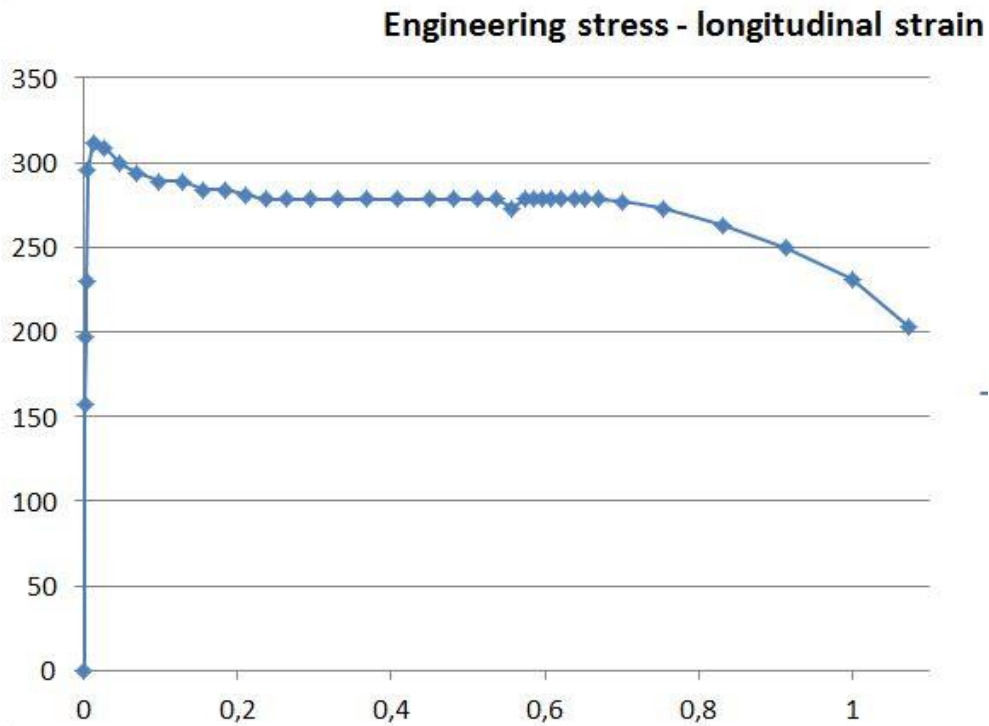


Fig 6.59 – Engineering stress [MPa] vs Longitudinal strain for left grain

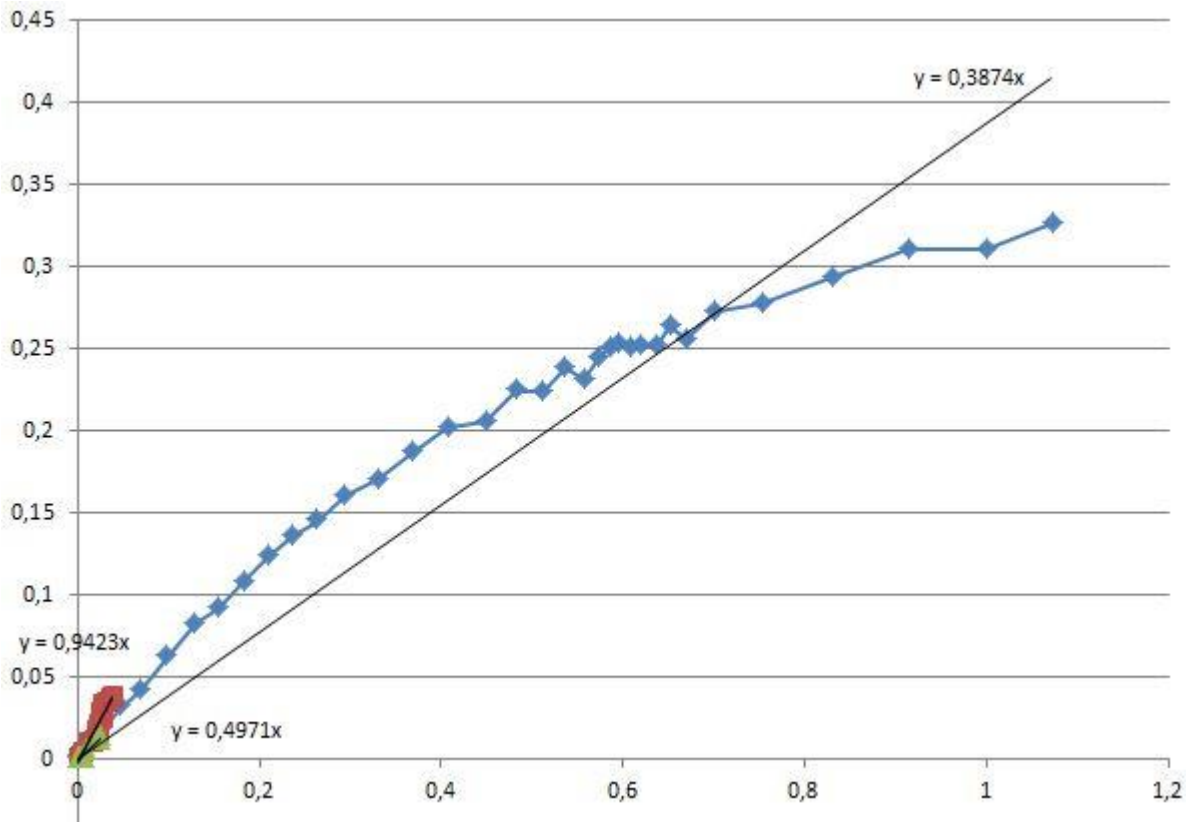


Fig 6.60 – Transverse strain (absolute value) vs Longitudinal strain for left grain (blue), right grain (green) and grain boundary (red).

6.2.3 Sample “A7”

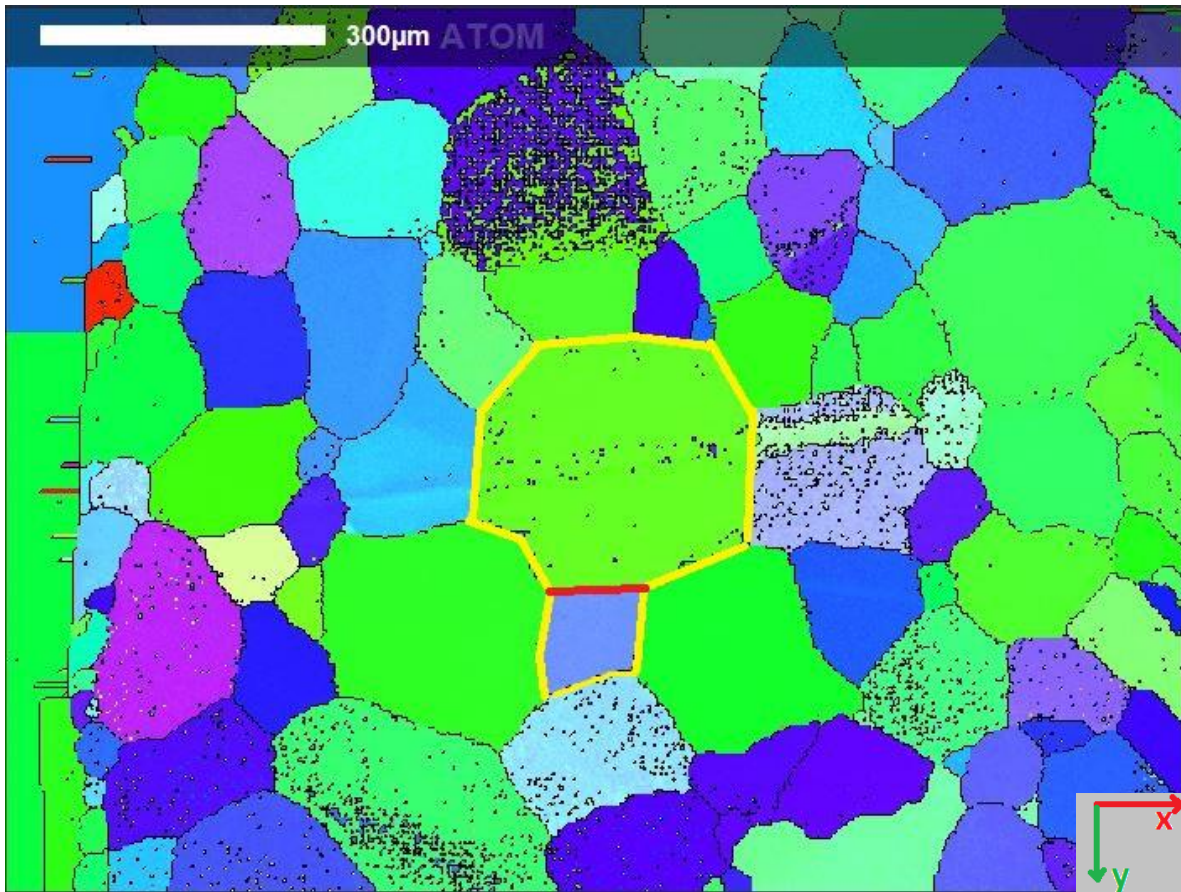


Fig. 6.61 – EBSD map for sample “A7”

This case presents once again the configuration “2” in Fig 4.10, in which the two crystals are marked in yellow and are the ones contained in the gauge of the sample (Fig. 6.61). The red line, indicates the analyzed grain boundary. The “green” crystal will be on the left side in the next pictures while the “light blue” one will be on the right.

“Green” crystal Euler angles are:

- $\Phi = 148.91^\circ$
- $\Theta = 115.78^\circ$
- $\Psi = 33.72^\circ$

“Light blue” crystal Euler angles are:

- $\Phi = 163.01^\circ$
- $\Theta = 111.32^\circ$
- $\Psi = 11.01^\circ$

The grain boundary misorientation is equal to 31° .

The un-deformed configuration of specimen “A7” is visible in Fig 6.62.

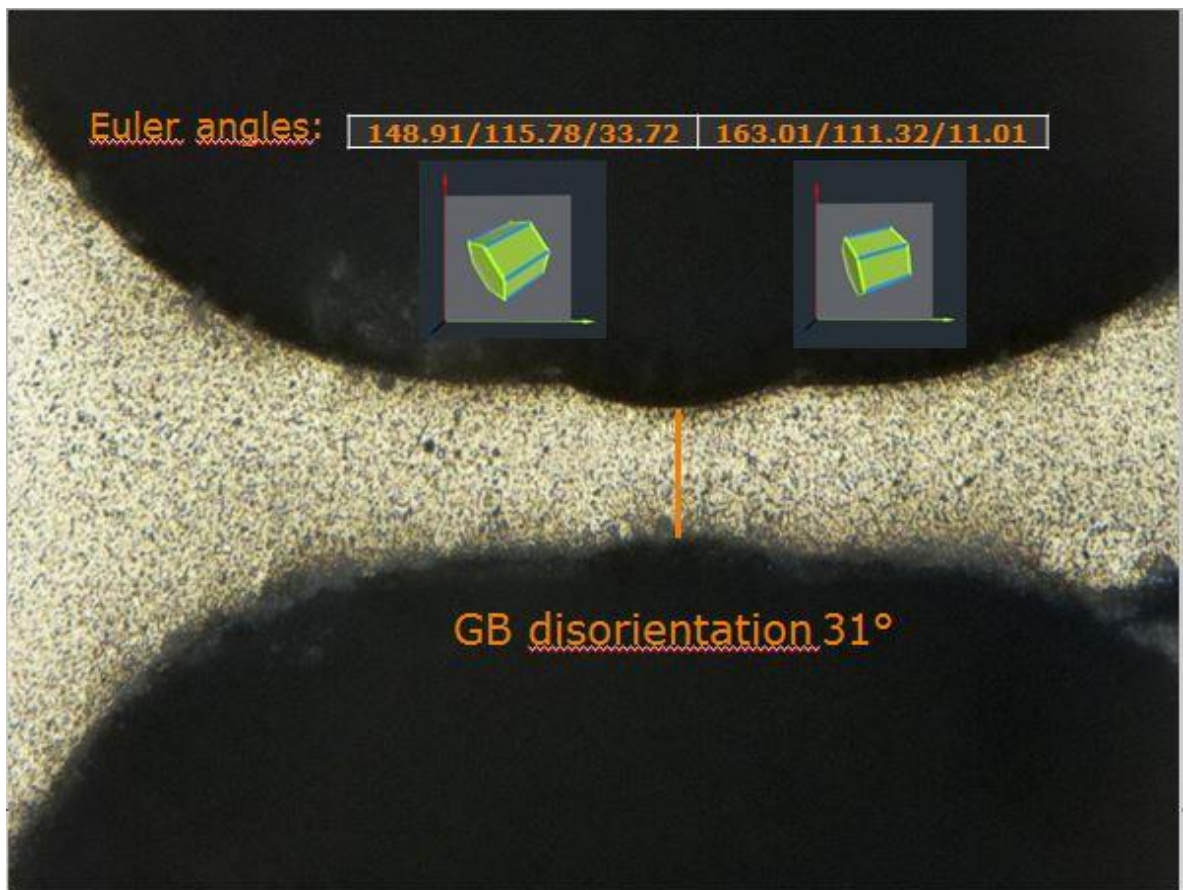
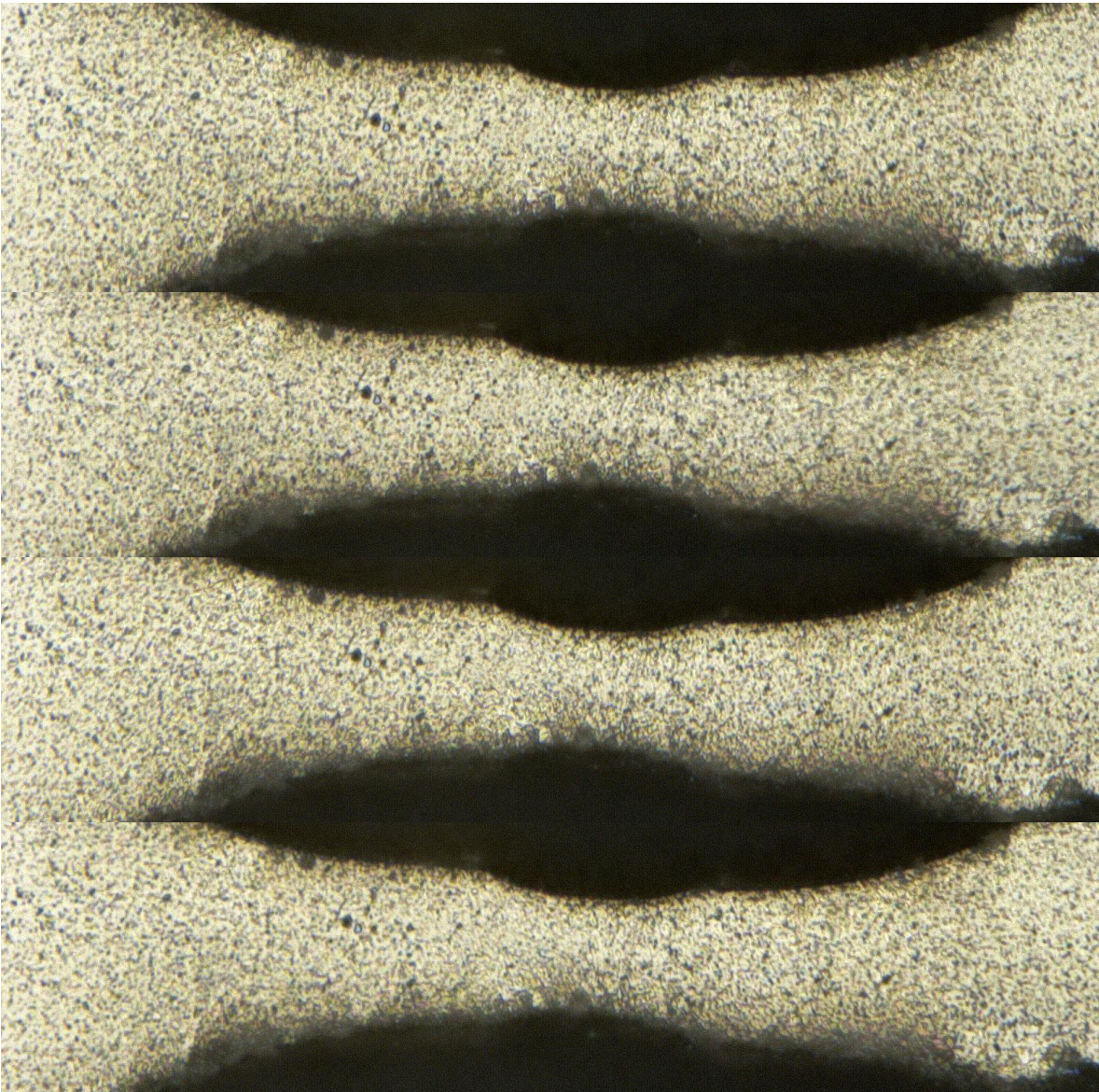


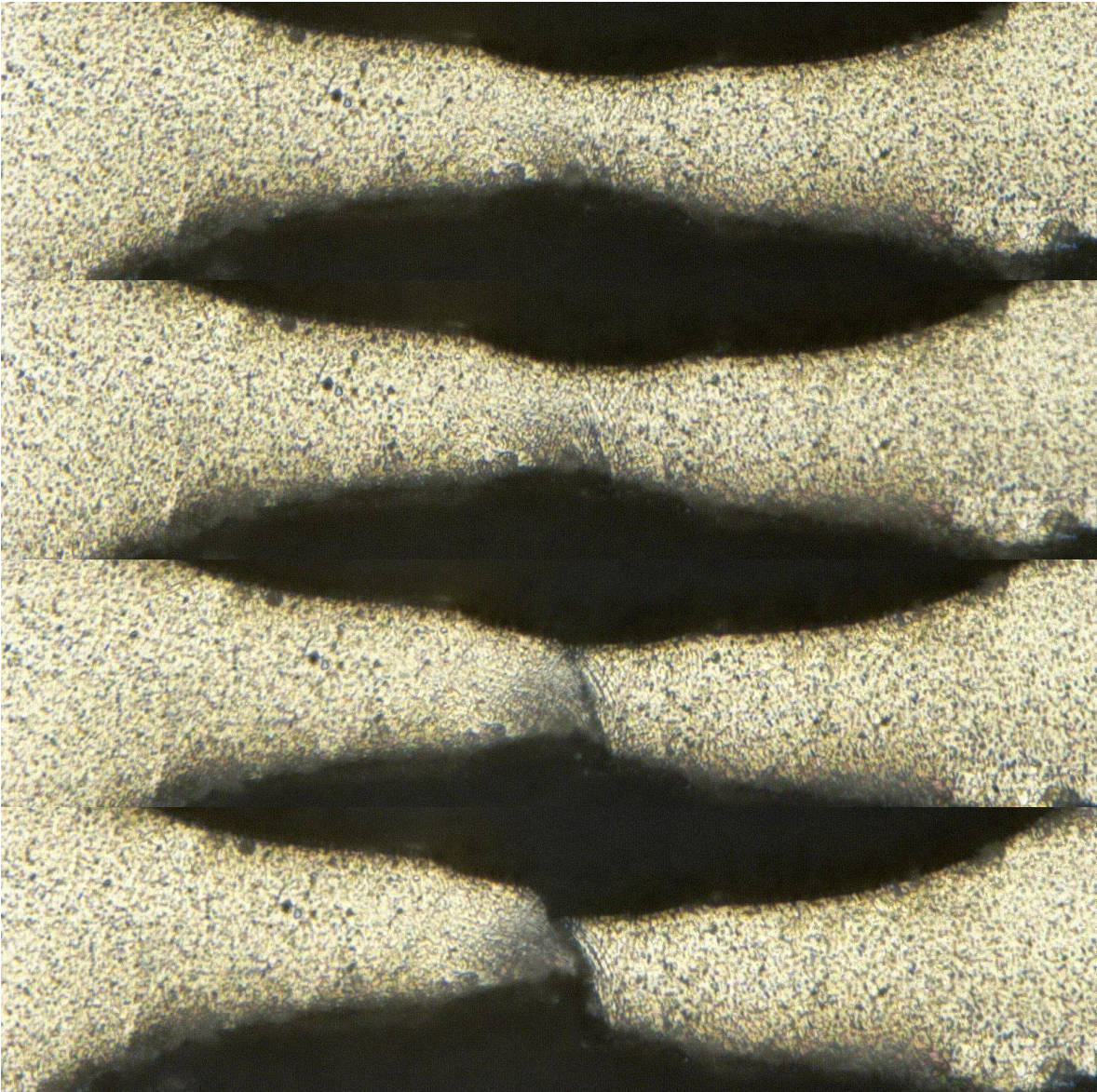
Fig 6.62 – Un-deformed configuration sample “A7”

After laser micromachining, the dimensions of the sample gauge are:

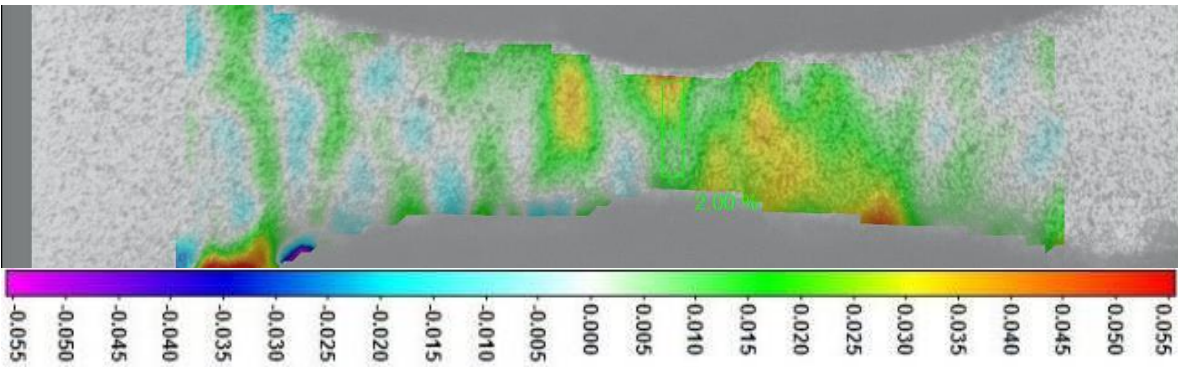
- Gauge length = $100\ \mu\text{m}$

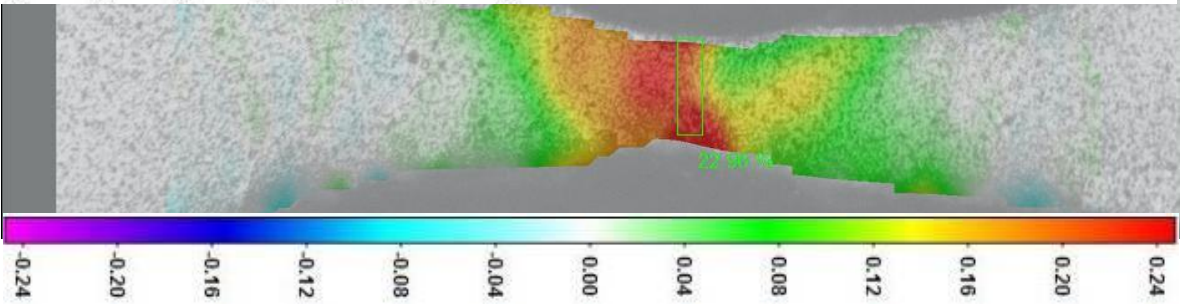
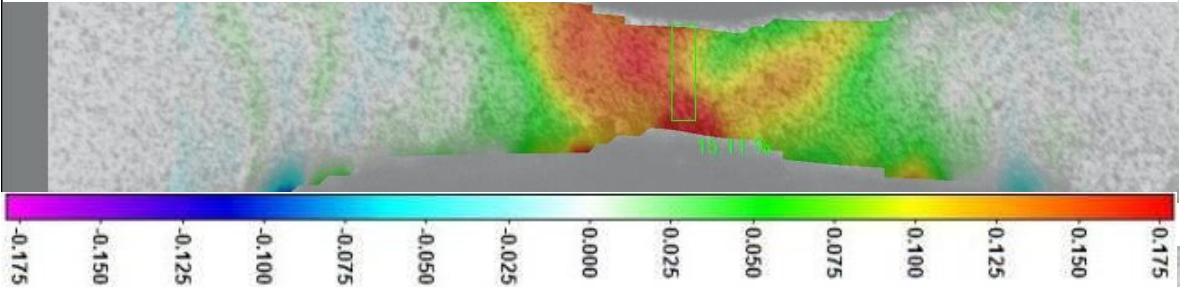
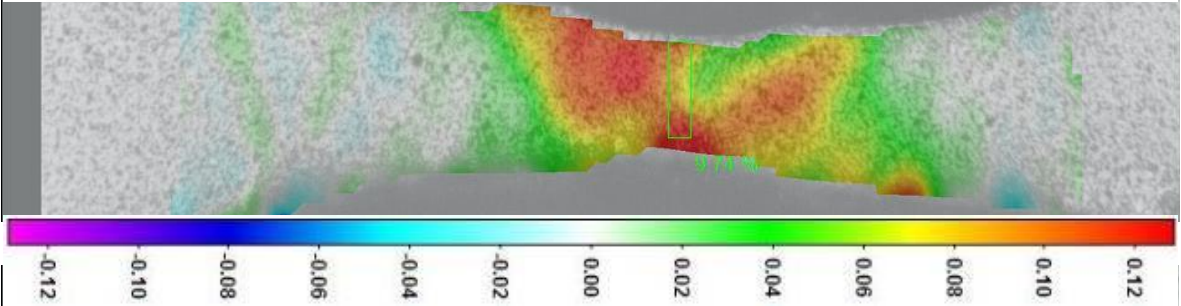
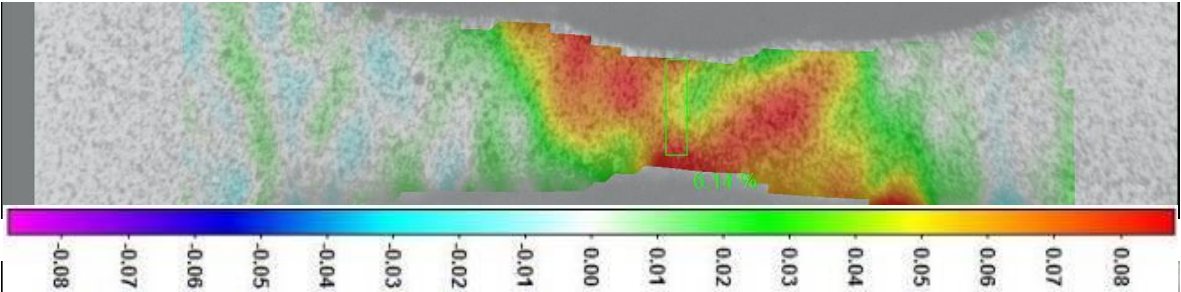
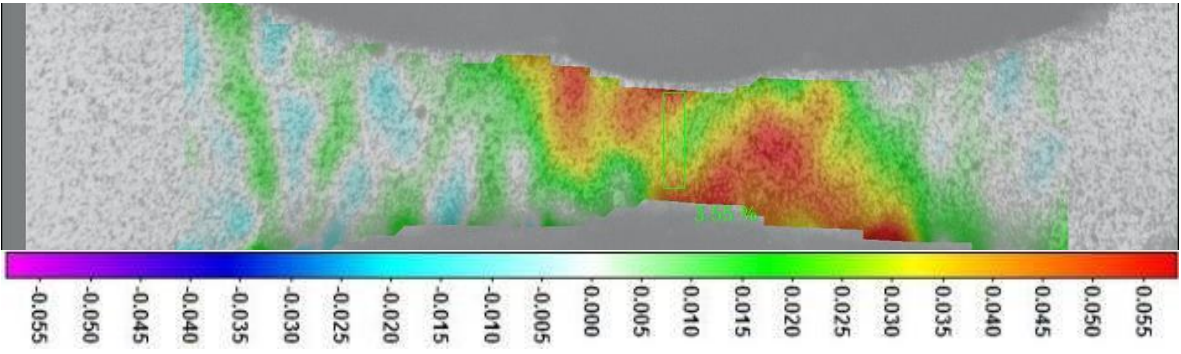
- Gauge width where the grain boundary stands = $39\ \mu\text{m}$
- Gauge width where the grains are analyzed = $42\ \mu\text{m}$
- Gauge thickness = $30\ \mu\text{m}$

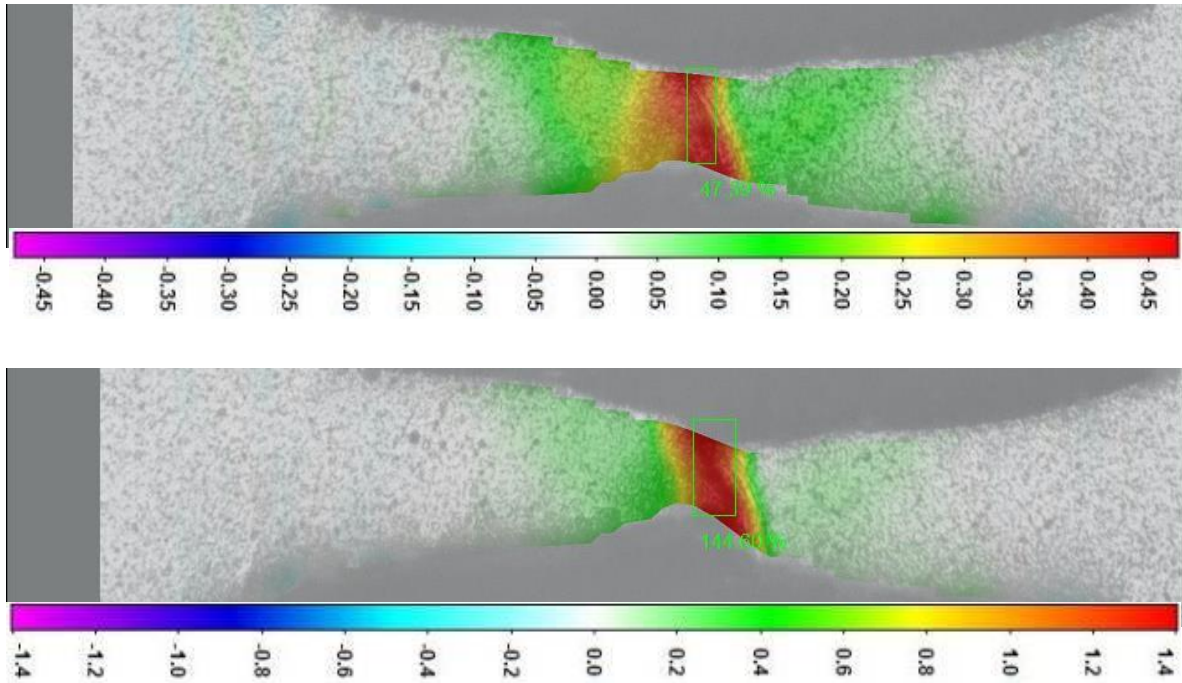




From Fig 6.63 To Fig 6.70 – Summary of tensile test for sample “A7”. Same reference as Fig. 6.62.







From Fig 6.71 to Fig 6.78 - Longitudinal strain maps which refer to the previous eight pictures

As it can be noticed from the previous pictures, the right grain shows higher yield strength but less tensile strength if compared to the left grain. In particular, by observing Fig 6.80, it can be seen that the left grain yield strength is equal to ~ 280 MPa and the right grain one is ~ 250 MPa. As already said, the right grain has more strength and its longitudinal strain reaches a value equal to $\sim 12\%$; the left grain, instead, deforms for more than $\sim 20\%$. After this value, the deformation localized onto the boundary which is the place where the fracture occurs.

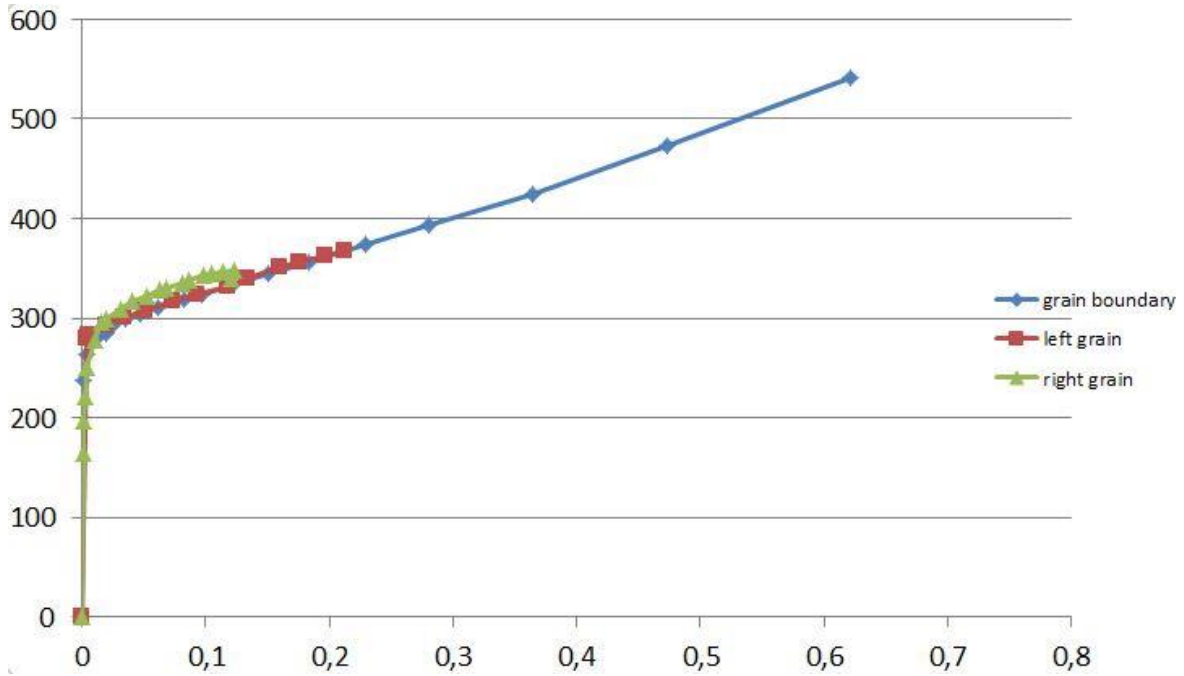


Fig 6.79 – True stress [MPa] vs Longitudinal strain for left grain, right grain and grain boundary

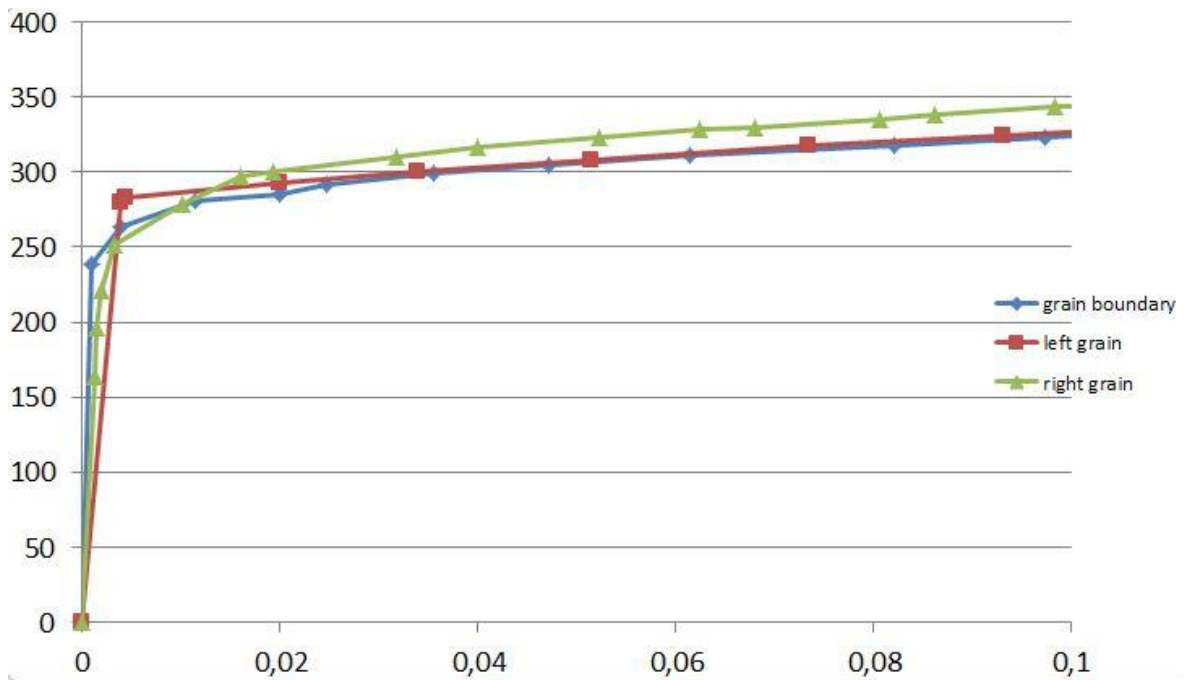


Fig 6.80 – Zoom on True stress [MPa] vs Longitudinal strain for left grain, right grain and grain boundary for yield strength analysis

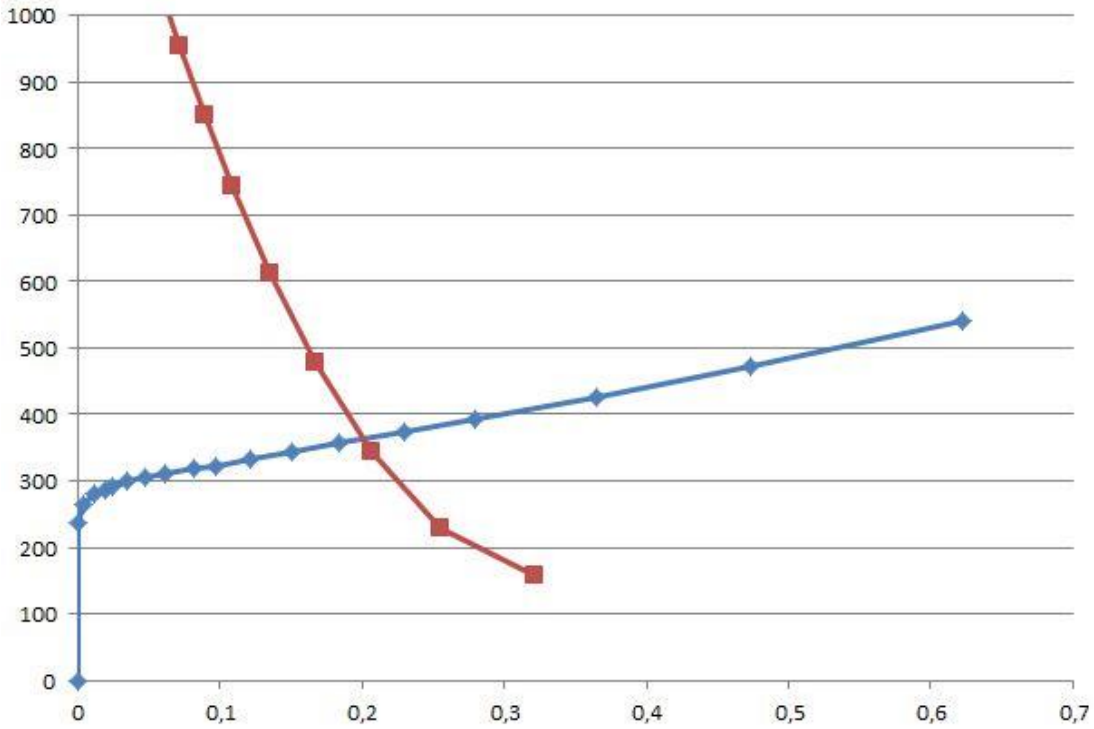


Fig 6.81 - $\frac{d\sigma}{d\varepsilon_{long}}$ – longitudinal strain (red) and true stress – longitudinal strain (blue) curves regarding the grain boundary.

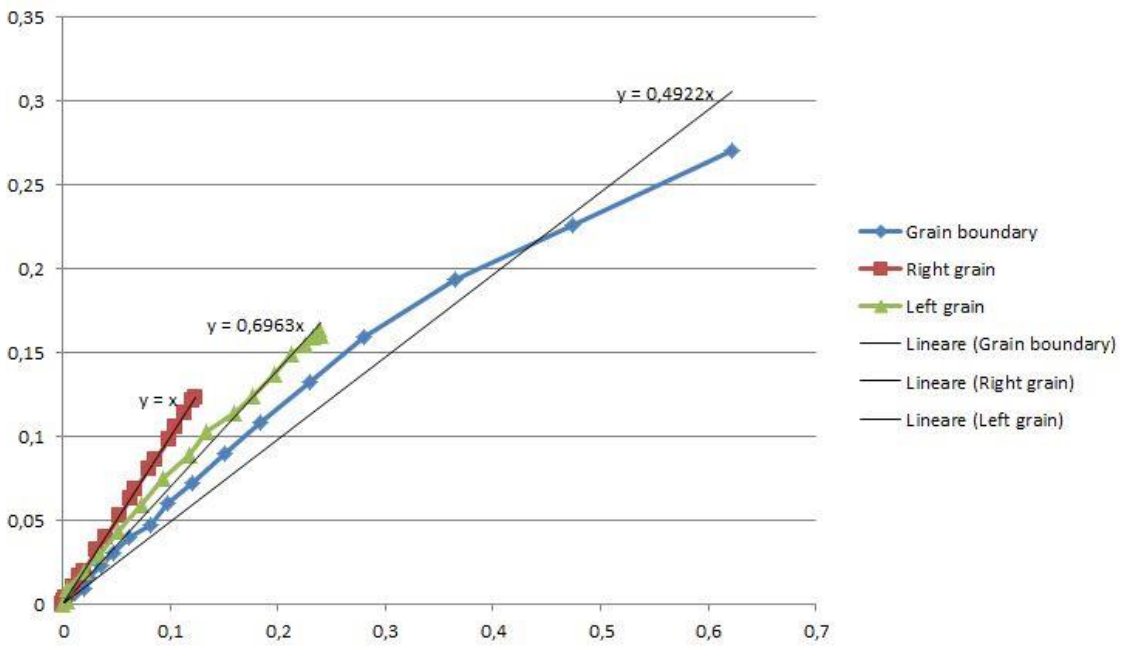


Fig 6.82 – Transverse strain (absolute value) vs Longitudinal strain for left grain, right grain and grain boundary

6.2.4 Sample “A8”

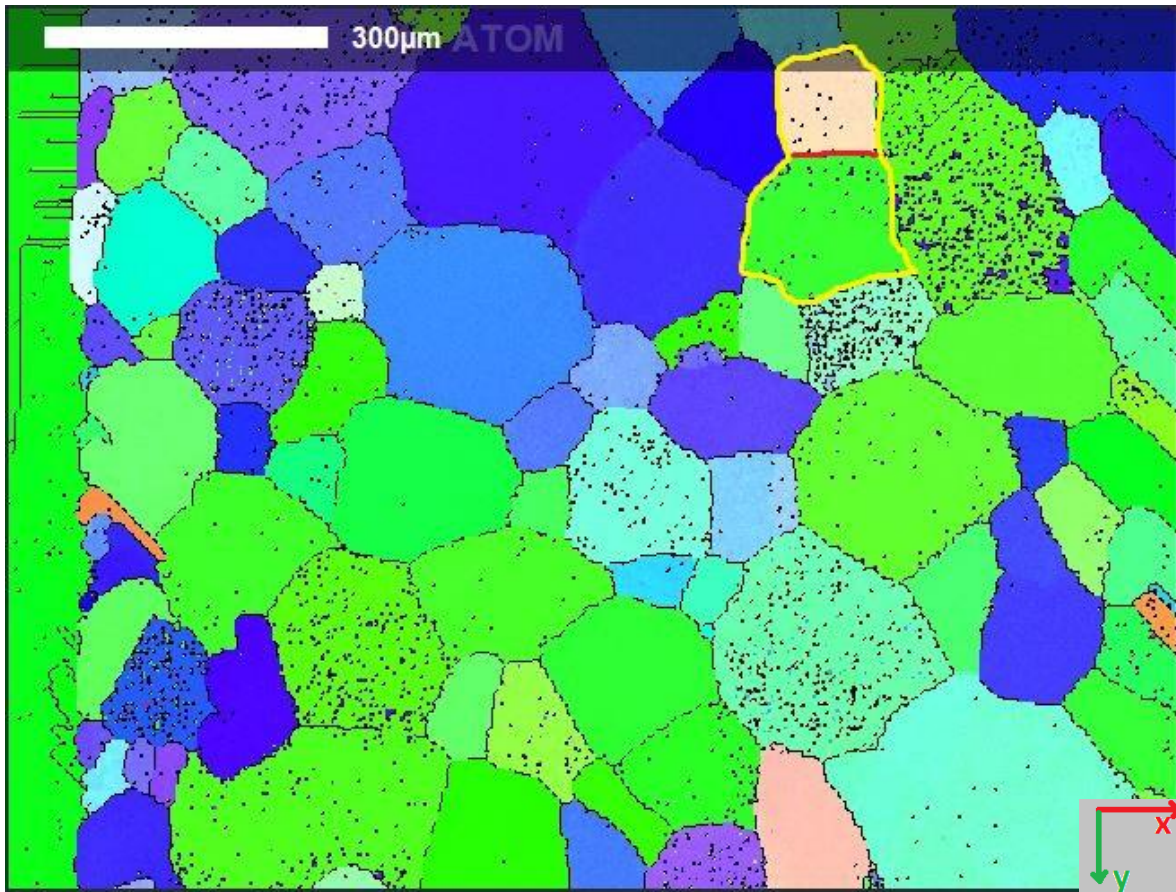


Fig 6.83 – EBSD map regarding sample “A8”

The gauge of the sample “A8” is filled by the two crystals marked in yellow. The grain boundary is indicated with the red colour (Fig. 6.83). The “green” crystal will be on the right side in the next pictures while the “pink” one will be on the left.

“Green” crystal Euler angles are:

- $\Phi = 150.83^\circ$
- $\Theta = 105.24^\circ$
- $\Psi = 25.33^\circ$

“Pink” crystal Euler angles are:

- $\Phi = 40.83^\circ$
- $\Theta = 51.39^\circ$
- $\Psi = 43.65^\circ$

The grain boundary misorientation is equal to 67° .

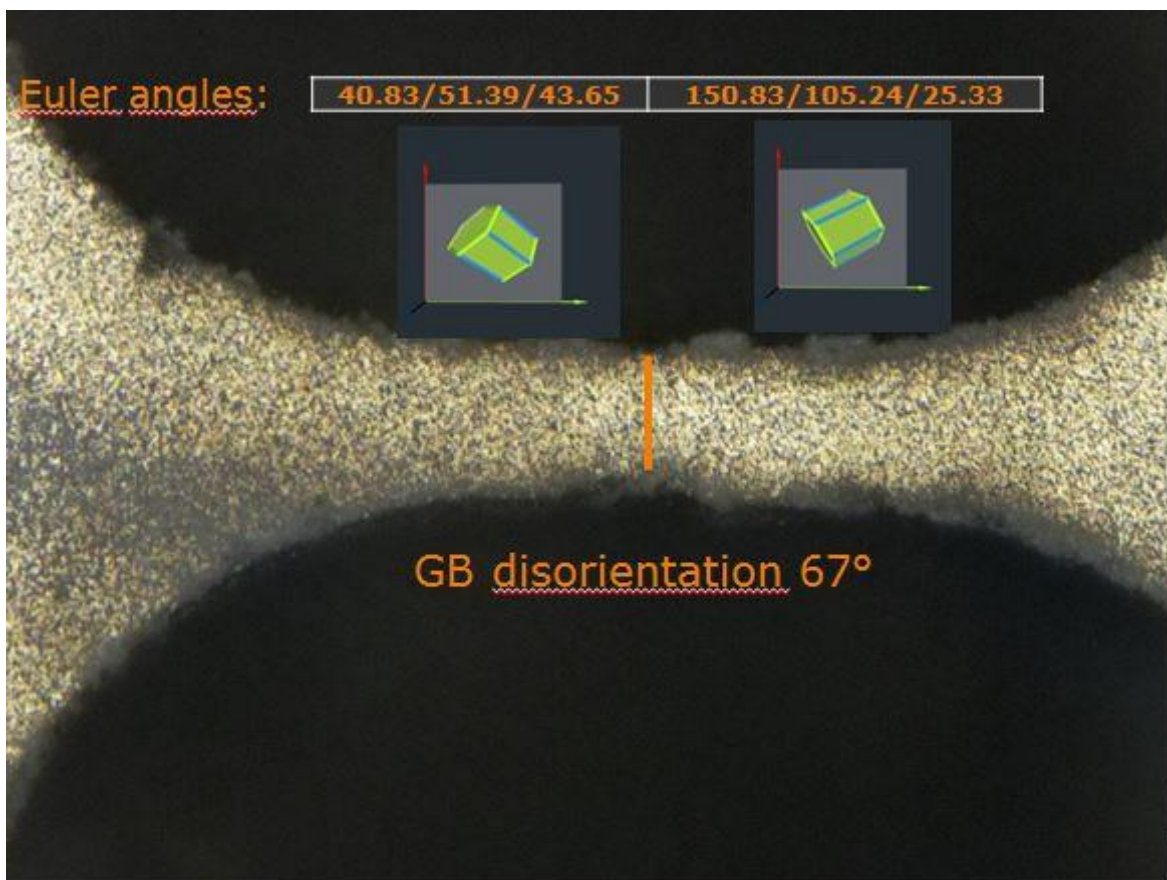
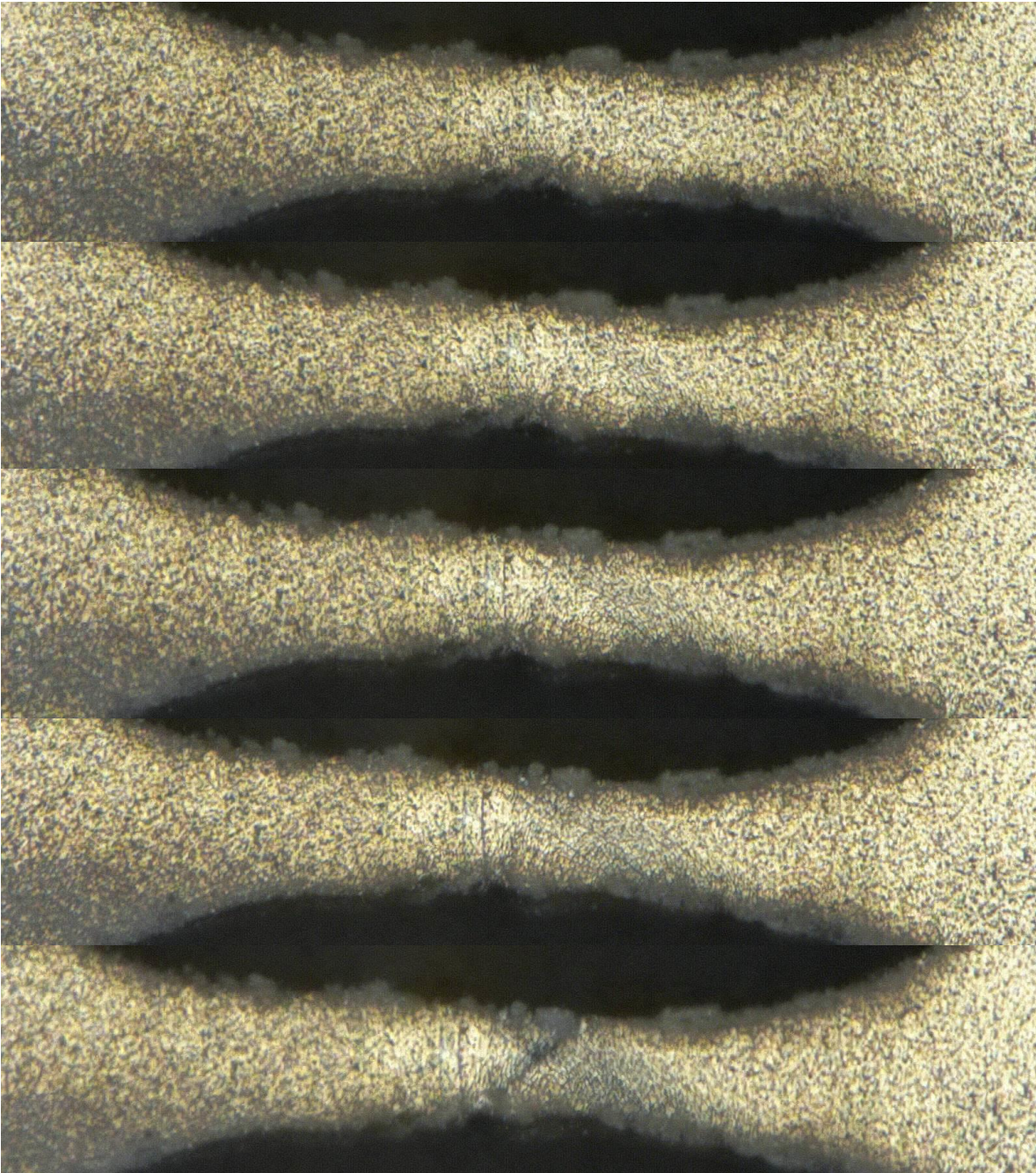


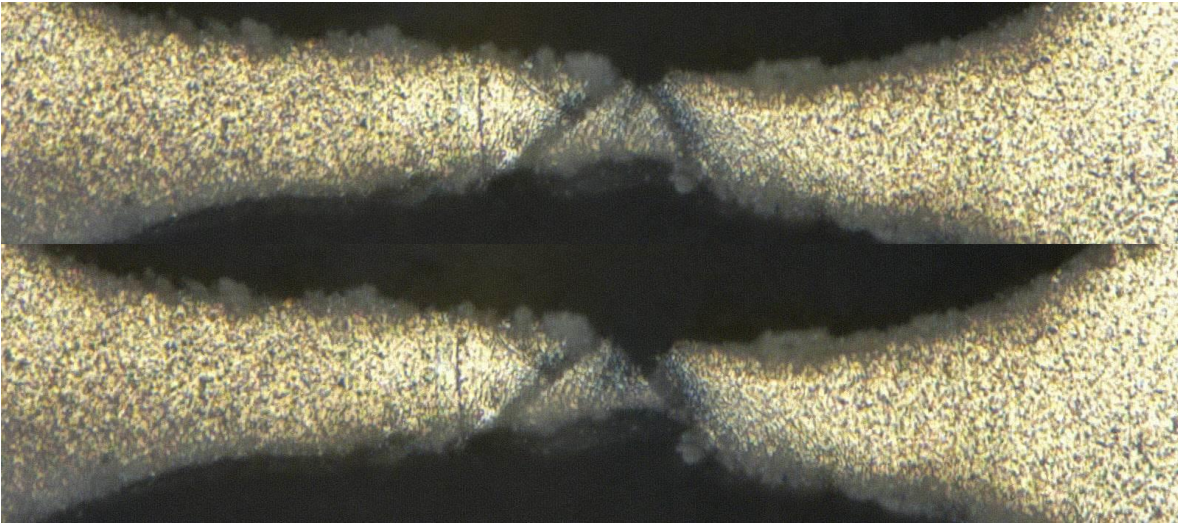
Fig 6.84 – Un-deformed configuration sample “A8”

Gauge dimensions are:

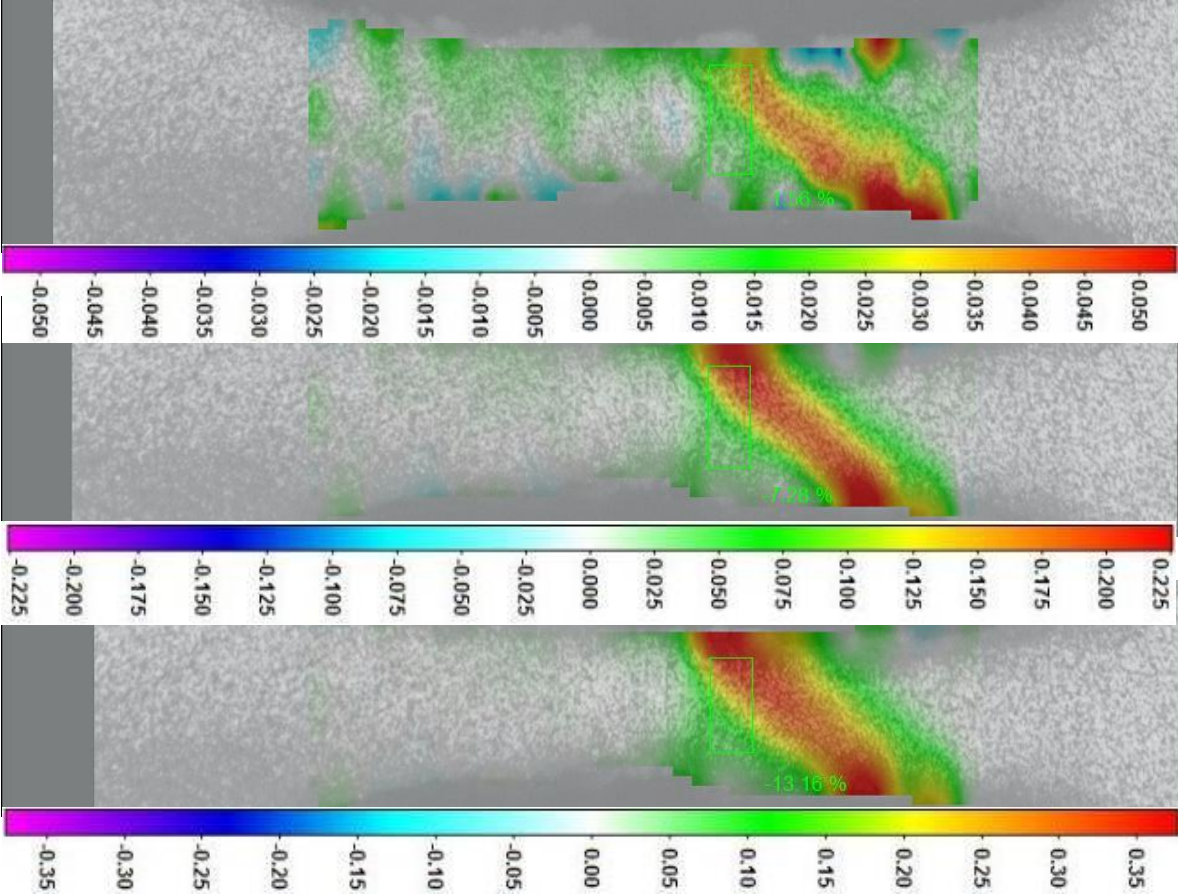
- Gauge length = $100\ \mu\text{m}$

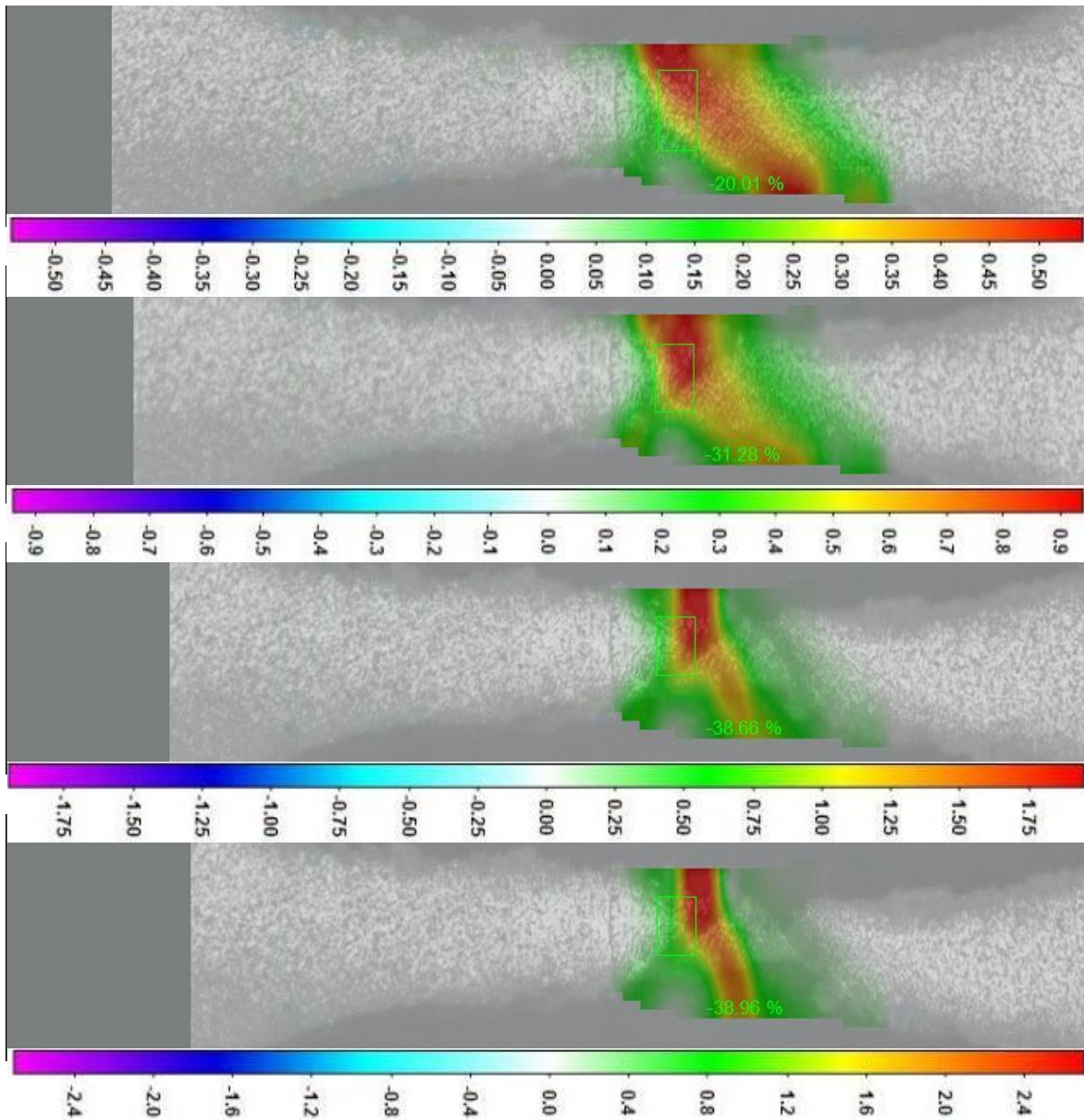
- Gauge width where the grain boundary stands = $39\ \mu\text{m}$
- Gauge width where the grains are analyzed = $42\ \mu\text{m}$
- Gauge thickness = $30\ \mu\text{m}$





From Fig. 6.85 to Fig 6.91 – Summary of tensile test regarding sample “A8”. Same reference as Fig. 6.84.





From Fig 6.92 to Fig 6.98 – Longitudinal strain maps referring to the previous seven pictures

The DIC study shows that the deformation is localized in the right grain. The left grain (Fig. 6.99 and Fig. 6.100) is stronger and its final value of longitudinal strain is ~2%. Right grain yield strength is about 270 MPa. Left grain yield strength is ~295 MPa. The grain boundary only deforms until 6.5%.

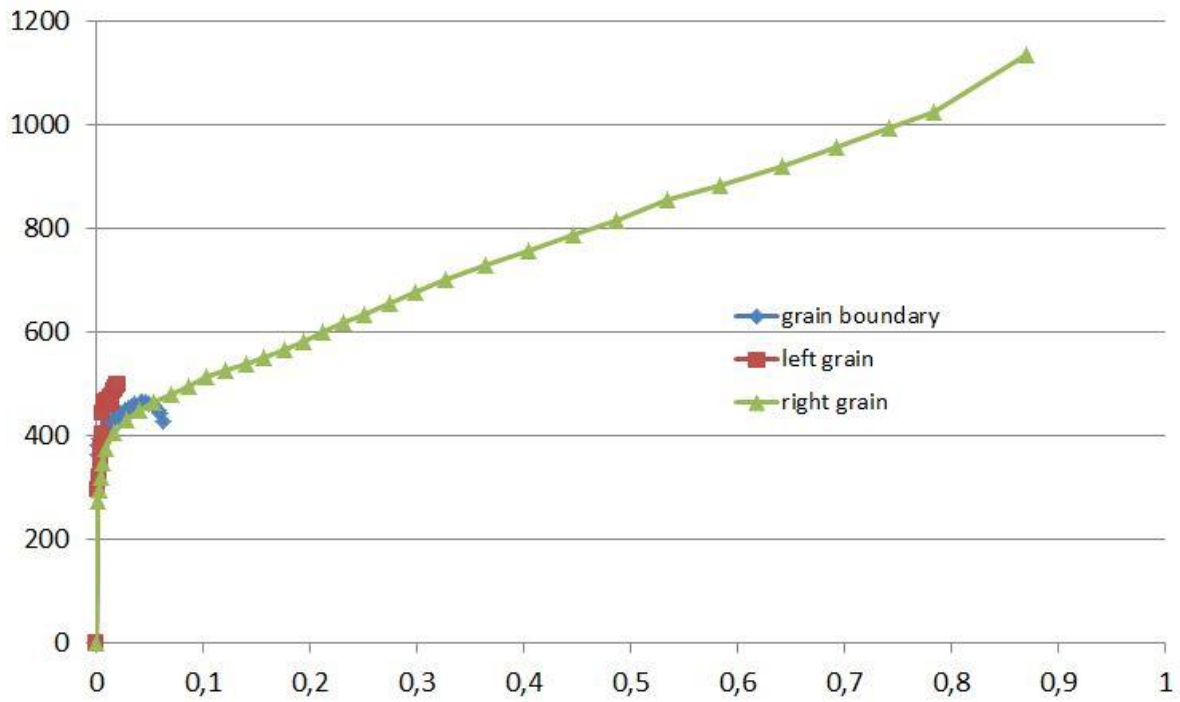


Fig 6.99 – True Stress [MPa] vs Longitudinal strain for left grain, right grain and grain boundary

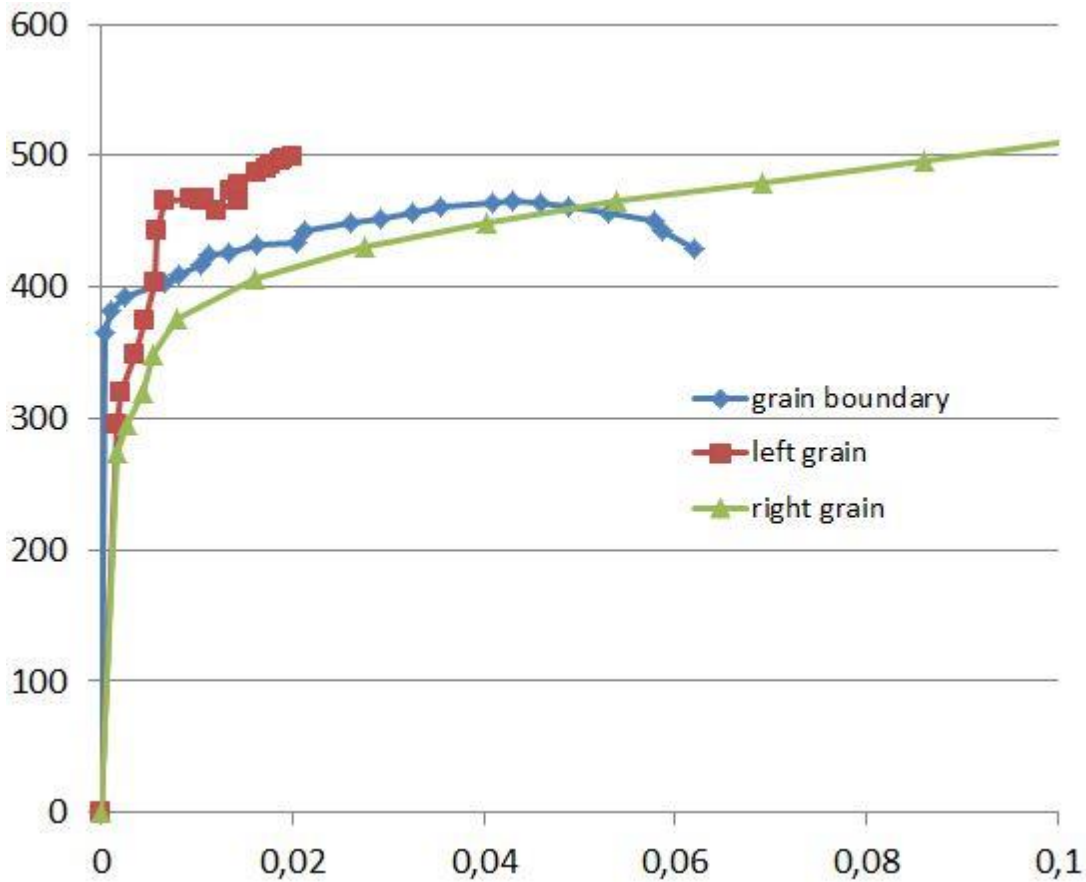


Fig 6.100 – Zoom on True Stress [MPa] vs Longitudinal strain for left grain, right grain and grain boundary

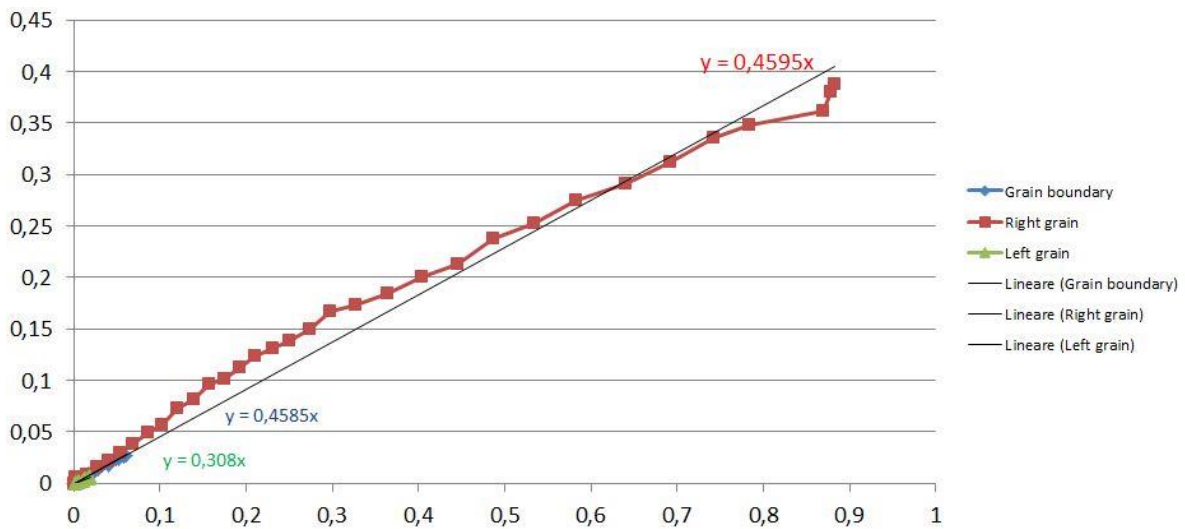


Fig 6.101 – Transverse strain (absolute value) vs Longitudinal strain for left grain, right grain and grain boundary.

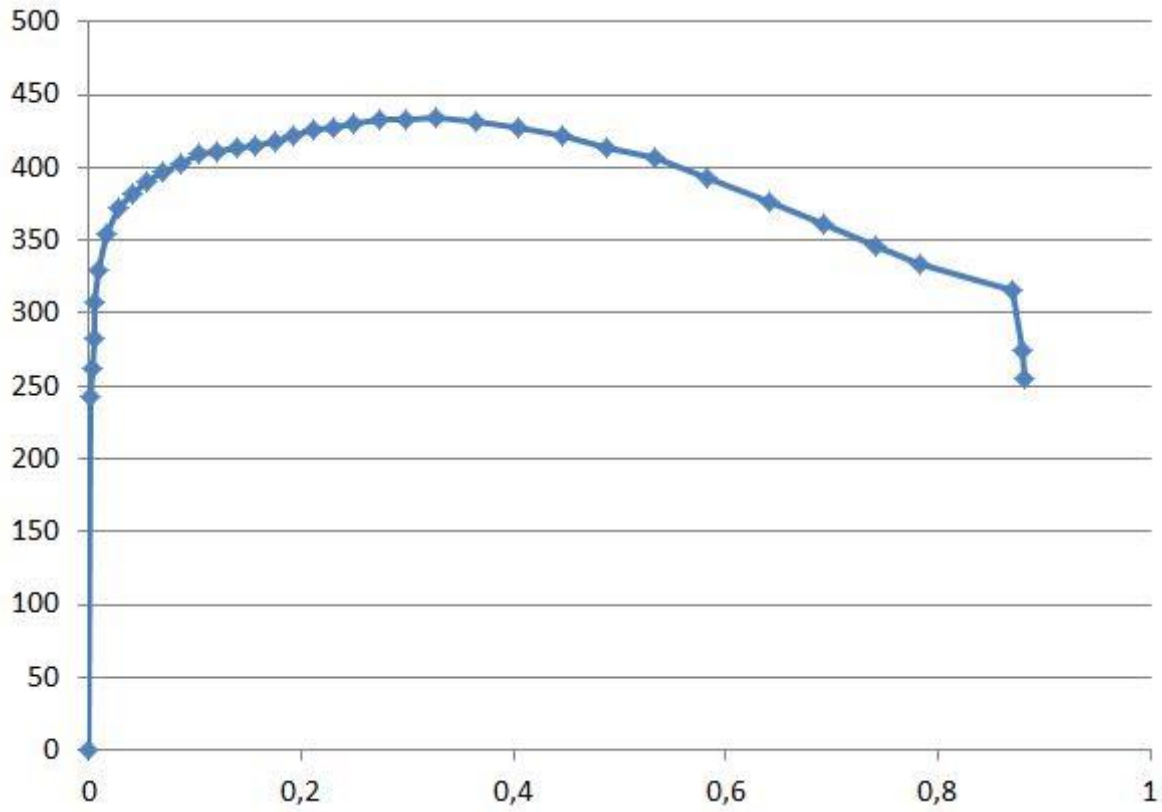


Fig. 6.102 – Engineering Stress [MPa] vs Longitudinal strain for right grain.

Chapter 7 Results analysis

7.1 Single grain boundaries behaviour

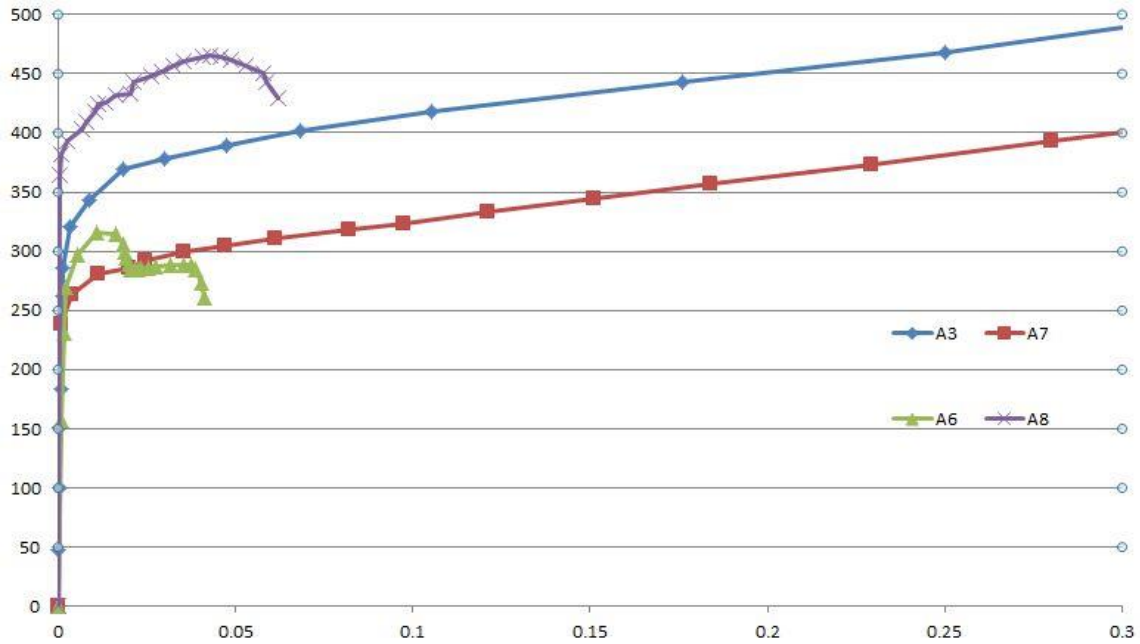


Fig. 7.1 – Grain boundaries True Stress [MPa] – Longitudinal Strain curves explaining the grain boundaries of the analyzed sample. Grain boundary of sample A3 in blue, sample A7 in red, sample A6 in green and sample A8 in violet.

Fig. 7.1 shows that it is not possible to characterize the strength of grain boundaries in CP titanium or, in other words, to obtain a single true stress – longitudinal strain curve that explains, globally, the behaviour of the grain boundaries. In Fig. 6.33, it can be seen how the true stress – strain curve of the boundary in sample “A3” has the same trend the weaker grain has too. A similar comment can be done for the sample “A6” grain boundary in Fig. 6.57 and for the sample “A7” in Fig. 6.79. Although boundaries “A6” and “A8” have very similar misorientation angles (respectively 66° and 67°), their curves are a lot different. Also, the two boundaries deform until different

values of longitudinal strain (2.5% for sample “A6” boundary, 6.5% for sample “A8” boundary”). This may confirm the fact that the behaviour of the boundaries depends on the strength of the adjacent crystals.

Taking a look at the misorientation angles of the grain boundaries, it can be noticed that, in case of a low misorientation angle (up to 31°), the fracture always occurred at the boundary (intergranular fracture). On the other hand, with high misorientation angles, the fracture was transgranular. Moreover, as the misorientation angle rises, it can be observed from the tensile tests pictures that the grain boundary tends to decrease the deformation in percentage and to increase the hinder of dislocations.

Table 7.1 – Table that explains the relation between misorientation angle and type of fracture.

	Grain boundary misorientation	Type of fracture
Sample “A3”	17.5°	Intergranular
Sample “A4”	30°	Intergranular
Sample “A6”	66°	Transgranular
Sample “A7”	31°	Intergranular
Sample “A8”	67°	Transgranular

Obviously, more experiments are required to confirm the results presented in Table 7.1.

7.2 Single crystals behaviour

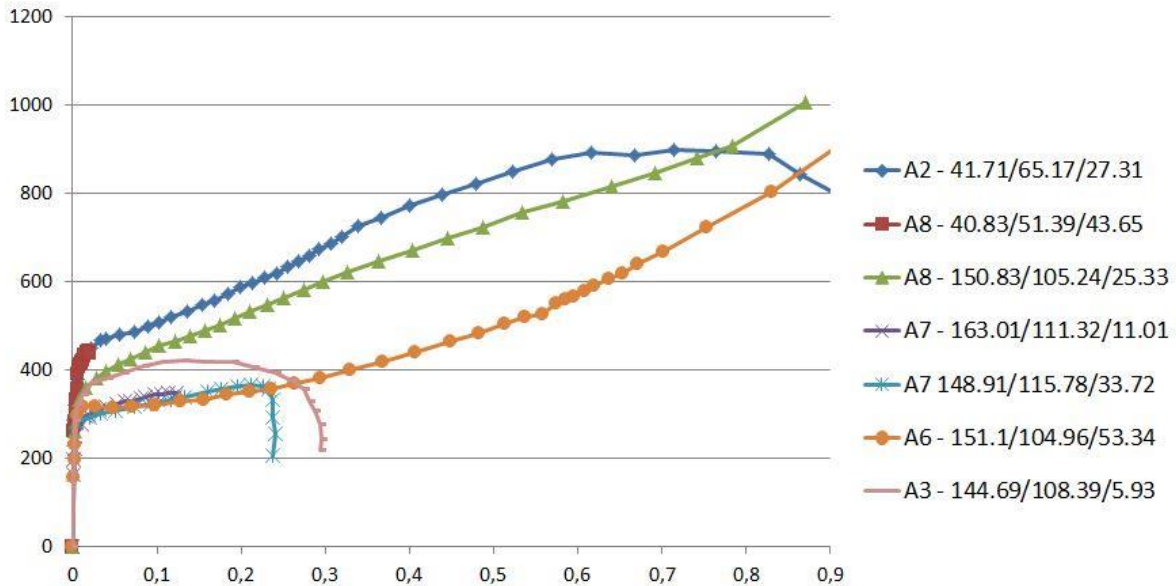


Fig. 7.2 – True Stress [MPa] vs Longitudinal Strain from analyzed crystals

In Fig. 7.2, crystals with Euler angles equal to 41.71/65.17/27.31 (blue curve), 150.83/105.24/25.33 (green curve) and 151.1/104.96/53.34 (orange curve) present full curves as they were the locus of fracture.

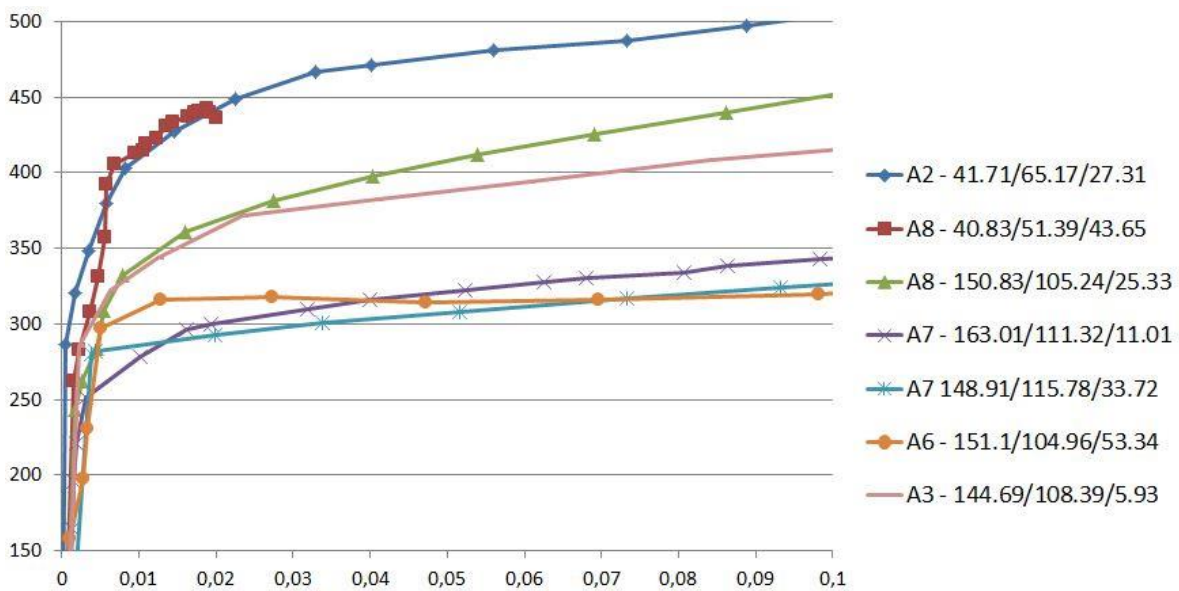


Fig. 7.3 – Zoom on True Stress [MPa] vs Longitudinal Strain from analyzed crystals

Fig. 7.3 and Fig. 7.4 show deep differences between the various true stress – strain curves of the given crystals. The differences are not only in terms of yield strength, but also in the evolution of the plastic deformation. In particular, crystals with orientation 41.71/65.17/27.31 and 40.83/51.39/43.65 (respectively blue and red curves in Fig. 7.3 and Fig 7.4) are the ones with better mechanical properties; their curves almost overlap, which could be expected for their similar orientations. Although the other crystals have comparable Euler angles, grains with orientations 150.83/105.24/25.33 and 144.69/108.39/5.93 (respectively green and pink curves in Fig. 7.3 and Fig 7.4) present better mechanical properties in the true stress – strain curves.

From the previous pictures, the peculiar behaviour of crystal with orientation 151.1/104.96/53.54 (orange curve) can be noticed as well. In fact, although it presents one of the highest yield strength recorded, its beginning of the strain hardening part is pretty flat. On the contrary, by taking a look at the blue curve, or also at the green curves, the start of the plastic deformation is characterized by a rapid increase of the stress. This is likely to be due to different slip systems activities that take place during the plastic deformation. If the first slip system to activate can be in some way predicted through the Schmid law, it is not easy to foresee what happens after. Also, observing the tensile tests pictures, it is possible to notice some differences: from Fig. 6.4 to Fig 6.17 (pictures regarding the tensile test and DIC for the crystal in blue in Fig. 7.3-7.4), it can be examined how the deformation is focused in a reduced part of the gauge and, furthermore, how is tricky to see slip bands. On the other hand, observing from Fig. 6.85 to Fig 6.98 (pictures regarding the tensile test and DIC for the crystal in green in Fig. 7.3-7.4), the deformation is evenly distributed in the crystal. The same thing happens, in an even clearer way, in

the orange crystal from Fig. 6.41 to 6.56 (17 pictures regarding the tensile test and DIC for the crystal in orange in Fig. 7.3-7.4), where the slip bands are clearly visible. After the slip bands encounter the grain boundary and get hindered, the deformation localizes in a particular part of the gauge, and there will be the locus of fracture.

The other crystals analyzed do not present high values of strain as they are not fractured grains. Of course the deformation, in these cases, stayed low because it was adjacent to a weaker crystal or grain boundary. All of them yielded though, for this reason, considerations about the primary slip system and, consequently, on the experimental CRSS can be done.

7.2.1 Determination of the experimental CRSS and comparison with the literature

As already explained previously, the CRSS and the yield stress are linked with the Schmid law. Through a parameterization of the HCP crystal lattice, it is possible to find, by knowing the crystal orientation and the tensile direction, the angles λ and φ that constitute the Schmid factor for each slip system. Through the knowledge of the Schmid factors and of the CRSS values found in the literature, the first slip system that occurs can be known and, consequently, the corresponding yield stress predicted. In the present research, a comparison between the predicted values of yield strength and the experimental ones extracted from the true stress – strain curves is performed. Then, the latter values are used to obtain experimental CRSS values that are

finally compared with the literature ones in order to see if there is an accordance between literature and experimental results.

The average CRSS values extracted from previous studies for the prediction are 127 MPa for the basal $\langle a \rangle$ (3 basal slip systems), 96 MPa for the prismatic $\langle a \rangle$ (3 prismatic slip systems) and 240 MPa for the 1st order pyramidal $\langle c+a \rangle$ (6 pyramidal slip systems). No data is available for the 2nd order pyramidal $\langle c+a \rangle$, most probably because of the high values of stresses necessary to activate this slip system, and the difficulty to perform, identify and analyse the type of experiment needed to acquire this data.

Table 7.2 – Summary of the predicted values of yield strength, experimental values of yield strength and experimental values of crss obtained from the samples analysis.

Sample-Grain	Euler angles	Slip Systems	Schmid Factor	Average Predicted Yield Strength [Mpa]	Experimental Yield Strength	Experimental CRSS [Mpa]
A2	41.71/65.17/27.31	Basal 13	0,49799	255,0252013	290	144,4171
		Prismatic 21	0,24345	394,3314849		
		Pyramidal 87	0,33951	706,9011222		
A3-LG	137.83/107.21/49.57	Basal 11	0,43933	289,0765484	270	118,6191
		Prismatic 33	0,22213	432,1793544		
		Pyramidal 54	0,38661	620,7806316		
A3-RG	144.69/108.39/5.93	Basal 13	0,46578	272,6609129	290	136,00776
		Prismatic 42	0,19903	482,3393458		
		Pyramidal 65	0,39383	609,3999949		
A6-LG	151.1/104.96/53.34	Basal 13	0,39739	319,585294	295	117,23005
		Prismatic 21	0,12730	754,1241163		
		Pyramidal 54	0,46057	521,0934277		
A6-RG	38.72/71.54/2.75	Basal 13	0,47116	269,5474998	270	127,2132
		Prismatic 42	0,22416	428,2655246		
		Pyramidal 98	0,37906	633,1451485		
A7-LG	148.91/115.78/33.72	Basal 13	0,49064	258,8455894	280	137,3792
		Prismatic 42	0,18242	526,2580857		
		Pyramidal 54	0,40749	588,9715085		
A7-RG	163.01/111.32/11.01	Basal 12	0,37763	336,3080264	250	94,4075
		Prismatic 33	0,10085	951,9087754		
		Pyramidal 65	0,48507	494,7739502		
A8-LG	40.83/51.39/43.65	Basal 13	0,47241	268,8342753	295	139,36095
		Prismatic 21	0,31503	304,7328826		
		Pyramidal 109	0,34472	696,2172198		
A8-RG	150.83/105.24/25.33	Basal 13	0,45387	279,8158063	270	122,5449
		Prismatic 21	0,12597	762,086211		
		Pyramidal 54	0,46288	518,4929139		

As it can be seen from Table 7.2, the first slip system to occur is:

- Basal in A2, A3-LG, A3-RG, A6-LG, A6-RG, A7-LG, A7-RG, A8-RG.
Likely to be basal in A8-LG.
- Likely to be prismatic in A8-LG
- Never pyramidal.

Table 7.3 – Experimental CRSS values and average.

Family	Experimental CRSS values [MPa]									Average
<a> Basal	144	119	136	117	127	137	94	139	122	126,1
<a> Prismatic								93		93

Table 7.3 shows that the average of the experimental CRSS values which refer to basal slip systems is 126,1 MPa. The standard deviation regarding the basal family is equal to 14. On the other hand, the average of the CRSS values concerning prismatic slip system is 93 MPa. These results are in agreement with the previous researches from the literature.

7.3 Fractography

Fracture surfaces of samples were studied using scanning electron microscopy. The lack of fibrous appearance suggests the fracture is not ductile. Ductile fracture is not expected as, from previous research, fracture of titanium changes from ductile (in the fine grained 1 and 20 μm) [15] to brittle in coarse-grained CP Ti (about 1 mm) [16].

Fractures in fig. 7.4, 7.5, 7.6, 7.7, 7.9 are intergranular while fractures in fig 7.8 and 7.10 are transgranular. Looking at these pictures, it is possible to notice how the intergranular fractures focus on a much reduced area tending to the outside of the cross sectional area. On the contrary, the transgranular fractures are recognizable from the dislocation lines and happen on a more central area (still reduced).

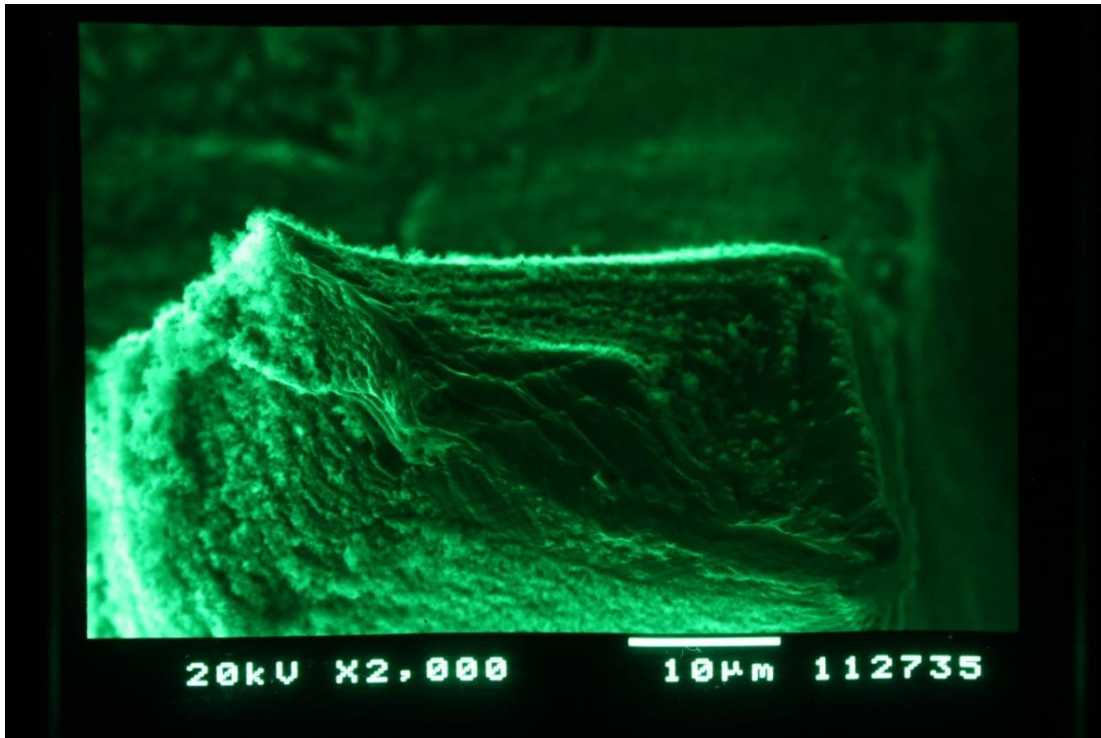


Fig. 7.4 – Close up view of fractured surface sample “A3”.

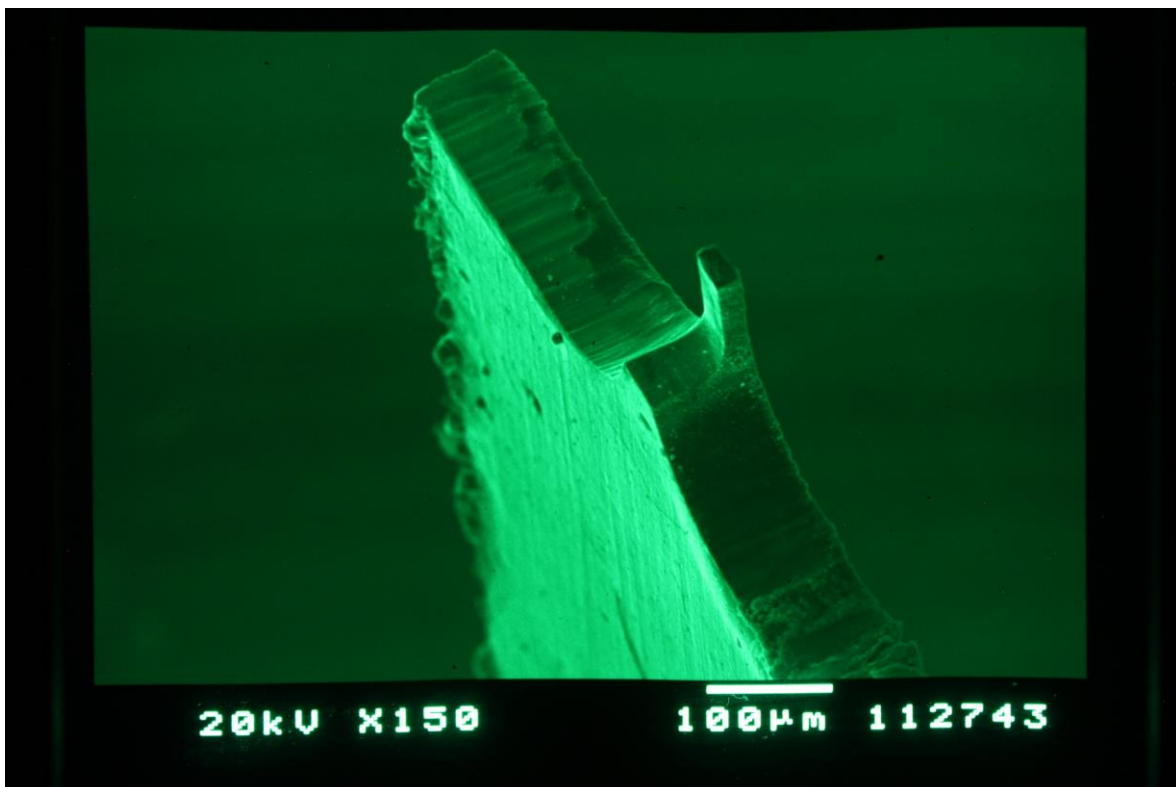


Fig. 7.5 – Fractured surface sample “A4”.

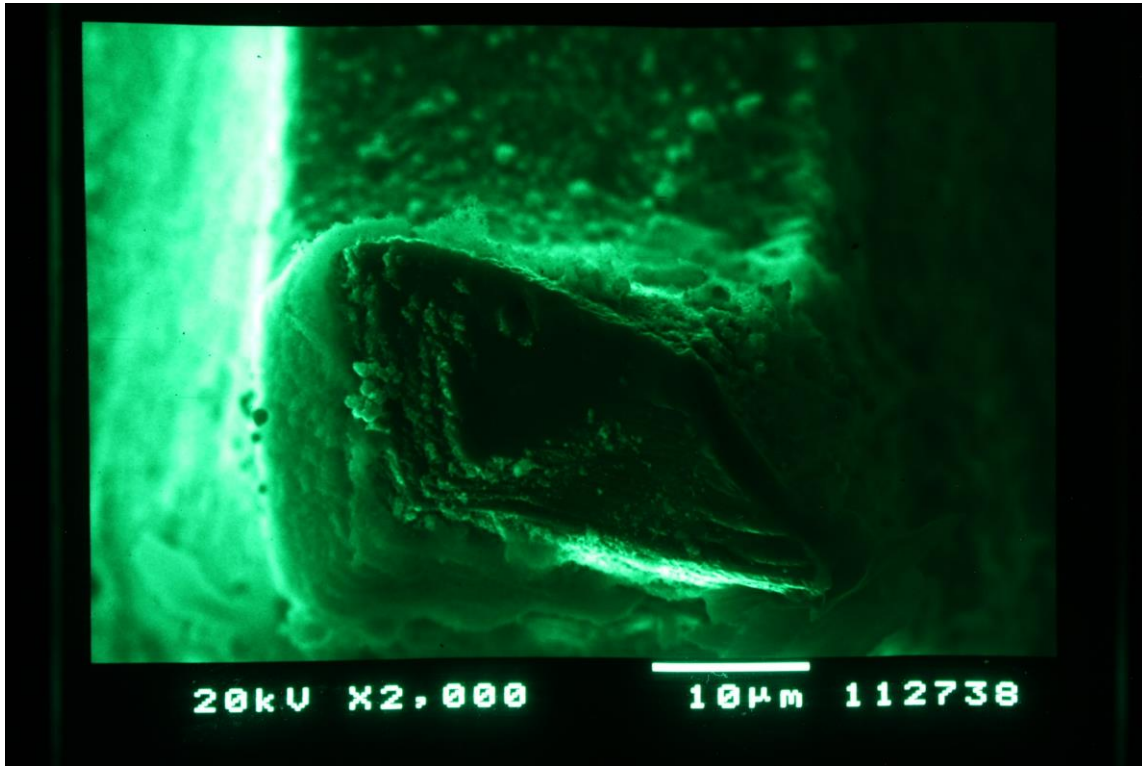


Fig. 7.6 - Close up view of fractured surface sample "A4".

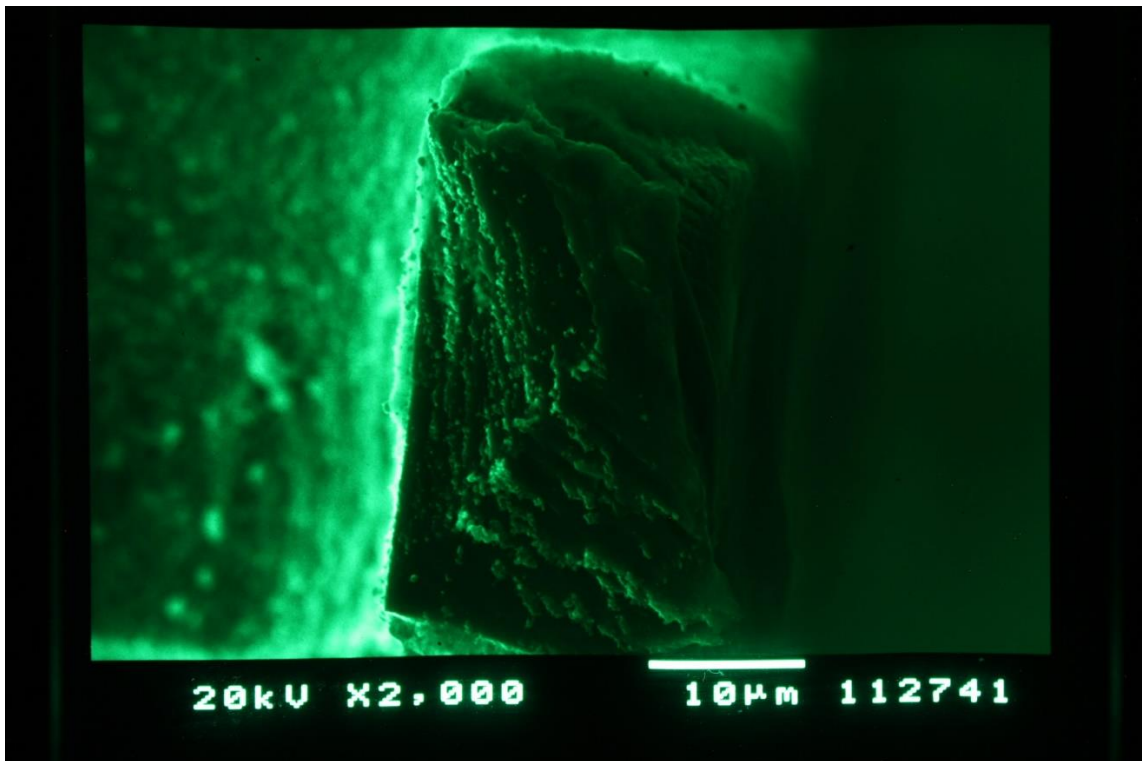


Fig. 7.7 – Second close up view of fractured surface sample "A4".

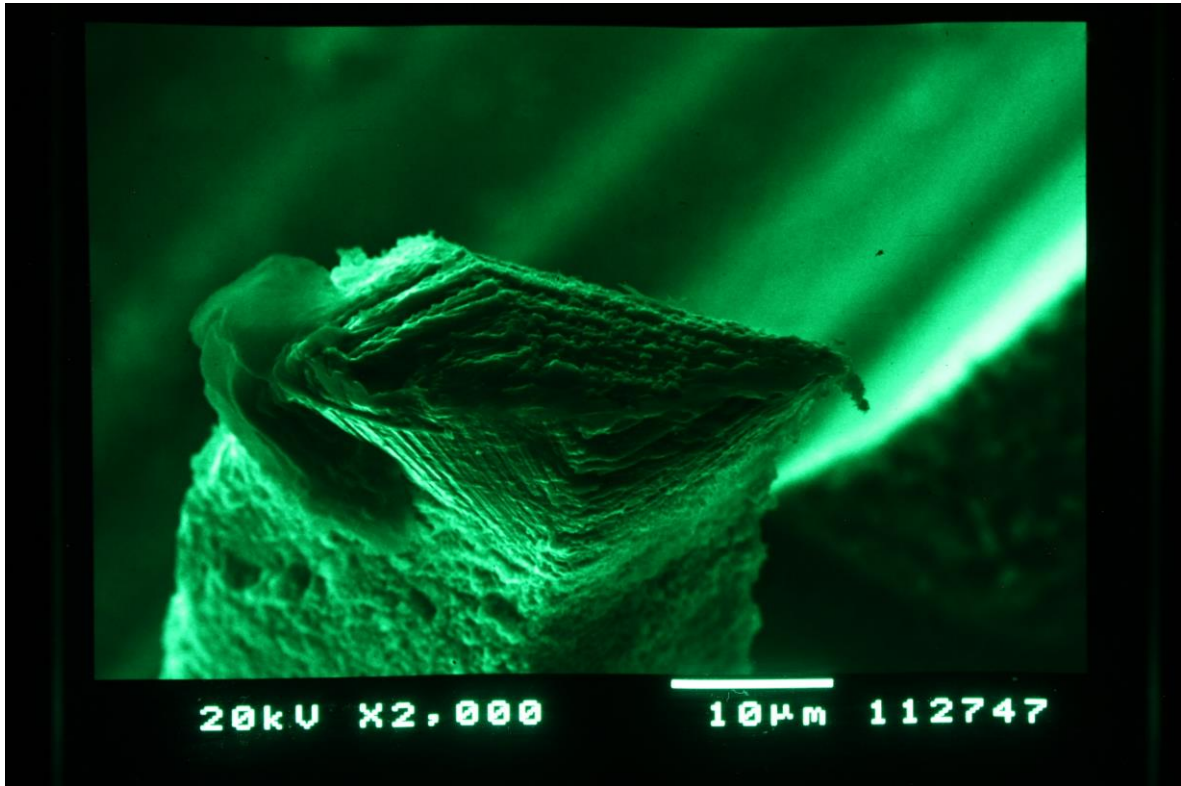


Fig. 7.8 - Close up view of fractured surface sample "A6".

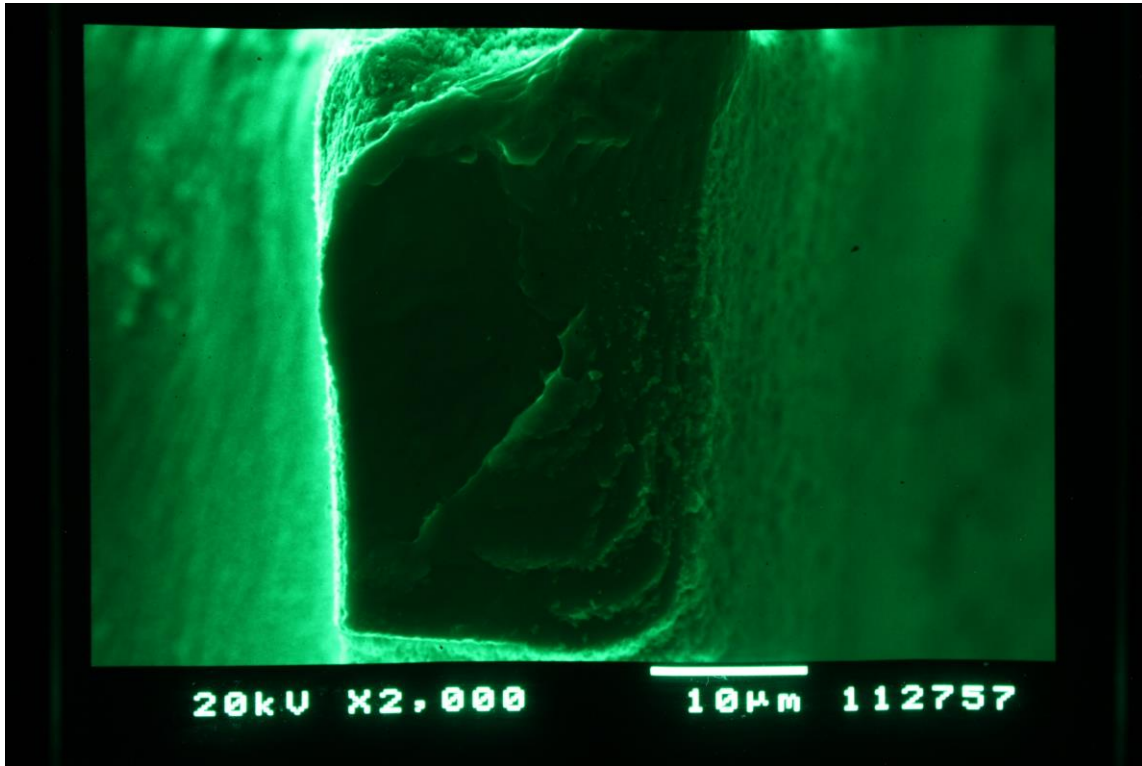


Fig. 7.9 - Close up view of fractured surface sample "A7".

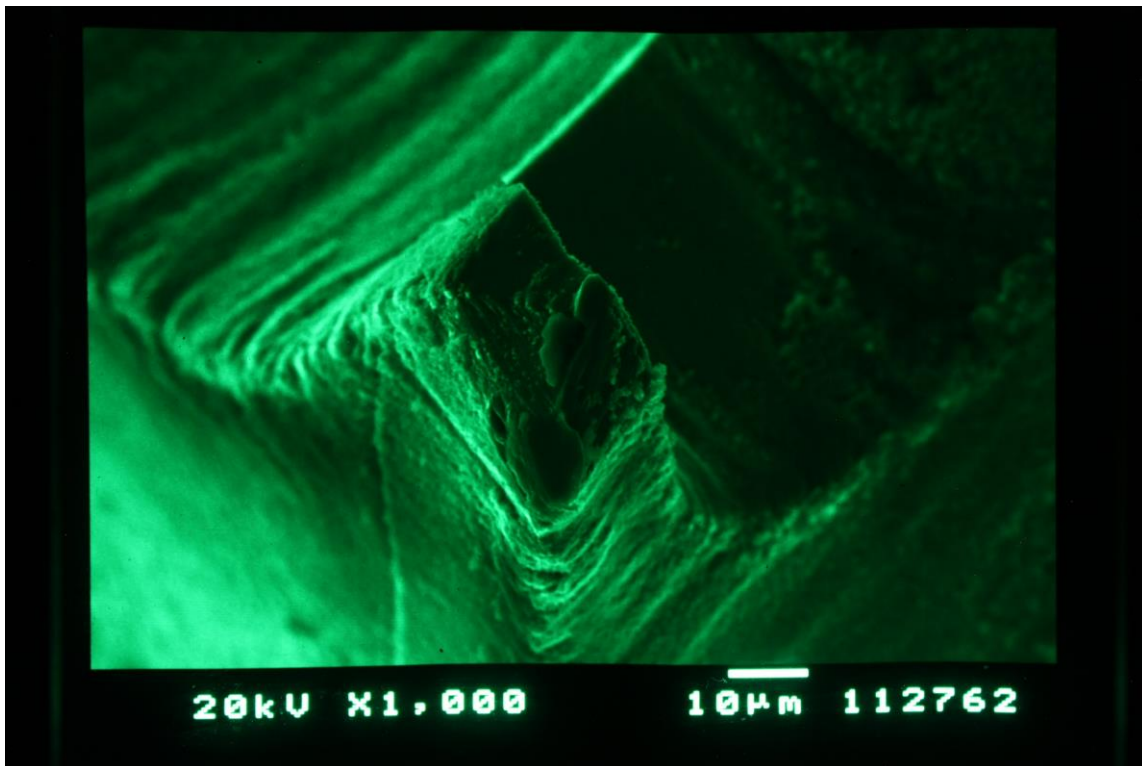


Fig. 7.10 - Close up view of fractured surface sample "A8".

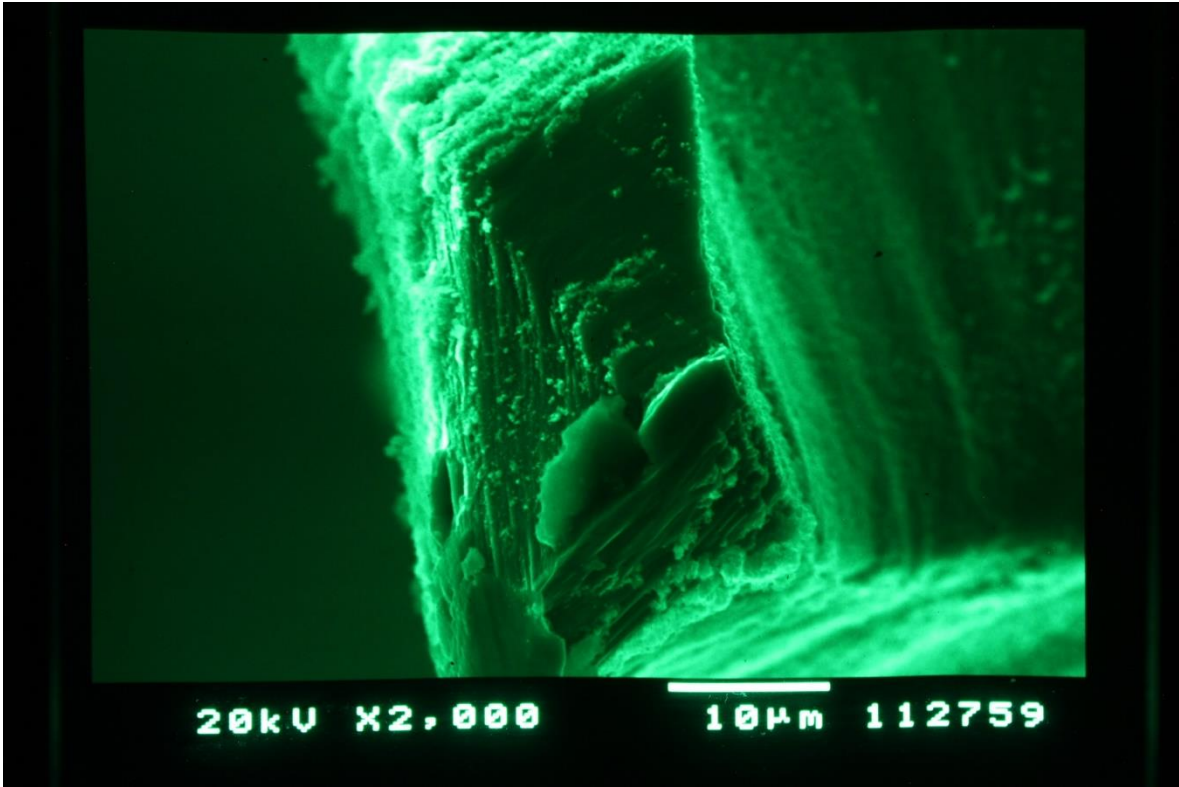


Fig. 7.10 – Second close up view of fractured surface sample “A8”.

Chapter 8 Discussions and Conclusions

8.1 Discussions

In the present study, the reader has surely noticed that the cross sectional areas of the samples analyzed do not coincide. It can be affirmed that the size of the gauge section does not have an influence on the experimental CRSS that have been obtained from the tests. In fact, by taking a look at Fig. 2.6, the CRSS tends to be a stable value when the width of cantilevers reaches about 10 μm . The dimensions of this study are in the flat part of the curve in Fig. 2.6. The first idea was to obtain samples with gauge area equal to 30 μm (width) x 30 μm (thickness). Then, in order to focus the deformation on the xy plane (the plane recorded by the digital camera), it was decided to increase the width and decrease the thickness. These small variations did not affect the results of the tests, as it can be seen from the experimental CRSS results that match with the literature.

Although the “speckle pattern” obtained on these specimens was qualitative, DIC strain data regarding the very start of the tensile tests, and therefore the start of the elastic deformation were not fully reliable as it can be seen, for instance, in Fig. 6.49. A longer gauge length could be realized in order to improve the quality of data. Also, one could try to perform tensile tests in SEM where a higher magnification can be exploited; in the latter case, the researcher must be able to take pictures with enough contrast between the surface of the sample and the pattern which is not as easy as under digital microscope. Because of the previous considerations, this study lacks of comparisons between the single crystals in terms of Young’s modulus and

Poisson ratio which would have been interesting and would have enriched the literature (eventual Young's modulus can be compared with those in Fig. 2.2).

The accuracy of DIC in the part of surface where the fracture is occurring (high strain) diminishes because the portion of pattern tends to spread out vertiginously or even “disappear”, and also the contrast decreases significantly. This is one limitation of the DIC combined with the digital microscope.

Another aspect that could be improved is the laser micromachining cut. As it can be seen in pictures taken in SEM, there are signs of debris on the side of the gauge that do not help at the moment of the cross sectional area definition and also, decrease the clarity of the images. Furthermore, once the micromachining process has arrived at its third or last step (Chapter 4.2.1), the power values are reduced in order to make a more precise cut. This may lead to a cut not perfectly perpendicular which implies a trapezoidal area rather than a rectangular area. An optimization of parameters is required to fix these inaccuracies. Furthermore, micromachining in vacuum seems to improve the quality of the surfaces and may represent a further improvement.

Moreover, as it can be seen from the orientations of the analyzed crystals, the Φ values were mostly around 40° or 150° , the Θ values were mostly around 60° or 110° . The Ψ values varied more, but were still ranged between 5° and 53° . In the next figure, one can notice how those orientations were greater in number.

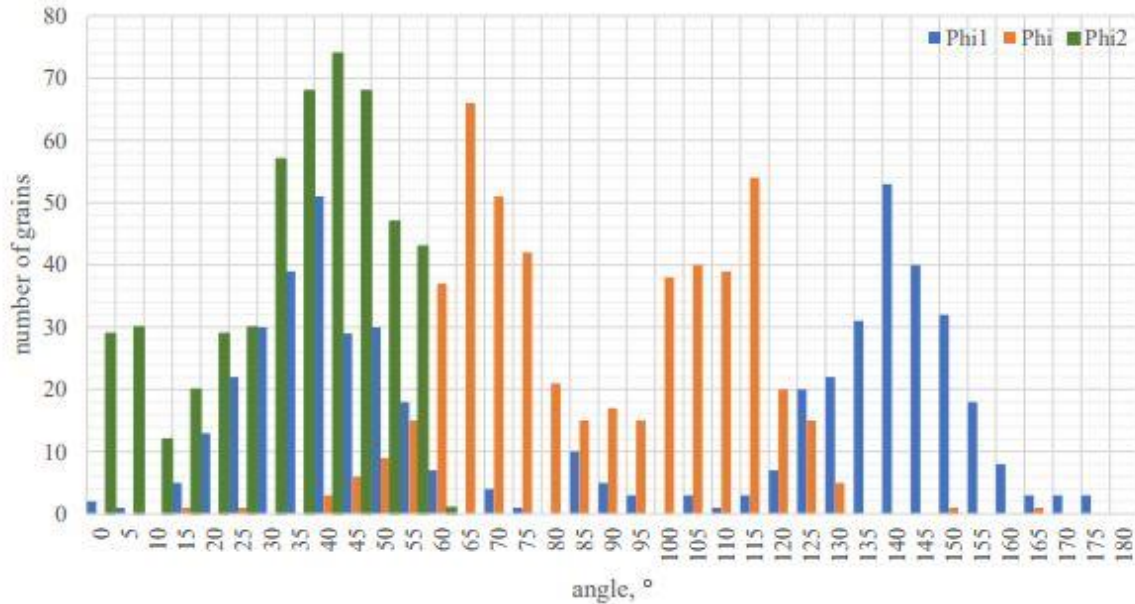


Fig. 8.1 – Number of crystals vs Euler angles. Phi1 is Φ , Phi is Θ , Phi2 is Ψ .

Fig. 8.1 considers the totality of the crystals of all the EBSD maps created in this study. Because of the expectation to find random orientations, the coupons were all cut according to the rolling direction. By cutting the coupons following different directions, many more orientations could have been analyzed.

Prismatic and basal slip systems are the ones occurring more frequently and the reason dwells in their lower CRSS value. In this study, unfortunately no pyramidal slip systems were possible to analyze. In order to analyze this type of slip systems, a reverse process could be executed. Taking the advantage of the excel sheet that has been implemented to find the Schmid factors, instead of giving Euler angles and tensile direction as input and obtaining Schmid factors as output, it could be done the opposite by using definite functions. Once the couples of tensile direction and Euler angles (that define the orientation of the crystal whose principal slip system is pyramidal) are known, a modification to the experimental procedure could be realized. The

modification would consist in cutting a square piece out of the titanium foil that includes a large number of grains, then polishing it, performing EBSD and finally, identifying the orientation. At this point, the researcher can cut the specimen (with the chosen grain in the gauge length) out of the square piece along the corresponding tensile direction with the femtosecond laser.

Finally, in order to have a 360 degrees view, more experiments involving many type of slip system are needed. Finite element analysis (FEA) would be useful to simulate the tensile tests on crystals with same orientation as in the experiments and, consequently, to compare experimental and analytical data.

8.2 Conclusions

The initial aim of this project was to investigate the mechanical properties of CP titanium single crystals (HCP) and to characterize the strength of single grain boundaries. The crystals anisotropic behaviour was demonstrated by extracting different stress-strain curves from the tensile tests. The principal slip system was surely basal in all cases except one; although this, remarkable differences were noticed in terms of yield strength and plastic deformation phase. In particular, the recorded yield strength values from the experiments, within the basal family, went from ~250 MPa to ~295 MPa that corresponds to ~20% difference. This percentage could increase vertiginously if principal prismatic or pyramidal slip systems were analyzed. In fact, from the literature, the former could give lower yield strength values (minimum is ~160 MPa if you consider prismatic CRSS = 96 ± 18 MPa), the latter could give much higher yield strength values (minimum is ~480 MPa if pyramidal CRSS > 240 MPa is considered). This research, given the large data on basal slip systems, orientated itself on the experimental determination of the CRSS values for this

family through the extraction of the yield strength values from the experiments and the development of tools for the Schmid factors definition. The outcome of the study was successful as the experiments matched with the literature. In fact, a value of $CRSS = 127 \pm 33$ MPa was found in the literature. In the present study, the value of $CRSS = 126.1 \pm 14$ MPa was obtained; that demonstrates how these values are in agreement especially on average. Single grain boundaries were investigated in this study as well. After analyzing the stress-strain curves, it is not possible to assert those to be independent from the behaviour of the adjacent crystals. For this reason, considerations about their eventual mechanical properties are omitted. On the other hand, interesting insights were noticed regarding the grain boundaries misorientation angles. For angles up to 31° , the grain boundaries highly permitted dislocation motion and the samples showed intergranular fracture. On the contrary, for larger angles than 31° , the grain boundaries behaved as a constraint as they tended to hinder the dislocations; accordingly, the fracture was transgranular.

Bibliography

- [1] Imeco. <http://www.imeco.it/titanio-gradi.html>
- [2] Supra Alloys. <http://www.supraalloys.com/titanium-grades.php>
- [3] Smiths high performance data sheet [online].
http://www.smithshp.com/Italia/downloads/CPGrade1_SHP.pdf
- [4] Lütjering G, Williams JC. Titanium. vol. 2nd ed. Berlin;New York: Springer; 2007.
- [5] Zarkades A, Larson R. F. The Science, Technology and Application of Titanium. Oxford, UK: Pergamon Press; 1970.
- [6] Shechtman D, Brandon D. Orientation dependent slip in polycrystalline titanium. J Mater Sci 1973;8:1233–7. doi:10.1007/BF00549337.
- [7] Banerjee D, Williams JC. Microstructure and slip character in titanium alloys. Def Sci J 1986;36:191–206.
- [8] Sengerandu's tutorials.
<https://sengerandu.wordpress.com/tutorials/physical-metallurgy/crss/>
- [9] Zheng Z., Balint D.S., Dunne F., Rate sensitivity in discrete location plasticity in hexagonal close-packed crystals, Acta Materialia 107 (2016) 17-26.
- [10] Paton E. N, Baggerly G. R, Williams C. J. Rockwell Report. vol. SC 526.7FR. 1976.

- [11] L. Wang, Z. Zheng, H. Phukan, P. Kenesei, J.-S. Park, J. Lind, R. M. Suter and T. R. Bieler, "Direct measurement of critical resolved shear stress of prismatic and basal slip in polycrystalline Ti using high energy X-ray diffraction microscopy," *Acta Materialia*, vol. 132, pp. 598-610, June 2017.
- [12] J. Gong and A. J. Wilkinson, "Micro-Cantilever Testing of Prismatic Slip in Commercially Pure Ti", *Philosophical Magazine*, no. 91:7-9, pp. 1137-1149, 2011.
- [13] Schmid, Erich; Walter Boas (1935). *Kristallplastizität: Mit Besonderer Berücksichtigung der Metalle* (in German) (1st ed.). Springer. ISBN 978-3662342619.
- [14] Caceres, Pablo G. "Deformation of Single Crystals" (PDF). Retrieved 15 May 2014.
- [15] Conrad H, Keshavan MK, Sargent GA. No Title. Proc. 2nd Int. Conf. Mech. Behav. Mater., vol. Special Vo, Boston, Massachusetts; 1976, p. 538.
- [16] Amateau MF, Burrier HI, Ebert LJ. Brittle Fracture in Alpha-Titanium. *Trans Am Soc Met* 1966;59:921.
- [17] Morris J.W. Jr., Material Science.
<http://www.mse.berkeley.edu/groups/morris/MSE205/Extras/defects.pdf>
- [18] Wikipedia on Burgers vector.
https://en.wikipedia.org/wiki/Burgers_vector
- [19] Callister, William D. Jr. "Fundamentals of Materials Science and Engineering," John Wiley & Sons, Inc. Danvers, MA. (2005)

- [20] Kittel, Charles, "Introduction to Solid State Physics," 7th edition, John Wiley & Sons, Inc, (1996) pp 592–593.
- [21] Fujii K., Fukuya K., Development of Micro Tensile Testing Method in an FIB System for Evaluating Grain Boundary Strength, *Materials Transactions*, Vol. 52, No. 1 (2011) pp. 20 to 24.
- [22] K.J. Hemker and W.N. Sharpe, Jr, Microscale Characterization of Mechanical Properties, *Annu. Rev. Mater. Res.* 2007. 37:93–126
- [23] Ichikawa Y., Tokoro R., Ogawa K., Micro-scale strength evaluation for bonding interface of cold sprayed coatings, *Material Science Forum* ISSN: 1662-9752, Vol. 879, pp 795-800 (2017).
- [24] A.P. Alkhimov, V.F. Kosarev, and A.N. Papyrin, A Method of Cold Gas-Dynamic Deposition, *Sov. Phys. Dokl.* 35 (1990) 1047-1049.
- [25] A.N. Papyrin, Cold Spray Technology, *Adv. Mater. Processes.* 159 (2001) 49-51.
- [26] A.P. Alkhimov, A.N. Papyrin, V.F. Kosarev, N.I. Nesterovich, M.M. Shushpanov, European Patent 0 484 533 B1. (1995)
- [27] Y. Watanabe, Y. Ichikawa, I. Nonaka, Hideo Miura, Characterization of Cold-Sprayed Copper Coatings with New Evaluation Parameter of EBSD Method, *Thermal Spray 2013: Innovative Coating Solutions for the Global Economy.* (2013) 132-137.
- [28] Jameson, *Electrical Discharge Machining*, Society of Manufacturing Engineers, 2001.

- [29] Titanio e suo impiego nel settore motociclistico.
<http://www.ing.unitn.it/~colombo/MOTOTITANIO/TitanioMOTO.htm#trattamentermici>
- [30] Campbell, F. C. (2008). *Elements of metallurgy and engineering alloys*. Materials Park, Ohio: ASM International.
- [31] G.A. Salishchev and S.Yu. Mironov, Effect of grain size on mechanical properties of commercially pure titanium, *Russian Physics Journal*, Vol. 44, No. 6, 2001.
- [32] Gözden Torun, MICROSTRUCTURE AND MECHANICAL PROPERTIES OF CP-TITANIUM (GRADE 4) IMPLANT MATERIALS, Department of Metallurgical and Materials Engineering, METU, 06800 Ankara, Turkey.
- [33] M.J. Tan*, X.J. Zhu, Dynamic recrystallization in commercially pure titanium, *Journal of Achievements in Materials and Manufacturing Engineering*, Volume 18, 2006.
- [34] Pushkareva M., Study of Void Growth in Commercially Pure Titanium, Thesis
Submitted to the Faculty of Graduate and Postdoctoral Studies in Partial Fulfillment of the Requirements for the Degree of Doctor of Philosophy in Advanced Materials and Manufacturing
- [35] <http://www.alliedhightech.com/Equipment/metprep-3-grinder-polisher-with-powerhead>

- [36] George F. Vander Voort and William Van Geertruyden, Specimen preparation for Electron Back Scattered Diffraction
- [37] Struers. <http://www.struers.com/en/Knowledge/Grinding-and-polishing>
- [38] Randle, Valerie; Engler, Olaf (2000). *Introduction to texture analysis : macrotecture, microtexture and orientation mapping* (Digital printing 2003 ed.). Boca Raton: CRC Press
- [39] Susan Swapp, EBSD, https://serc.carleton.edu/research_education/geochemsheets/ebsd.html
- [40] Zhou, Weilie, Wang, Zhong Lin, Scanning Microscopy for Nanotechnology, 2007
- [41] Keith Dicks, Introduction to EBSD, <https://www.birmingham.ac.uk/Documents/college-eps/metallurgy/cem/IntroEBSD63slidesv2.pdf>
- [42] Novi Commentarii academiae scientiarum Petropolitanae 20, 1776, pp. 189–207
- [43] Gjoreski, Hristijan & Gams, Matjaz. (2011). Activity/Posture Recognition using Wearable Sensors Placed on Different Body Locations. . 10.2316/P.2011.716-067.
- [44] Momma, C.; Nolte, S.; Chichkov, B.N.; von Alvensleben, F.; Tunnermann, A. Precise laser ablation with ultrashort pulses. Appl. Surf. Sci. 1997, 109, 15–19.

- [45] K. M. Tanvir Ahmmed, Colin Grambow and Anne-Marie Kietzig, Fabrication of Micro/Nano Structures on Metals by Femtosecond Laser Micromachining, *Micromachines* 2014, 5, 1219-1253
- [46] Kanavin, A.P.; Smetanin, I.V.; Isakov, V.A.; Afanasiev, Y.V.; Chichkov, B.N.; Wellegehausen, B.; Nolte, S.; Momma, C.; Tunnermann, A. Heat transport in metals irradiated by ultrashort laser pulses. *Phys. Rev. B* 1998, 57, 14698–14703.
- [47] Chichkov, B.N.; Momma, C.; Nolte, S.; vonAlvensleben, F.; Tunnermann, A. Femtosecond, picosecond and nanosecond laser ablation of solids. *Appl. Phys. A* 1996, 63, 109–115.
- [48] STEPHEN HYPESH and GEOFF SHANNON, Femtosecond laser processing of metal and plastics in the medical device industry. *Femtosecond laser processing of metal and plastics in the medical device industry* 09/12/2014
- [49] K. M. Tanvir Ahmmed, Colin Grambow and Anne-Marie Kietzig, Fabrication of Micro/Nano Structures on Metals by Femtosecond Laser Micromachining, *Micromachines* 2014, 5, 1219-1253
- [50] Czichos, Horst (2006). *Springer Handbook of Materials Measurement Methods*. Berlin: Springer. pp. 303–304.
- [51] P. W. Bridgman, *Studies in Large Plastic Flow and Fracture*, McGraw-Hill, New York, (1952).
- [52] Dr Nick McCormick and Dr Jerry Lord, *Digital image correlation*, National Physical Laboratory, 2010

[53] “B. Beausir, J.-J. Fundenberger, Université de Lorraine - Metz, 2015, ATOM - Analysis Tools for Orientation Maps, <http://atom-software.eu/>,”

[54] Single crystal deformation. https://www.ifw-dresden.de/userfiles/groups/imw_folder/lectures/Metal_Physics_II___Plasticity/c2-all.pdf